

# Applications of Atomic Layer Deposition of Tin Oxide

Sunny Aggarwal

Department of Chemical Engineering, City College of New York (CUNY)

*NNIN REU Site: Penn State Nanofabrication Laboratory, The Pennsylvania State University, University Park, PA*

*NNIN REU Principal Investigator: Dr. Suzanne Mohney, Materials Science and Engineering, The Pennsylvania State University*

*NNIN REU Mentors: Haila Mohammed Aldosari and Shih-Ying Yu, MSE, The Pennsylvania State University*

*Contact: sunnys94@yahoo.com, mohney@ems.psu.edu*

## Abstract:

Atomic layer deposition (ALD) produces high-quality, low-porosity conformal nanostructures. Tin dioxide,  $\text{SnO}_2$ , is deposited within the void space of a face-centered cubic (FCC) silica opal lattice.  $\text{SnO}_2$  is a viable metal oxide for the formation of inverse opals due to its stability when the silica spheres are etched away. Furthermore, we explore its use as an effective interfacial layer for ohmic contacts between a metal and semiconductor.  $\text{SnO}_2$  is deposited by ALD using tetrakis (dimethyl amino) tin and water, then 30 nm sized opals are infiltrated with varying pulse lengths of these precursors in order to attain the most depth and complete infiltration. The resulting infiltrated  $\text{SnO}_2$  opals are characterized through field emission scanning electron microscopy (FE-SEM) and the 4-point probe to explore its filling efficiency and resistivity differences. In this work, we fill opals that are smaller than those that have been previously studied.

## Introduction:

Atomic layer deposition (ALD) is a modified chemical vapor deposition technique that provides conformal, uniform monolayer-by-monolayer growth. Such advantages allow for ALD to provide opportunities in optoelectronics [1] and microelectronics. An ALD cycle follows this process: dose with first precursor, tetrakis (dimethyl amino) tin (TDMASn); purge with  $\text{N}_2$  gas to remove any excess reactants; dose with second precursor, water ( $\text{H}_2\text{O}$ ); and finally purge the remaining reactants. In this study, ALD is used for infiltration of nano-opals and electrical contacts. Opals, 30 nm in size (smaller than those typically used for self-assembled photonic crystals) [2], were fabricated using the vertical deposition method. Self-assembly of these colloids created a face-centered cubic (FCC) lattice. Its 26% void space is infiltrated with tin oxide,  $\text{SnO}_2$ , through ALD as shown by the half reactions discussed previously by Mullings, et al. [3].

$\text{SnO}_2$  is selected due to ability to make good electrical contacts. It is a wide band gap semiconductor that can have a high carrier concentration and that shows strong resistance towards a variety of etching agents, including HF, which is the sole reagent that the silica templates are etched away with. Also, aggressive scaling of devices calls for low contact resistance. The use of  $\text{SnO}_2$  in contacts between a metal and a semiconductor are being explored. Such materials lower the effective Schottky barrier height, by relieving Fermi level pinning and lowering of the conduction band offset (CBO) [4].

## Experimental Procedure:

**Fabrication of Opals.** Nano silica colloids are dispersed in an open vial solution. Inside it, silicon substrates are placed in at a diagonal of  $45^\circ$ . The solution is then evaporated in a drying oven for four days, slowly, allowing for the opals to self-assemble in the FCC lattice.

**Preparation of Samples.** One of the opal substrates was cleaved and degreased. Degreasing included the standard 3-step procedure: sonication in acetone for five minutes, followed by sonication in isopropanol for five minutes, and a final sonication in deionized water for five minutes. The sample was then blown dry with  $\text{N}_2$  gas for 1-2 seconds and placed in a sterile sample holder.

**ALD Recipes.** The prepared samples were placed in an ALD reactor (Cambridge Savannah) set at these control conditions:

- Temperature of  $150^\circ\text{C}$ .
- $\text{N}_2$  purge flow rate of 20 sccm.

Conformal deposition of  $\text{SnO}_2$  thin films utilized saturated pulse times of 0.030 s for TDMASn and 0.015 s for  $\text{H}_2\text{O}$ . The purge times were 30 s.

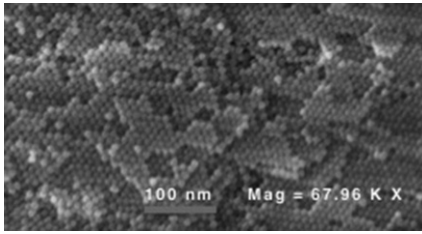


Figure 1: Empty opals; no dose of SnO<sub>2</sub>.

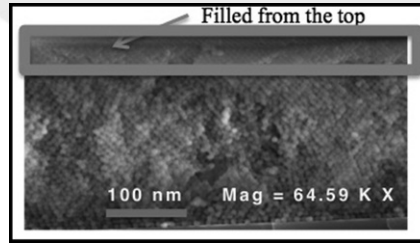


Figure 2: Infiltrated SnO<sub>2</sub> opal at a dose of 0.03 s of TDMASn and 0.015 s of H<sub>2</sub>O.

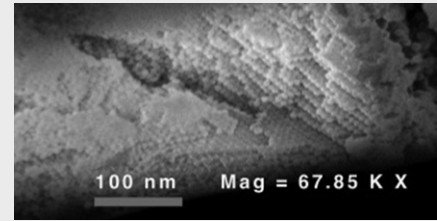


Figure 3: Infiltrated SnO<sub>2</sub> opal at a dose of 0.090 s of TDMASn and 0.045 s of H<sub>2</sub>O.

## Results and Conclusions:

Ellipsometry revealed that the growth rate of these films was ~0.5 Å/cycle. Since 5-6 nm of holes are to be filled from these 30 nm sized opals, 125 ALD cycles was used.

Figure 1 shows a FESEM image of the empty silica opal lattice, while Figure 2 demonstrates a partial filling of the opal from the saturated pulse times of the precursors. Hence, tripling the pulse times of each precursor respectively yields an almost complete infiltration as shown in Figure 3.

Further characterization of the opals done by the Keithley 2400 source-measure unit yields a variety of film sheet resistances, as shown in Figure 4.

Portrayed through the FESEM and data from the resistivity measurements, SnO<sub>2</sub> is shown to have deeper and a more complete infiltration into the opals as the dose increases. Such nano-scaled inverse opals can have applications in lithium ion batteries and gas sensors.

## Future Works:

The silica template must be etched using ion milling (primarily to expose) and then a dilute aqueous HF solution to attain the SnO<sub>2</sub> inverse opals. Further characterization of these samples, such as by transmission electron microscopy, and measurement of their electronic properties can be further performed, and their applicability for batteries and sensors can be explored.

## Acknowledgements:

The author thanks the support of Dr. Suzanne Mohny's lab group along with the nanofabrication staff in the Materials Research Institute of Pennsylvania State University and National Science Foundation for funding the National Nanotechnology Infrastructure Network Research Experience for Undergraduates (NNIN REU) Program.

Empty opals	
Average Voltage Measured (mV)	0.33
Current Used (nA)	5.0
Calculated Sheet Resistance (Ω)	66,000
SnO <sub>2</sub> Opals with 60 cycles at a dose of 0.030 s of TDMASn and 0.015 s of H <sub>2</sub> O	
Average Voltage Measured (mV)	0.11
Current Used (nA)	5.0
Calculated Sheet Resistance (Ω)	96,100
SnO <sub>2</sub> on regular Si wafer at 150°C	
Average Voltage Measured (mV)	0.18
Current Used (nA)	1.0
Calculated Sheet Resistance (Ω)	829,000

Figure 4: Resistance Measurements.

## References:

- [1] Niinistö, L., Nieminen, M., Päiväsaari, J., Niinistö, J., Putkonen, M. and Nieminen, M. "Advanced electronic and optoelectronic materials by Atomic Layer Deposition: An overview with special emphasis on recent progress in processing of high-k dielectrics and other oxide materials." *physics status solidi (a)* 201.7 (2004): 1443-1452.
- [2] Nishijima, Y., Ueno, K., Juodkazis, S., Mizeikis, V., Misawa, H., Tanimura, T., and Maeda, K. "Inverse silica opal photonic crystals for optical sensing applications." *Optics Express* 15.20 (2007): 12979-12988.
- [3] Mullings, Marja N. and Hägglund, Carl and Bent, Stacey F. Tin oxide atomic layer deposition from tetrakis (dimethyl amino) tin and water. *Journal of Vacuum Science & Technology A*, 31, 061503 (2013).
- [4] Yuan, Z., Nainani, A., Sun, Y., Lin, J. Y. J., Pianetta, P., and Saraswat, K. C. "Schottky barrier height reduction for metal/n-GaSb contact by inserting TiO<sub>2</sub> interfacial layer with low tunneling resistance." *Applied Physics Letters* 98.17 (2011): 172106.

M  
A  
T  
S

# Bimetallic Nanocrystals and Their Optical Properties

Nnenna E. Dieke  
Chemistry, Agnes Scott College

NNIN REU Site: Institute for Electronics & Nanotechnology, Georgia Institute of Technology, Atlanta, GA

NNIN REU Principal Investigator: Dr. Dong Qin, School of Materials Science and Engineering, Georgia Institute of Technology

NNIN REU Mentor: Yin Yang, School of Materials Science and Engineering, Georgia Institute of Technology

Contact: ndieke@agnesscott.edu, dong.qin@mse.gatech.edu, yin.yang@mse.gatech.edu

## Abstract and Introduction:

Silver nanocubes exhibit an excellent property known as localized surface plasmon resonance (LSPR) which depends heavily on the composition, size, and geometry of the nanoparticles. LSPR is useful in applications such as surface enhanced Raman scattering (SERS), making silver nanocubes an ideal material for SERS. Although silver nanocubes favor SER, it shows limited catalytic activity towards chemical reactions.

The objective of this project is to improve the catalytic behavior of silver (Ag) nanocubes, but still retain its SERS properties. This can be done by depositing a known catalyst, in this case palladium (Pd), onto the cube in order to create a Ag-Pd bimetallic nanostructure through a widely known process called galvanic replacement reaction. Galvanic replacement reaction destroys the SERS property because one Pd atom deposits onto the cube at the expense of two Ag atoms [1]. In order to combat this, galvanic is done in the presence of reducing agents that will reduce Ag<sup>+</sup> back to Ag atoms to be co-deposited alongside with the palladium which will help in retaining the SERS property.

Through etching the Ag-Pd bimetallic structures with hydrogen peroxide (H<sub>2</sub>O<sub>2</sub>), Ag-Pd hollow nanoboxes can be created. These hollow nanostructures are more stable than Ag nanocubes, making them more ideal for SERS. The enlarged surface area should also be beneficial to their catalytic activities.

## Experimental Procedure:

The way in which the Ag-Pd bimetallic nanostructure was generated was through galvanic replacement reaction alongside reducing agents, NaOH and ascorbic acid (AA). The palladium precursor, disodium tetrachloropalladate (Na<sub>2</sub>PdCl<sub>4</sub>), was titrated at a rate of 0.02 mL/min into a 20 mL vial that contained 1 mM of 29K polyvinyl pyrrolidone (PVP), which acted as a capping agent, NaOH, ascorbic acid, and silver nanocubes, Figure 1. The amount of NaOH introduced into the solution assisted in tuning the pH of the solution.

Once different volumes of the palladium precursor has been titrated into the mixture a ultraviolet-visible (UV-Vis) spectrum was collected to monitor the change in morphology over time, then the samples were washed three times before being prepared for TEM imaging.

## Results and Discussion:

Experiments were conducted under basic and acidic conditions as well as a control experiment in which no NaOH was added to the solution. In the control experiment, the UV-Vis showed a significant shift indicating that the morphology of the cubes were changing and galvanic was taking place, Figure 1A. After taking TEM images, Figure 2, holes in the cubes were observed which also confirmed that galvanic replacement reaction did in fact take place, and a layer of palladium is present.

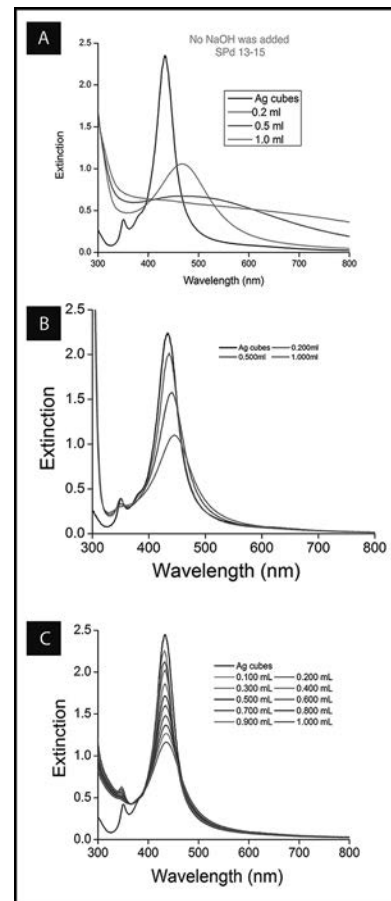


Figure 1: UV-Vis spectra of (A) the control experiment in which no NaOH was added, (B) experiment done under acidic conditions in which 200  $\mu$ L of 200 mM NaOH and 0.5 mL of 100 mM ascorbic acid were used, and (C) experiment done under basic conditions in which 90  $\mu$ L of 200 mM NaOH and 0.5 mL of 100 mM ascorbic acid were used. (See full color version on page xxxvi.)

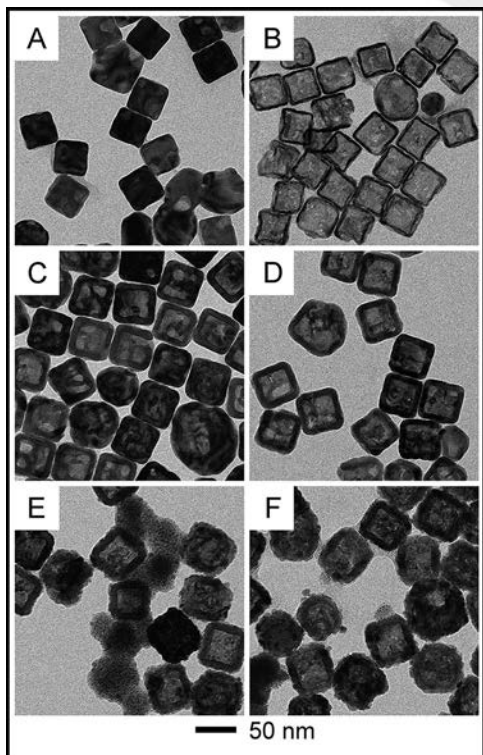


Figure 2: TEM image of control experiment where no reducing agent was added. A, C, and E are images before etching; and B, D, and F are images taken after etching with an excess amount of  $H_2O_2$  solution.

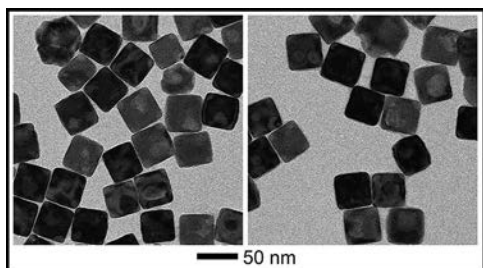


Figure 3: TEM image of sample when 200  $\mu L$  of NaOH and 0.5 mL of 100 mM AA are used.

The experiment was also ran under acidic conditions with a pH of 4.83. In these samples 200  $\mu L$  of 200 mM NaOH and 0.5 mL of 100 mM AA were used to tune the pH. The UV-Vis showed a shift that is characteristic of galvanic, but the shift was not as severe as in the control experiment in which no NaOH was present (see Figure 1B). The TEM images, Figure 3, showed slight holes in the cube, but in comparison with the control these holes were not as intense.

Lastly, under basic conditions with a pH of 10.86, it was noted that the UV-Vis did not have much of a shift indicating the inhibition of galvanic, Figure 1C. After taking TEM images, Figure 4, it was confirmed that the cube somewhat retained their shape, but after etching the sample with a 3% solution of  $H_2O_2$  in order to test the quality of the cubes it was shown that the cubes were unstable, and little to no cubes were left afterwards.

The occurrence of self-nucleation was observed in Figure 1, image E. This was due to the high amount of  $Na_2PdCl_4$  that was being injecting into the solution. Some of the precursor began to form clusters instead of depositing onto the cube which is something that negatively impacted the experiment.

### Future Work:

These preliminary results can assist in furthering the study of the creation of Ag/Pd bimetallic nanostructure that possesses both excellent SERS and catalytic properties. In the future, the conditions could continue to be manipulated to determine if it is indeed possible to create these stable structures that can last under  $H_2O_2$  etching.

### Acknowledgements:

I would like to thank Dr. Dong Qin and my mentor Yin Yang for the opportunity of working in the Qin Lab this summer, Georgia Tech NNIN REU site coordinator Leslie O'Neill, as well as Joyce Allen and Dr. Nancy Healy. I would also like to thank the NSF and NNIN REU Program for their support.

### References:

- [1] "Galvanic replacement-free deposition of Au on Ag for core-shell nanocubes with enhanced chemical stability and SERS activity," Y. Yang, J. Liu, Z. Fu, and D. Qin; JACS, 136, 8153-8156, (2014).

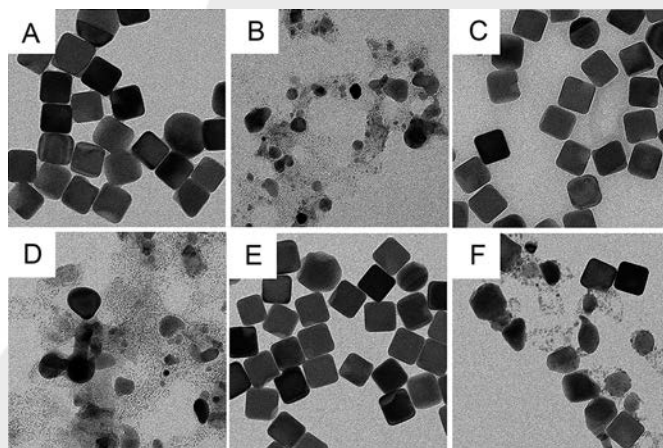


Figure 4: TEM image of product when 90  $\mu L$  of NaOH and 0.5 mL of 10 mM AA is used. A, C, and E are images before etching; and B, D, and F are images taken after etching with an excess amount of  $H_2O_2$  solution.

# Selective Area Atomic Layer Deposition: Developing Techniques that will Enable Single-nm Technologies

Alicia M. Elliott

Engineering Science, Stony Brook University

NNIN REU Site: Cornell NanoScale Science & Technology Facility, Cornell University, Ithaca, NY

NNIN REU Principal Investigator: Prof. James R. Engstrom, School of Chemical and Biomolecular Engineering, Cornell University

NNIN REU Mentor: Wenyu Zhang, School of Chemical and Biomolecular Engineering, Cornell University

Contact: alicia.elliott@stonybrook.edu, jre7@cornell.edu, wz89@cornell.edu

## Abstract:

Atomic layer deposition (ALD) is a chemical vapor deposition process with self-limiting growth, providing atomic level, or “digital,” control of thickness. Selective deposition extends this control to three dimensions, so 3D structures can be created without lithography. To deposit selectively, growth is promoted on one surface and prevented on another by varying deposition conditions. This project probes the intrinsic reactivity of two precursors: tetrakis-(ethylmethylamino)hafnium (TEMAH;  $\text{Hf}(\text{N}(\text{CH}_3)(\text{C}_2\text{H}_5)_2)_4$ ) and tris(dimethylamino)silane (3DMAS;  $\text{SiH}(\text{N}(\text{CH}_3)_2)_3$ ). Nucleation of each precursor on a metal and dielectric substrate was studied. Saturation curves of film deposited vs. dose time were generated for TEMAH by exposing the substrates to the first half of an ALD cycle. For 3DMAS, thicker films were deposited and the growth rate was estimated using *ex situ* ellipsometry. *Ex situ* x-ray photoelectron spectroscopy (XPS) was used to determine amount of precursor deposited.

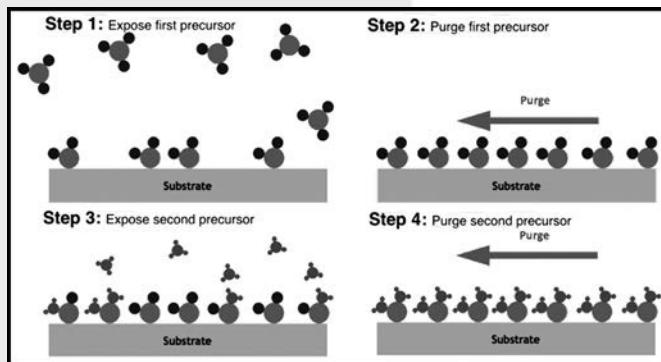


Figure 1: Schematic of the four-step ALD cycle.

## Introduction:

Atomic layer deposition (ALD) is a deposition technique with a four step, self-limiting growth process (see Figure 1). Self-limiting growth allows digital control of thickness, creating highly conformal films on high aspect ratio structures.

Semiconductor devices have gone towards three dimensional (3D) features to increase speed and decrease power consumption (e.g., Intel's tri-gate transistor). Selective deposition could be utilized to pattern in 3D using ALD. To achieve this, growth is promoted on one substrate (e.g., a dielectric) and prevented on another (e.g., a metal). If selectivity can be achieved using ALD, this precise control can be extended to three dimensions, creating 3D patterns without lithography.

As a first step to developing a process that is selective, we must first understand the intrinsic reactivity of the thin film precursor with substrates of interest.

The nucleation of each precursor on two substrates, a dielectric ( $\text{SiO}_2$  or  $\text{Al}_2\text{O}_3$ ) and a metal (Cu), must be studied to determine how to selectively prevent deposition. Precursor dose times and heater temperature should be considered. Dose times can be varied to determine when each substrate becomes saturated with the precursor.

## Experimental Procedure:

Two precursors were studied: tetrakis-(ethylmethylamino) hafnium (TEMAH), the precursor for hafnia ( $\text{HfO}_2$ ) films, and tris(dimethylamino)silane (3DMAS), the precursor for silica ( $\text{SiO}_2$ ) films.

TEMAH was deposited onto copper (Cu) and chemical oxide (chemically grown  $\text{SiO}_2$ ) substrates. Chemical oxide ( $\text{SiO}_2$ ) was grown by twice exposing silicon substrates to two minutes of buffered oxide etch 6:1 and 15 minutes of Nano-Strip<sup>®</sup> heated to 70-80°C. Each sample was exposed to one half-cycle of thermal  $\text{HfO}_2$  ALD at a heater temperature ( $T_s$ ) of ~ 250°C, with the following precursor dose times: 0.0, 0.1, 0.2, 0.4, 0.7, 1.0, 2.0, 3.5, 5.0, and 7.0 seconds. Plasma  $\text{SiO}_2$  ALD films were deposited at 200°C onto Cu and ALD-deposited alumina ( $\text{Al}_2\text{O}_3$ ) substrates, varying the number of cycles as follows: 0, 10, 20, 50, and 100 cycles. The 3DMAS doses were also varied, with dose times of 0.0, 0.1, 1.0, and 4.0 seconds.

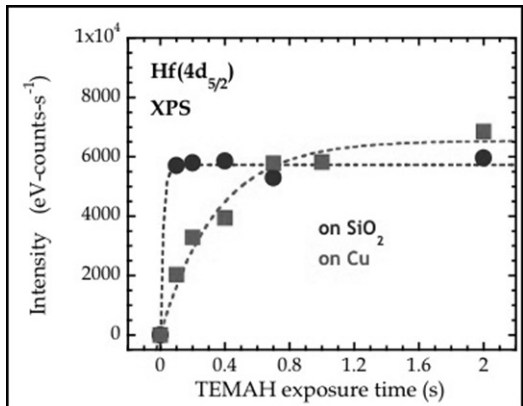


Figure 2: Integrated intensity of the Hf(4d<sub>5/2</sub>) peak as a function of TEMAH dose time on SiO<sub>2</sub> and Cu.

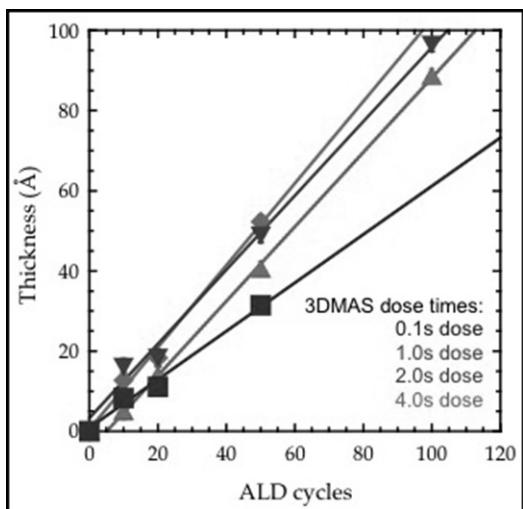


Figure 3: Estimated thicknesses of SiO<sub>2</sub> films (from SE) as a function of ALD cycles for four 3DMAS dose times.

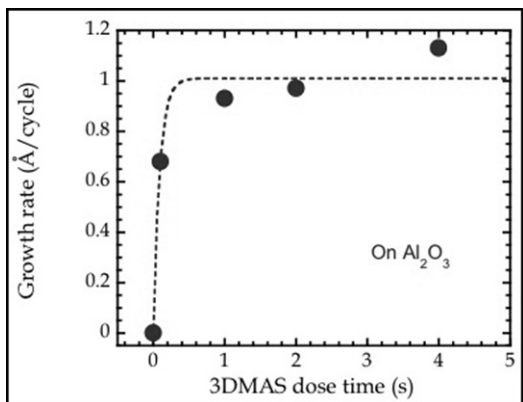


Figure 4: Estimated growth rate of SiO<sub>2</sub> ALD on Al<sub>2</sub>O<sub>3</sub> (from SE) as a function of 3DMAS dose time.

*Ex situ* XPS and spectroscopic ellipsometry (SE) were used to determine how much precursor was deposited. SE was used to estimate film thicknesses for the SiO<sub>2</sub> ALD on Al<sub>2</sub>O<sub>3</sub> and estimate growth rates. Saturation curves were generated from these analyses.

### Results and Conclusions:

In Figure 2, we present the XPS integrated intensity for Hf(4d<sub>5/2</sub>) against TEMAH dose time, generating a saturation curve for each substrate. These results showed that TEMAH saturated on SiO<sub>2</sub> substrates (~0.1s - 0.2s TEMAH dose time) much more quickly than on Cu substrates (~2s). This is most likely due to the higher concentration of hydroxyl (-OH) groups on SiO<sub>2</sub> surfaces, thus promoting better adsorption of the precursor on the SiO<sub>2</sub>.

SiO<sub>2</sub> ALD is a plasma process (using 3DMAS and oxygen plasma), so doing half-cycle ALD like we did for Hf will not capture the important processes occurring in the oxygen plasma half-cycle. A series of thicker films were deposited for each 3DMAS dose time.

In Figure 3, we present the estimated SiO<sub>2</sub> thicknesses on Al<sub>2</sub>O<sub>3</sub>. Growth rates can be estimated using the slopes of the data points. The growth rate for 0.1s dose time is ~0.68 Å/cycle, while 1.0s, 2.0s, and 4.0s dose time growth rates ranged from ~0.93 to 1.13 Å/cycle (saturation).

A saturation curve was generated for alumina substrates from this data, as seen in Figure 4. This shows a similar shape to that for TEMAH on SiO<sub>2</sub>. Because of the rougher substrate surface for Cu, SE cannot be used to estimate film thickness. XPS analysis will be performed and a saturation curve will be generated.

### Acknowledgements:

I would like to thank the National Science Foundation for funding this work, and the NNIN REU Program and the CNF for organization. I would also like to thank Professor James R. Engstrom and Wenyu Zhang for their guidance, teaching, and reassurance. I also thank Melanie-Claire Mallison, Rob Ilic, Vince Genova, and Meredith Metzler. Finally, thanks to all of the CNF staff.

# Directed Assembly of Nanowires in AC Fields: Tuning Wire Design and Electrode Geometry to Observe Ordered Arrays

Robyn Emery  
Biology, Northwest University

**NNIN REU Site:** Penn State Nanofabrication Laboratory, The Pennsylvania State University, University Park, PA  
**NNIN REU Principal Investigator:** Prof. Christine D. Keating, Department of Chemistry, The Pennsylvania State University  
**NNIN REU Mentor:** Sarah J. Boehm, Department of Chemistry, The Pennsylvania State University  
**Contact:** robyn.emery13@northwestu.edu, keating@chem.psu.edu, sjb340@psu.edu

## Introduction:

Nanowires form a fascinating topic of inquiry in modern research and offer material properties that are advantageous in fields such as next-generation electronics, solar cells, and optics [1]. Dense, ordered arrays of nanowires are needed to investigate potential advantages. In unregulated assembly, however, nanowires tend to become trapped in entropically unfavorable positions and orientations. This project explored the introduction of an applied current (AC) field on gold (Au) nanowires to form assemblies with observable and ultimately reproducible properties. Partially-etched nanowires were synthesized and assembled in lithographically-designed gold electrodes. Field strength was fine-tuned for specific wire designs, and the use of different electrode geometries created unique field conditions that visibly influenced resulting assemblies. Effectiveness of electrode geometries was also studied in experiments.

## Wire Synthesis:

It was necessary to fabricate nanowires in large quantities while maintaining a relatively narrow size distribution. This was achieved using a porous alumina membrane that acted as a nanotemplate for the metallic wires. Multicomponent nanowires featuring segments of different metals were able to be prepared via electrodeposition into pores beginning bottom-upwards from a sacrificial silver base. Removal of both the membrane and base yielded approximately a billion monodisperse wires in solution, with a nominal diameter of 300 nm and length determined by deposition time.

The wire design chosen for experiments featured a 2  $\mu\text{m}$  gold (Au) segment and a 3  $\mu\text{m}$  etched segment (2Au-3E) (Figure 1). To achieve partially-etched nanowires, silver (Ag) metal was deposited on top of the gold segment.

A thin coating of amorphous silica retained wire shape, and selective etching of the silver segment left a hollow, solvent-filled segment in its place. Assemblies resulting from these wires were more ordered than wires featuring a longer Au segment, so experiments with the 2Au-3E wires were chosen for accurate analysis of lattice structures.

## Electrode Synthesis:

Electrodes were designed featuring a central gap, micrometers in diameter, to accommodate the small wire size. Au electrodes were fabricated using standard photolithography techniques. After spinning positive photoresist onto 35 mm circular glass cover slip, projected light through a patterned mask exposed certain regions in the precise shape of electrodes. After removal of the reacted areas in a developing solution, a binding titanium (Ti) layer and a 50 nm Au layer were deposited via electron-beam evaporation. Lift-off in another developing solution removed all remaining photoresist to leave usable Au electrodes behind on the substrate surface. The two extended probes at the electrode base provided an attachment site for an external field generator.

Two types of electrodes were fabricated for assemblies (Figure 2). Bulb-stem electrodes featured alternating circular and

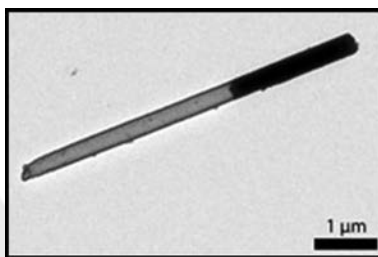


Figure 1: TEM of one of the 2Au-3E nanowires used in experiments.



Figure 2: The two electrode designs: bulb-stem (left) and interdigitated (right).

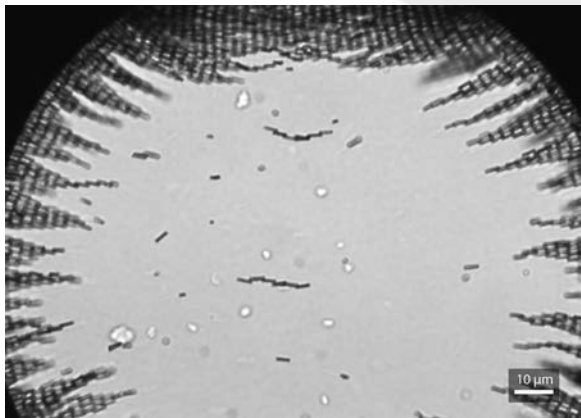


Figure 3: A 100  $\mu\text{m}$  bulb region of the bulb-stem electrode during assembly.

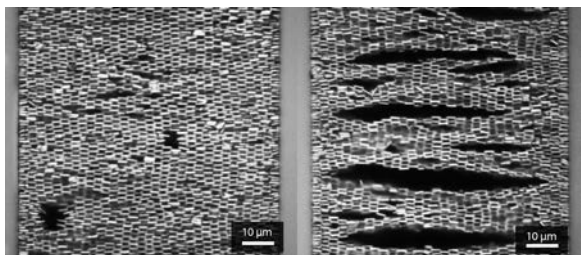


Figure 4: Annealed assemblies in the 50  $\mu\text{m}$  gap of bulb-stem electrodes (left) and interdigitated electrodes (right).

rectangular regions, 100  $\mu\text{m}$  at the widest and 50  $\mu\text{m}$  at the narrowest. Interdigitated electrodes featured gaps of uniform widths ranging from 10  $\mu\text{m}$  to 150  $\mu\text{m}$ . Both electrode geometries produced unique areas of field maxima and minima that influenced final lattice structure.

### Experimentation and Results:

Nanowires were appropriately diluted and placed in a silicone spacer on top of the electrode. Electrodes were attached to an external field generator using a thin Au wire and Ag epoxy binding on each probe. The cover slip with the set-up apparatus was then placed on an inverted optical microscope for real-time observation during experiments. Once wires were sedimented to the substrate surface, the field was turned on at low conditions and increased over time (Figure 3).

At low voltage and frequency, wires began to orient preferentially with Au segments in contact with the electrode edge. Particle motion occurred through a process called dielectrophoresis, where field-induced dipoles on polarizable gold segments drew wires towards the stronger field gradient at edges. Increasing voltage and frequency of the field drew in a greater number of wires and eventually allowed wires to completely bridge the electrode gap.

After the field was on for a significant amount of time, assembly structures were “annealed”—we refer to annealing as turning on and off the field to give wires the opportunity to reorient positions. The annealed structures in the 50  $\mu\text{m}$  gaps of both the interdigitated and bulb-stem electrodes were compared (Figure 4). The lattices in the bulb-stem electrodes had significantly less defects, perhaps a result of “funneling” concentrating effect towards stem centers produced by larger bulbs. Since interdigitated electrodes had parallel edges, lattices did not exhibit the same density and uniformity.

A qualitative comparison of the two suggests that electrodes of alternating bulb-stem patterns are more capable of producing ideal nanowire arrangements than isometric gaps. In addition, we observed that spacing between wires was too small to accommodate the longer etched segment, suggesting that some wires had to be positioned out of plane for uniform lattices to form.

### Summary:

Overall, ordered arrays of partially-etched gold nanowires were successfully produced using the 2Au-3E wire design. The bulb-stem electrodes proved to be the most effective at condensing assemblies by comparing final annealed structures to the IDE geometry.

### Acknowledgements:

I’d like to thank my mentor, Sarah Boehm, for all her patience and help. I’d also like to thank my principal investigator, Christine Keating, and the entire Keating group at Penn State for allowing me to use their resources. Another *thank you* to the NNIN REU Program and NSF for the funding provided.

### References:

- [1] Triplett, D. A., et al.; “Assembly of Gold Nanowires by Sedimentation from Suspension: Experiments and Simulation”; *J. of Phys. Chem. C.*, 114, 7346 (2010).

# Early Hydration of Portland Limestone Cements Monitored by Raman Spectroscopy

Dylan J. Freas  
Chemistry, Williams College

**NNIN REU Site:** Institute for Electronics & Nanotechnology, Georgia Institute of Technology, Atlanta, GA  
**NNIN REU Principal Investigator:** Dr. Kimberly E. Kurtis, Civil and Environmental Engineering, Georgia Institute of Technology  
**NNIN REU Mentor:** Elizabeth I. Nadelman, Civil and Environmental Engineering, Georgia Institute of Technology  
**Contact:** dylan.j.freas@williams.edu, kimberly.kurtis@ce.gatech.edu, enadelman3@gatech.edu

## Abstract:

Given its innate heterogeneity, cement hydration is a difficult process to study, and many current techniques have limited use in identifying specific chemical changes that occur during the hydration process. Raman spectroscopy has the potential to supply this information. This study was aimed at evaluating the capability of Raman spectroscopy in studying the hydration of Portland limestone cements. The consumption of many raw cement phases and the formation of major cement hydration products were detected over various time periods of hydration. This information provides insight on the nanostructural development of concrete, which can be correlated to the evolution of its macroscopic properties.

## Introduction:

Globally, the cement industry accounts for approximately five percent of current anthropogenic carbon dioxide (CO<sub>2</sub>) emissions [1]. The source of most of the CO<sub>2</sub> emissions during cement manufacturing is the heating of raw materials, such as limestone and clay, to form cement clinker. One method the cement industry has implemented to reduce CO<sub>2</sub> emissions is replacing a portion of cement clinker with filler material such as limestone. However, it is crucial to understand the effect of limestone addition on the hydration and microstructural development of cement.

Raman spectroscopy is a relatively innovative technique in the field of pure cement study. One of the most significant features of this technique is its capability for a real-time *in situ* analysis. Using this technique, researchers have characterized individual clinker components, studied the progress of timed hydration on various clinker phases, and identified products of Portland cement hydration [2]. The purpose of this present study is to extend Raman spectroscopy to the characterization of Portland limestone cements and to demonstrate its ability to characterize the formation of hydration products at the nanoscale.

## Experimental Procedure:

Type I/II ordinary Portland cements containing ~3% limestone ("AI") were compared to Type IL Portland limestone cements containing ~12% limestone ("AL"). The cements were mixed with deionized water at a water-to-cement ratio of 0:4. The

cement pastes were stored in microscope well slides, and cover slips were sealed over the pastes in order to reduce the effect of carbonation.

Raman spectra were collected using a Thermo Almega XR Micro and Macro Raman Analysis Spectrometer with a 488 nm laser. A circular spot size of 50 μm was used at 50x magnification. The Raman shift range chosen for study was 200-1200 cm<sup>-1</sup> with 40 seconds exposure. All instrumental configuration was systematically chosen by targeting for a high S/N ratio and statistical representativeness.

The collected data were processed using Thermo Scientific's OMNIC Series software. The qualitative analysis of cement hydration was performed on the data normalized to the signal with the largest Raman intensity value. Baseline correction and cover slip subtraction were also applied in the data analysis.

## Results And Discussion:

The Raman spectra for the two cement pastes are shown in Figures 1 and 2. Peaks were identified using values reported in the literature [3]. The results show that many major phases of commercial cement, such as limestone, gypsum, and tricalcium silicate and dicalcium silicate (C<sub>3</sub>S / C<sub>2</sub>S), can be detected, along with many major cement hydration products, including ettringite, calcium hydroxide (CH), and calcium silicate hydrate (C-S-H).

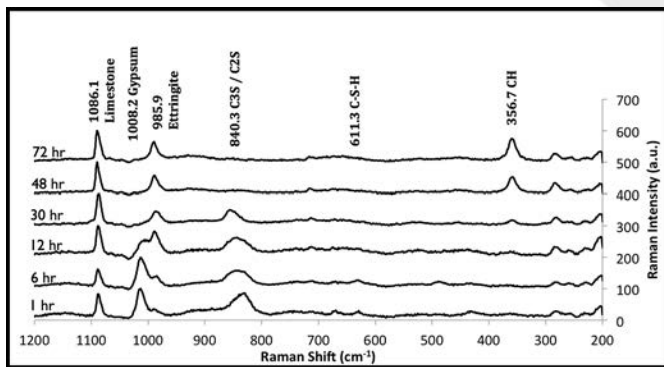


Figure 1: Time-lapsed Raman spectra of a Type IL Portland limestone cement (AL).

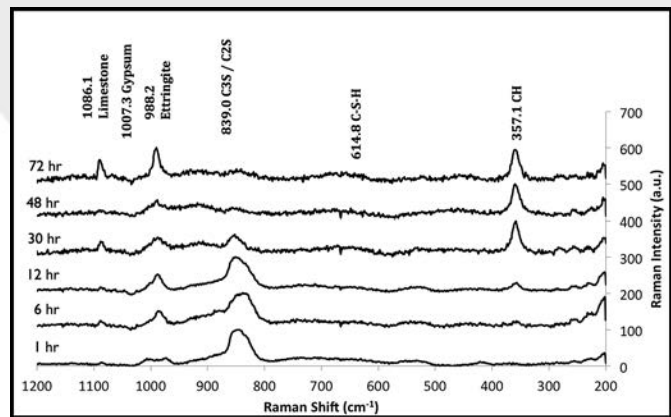


Figure 2: Time-lapsed Raman spectra of a Type I/II ordinary Portland cement (AI).

For both cement pastes, the  $C_3S/C_2S$  bands from  $\sim 800$ - $900\text{ cm}^{-1}$  become shifted toward  $860\text{ cm}^{-1}$  by 30 hr, which corresponds to the initial rapid hydration of  $C_3S$ , leaving primarily  $C_2S$ . By 48 hr, the  $C_2S$  signal has disappeared, indicating the consumption of both calcium silicate phases. The formation of CH ( $\sim 356\text{ cm}^{-1}$ ) is detected by 24 hr and its principal band increases in intensity through 72 hr. C-S-H was not clearly detected, but the broad C-S-H band between  $600$ - $700\text{ cm}^{-1}$  is seen to increase in intensity over time as more C-S-H is produced.

The conversion from gypsum ( $\sim 1008\text{ cm}^{-1}$ ) to ettringite ( $\sim 988\text{ cm}^{-1}$ ) is illustrated as early as 6 hr and continues through 24 hr, at which point the gypsum signal has disappeared and the ettringite band continues to increase in intensity. This trend continues through 72 hr. The gypsum band is not as pronounced in the Type I/II ordinary Portland cement paste as it is for the Type IL Portland limestone cement paste because the corresponding raw cement contained less gypsum prior to hydration.

### Conclusions and Future Work:

This research shows that Raman spectroscopy can effectively characterize the hydration of Portland limestone cements. This nondestructive technique has been shown to provide results that are consistent with those from previous studies of cement hydration, including calorimetry and Fourier transform infrared spectroscopy studies [4]. Future work will correlate Raman spectroscopic signatures with morphological information obtained by scanning electron microscopy and specific surface area analysis, chemical composition information obtained by thermogravimetric analysis, and reaction kinetics information

provided by isothermal calorimetry, to obtain a comprehensive understanding of the nanostructural development of cement-based materials.

### Acknowledgements:

This research was performed through the support of the National Nanotechnology Infrastructure Network Research Experience for Undergraduates (NNIN REU) Program and the National Science Foundation. Any opinions, findings, and conclusions or recommendations expressed in this material are those of the author(s) and do not necessarily reflect the views of the National Science Foundation. Much appreciation goes to Elizabeth Nadelman and Dr. Kimberly Kurtis for their guidance in this project.

### References:

- [1] Lollini, et al. Effects of Portland Cement Replacement with Limestone on the Properties of Hardened Concrete. *Cement & Concrete Composites*, 2014, 46, 32-40.
- [2] Garg, et al. A Raman Spectroscopic Study of the Evolution of Sulfates and Hydroxides in Cement-Fly Ash Pastes. *Cement and Concrete Research*, 2013, 53, 91-103.
- [3] Potgieter-Vermaak, et al. The Application of Raman Spectrometry to Investigate and Characterize Cement, Part I: A Review. *Cement of Concrete Research*, 2006, 36, 656-662.
- [4] Ylmen, et al. Early Hydration and Setting of Portland Cement Monitored by IR, SEM, and Vicat Techniques. *Cement and Concrete Research*, 2009, 39, 433-439.



# Extent of Dopant Activation after Microwave and Rapid Thermal Anneals Using Similar Heating Profiles

Taliya Gunawansa

Optical Engineering, Norfolk State University

*NNIN REU Site: ASU NanoFab, Arizona State University, Tempe, AZ*

*NNIN REU Principal Investigator: Dr. T. L. Alford, School for Engineering of Matter, Transport and Energy, Arizona State University*

*NNIN REU Mentors: Ms. Zhao Zhao, School of Engineering of Matter, Transport and Energy, Arizona State University;  
Dr. A. Lanz, Department of Mathematics, Norfolk State University*

*Contact: t.s.gunawansa@spartans.nsu.edu, ta@asu.edu, zzhao44@yahoo.com, alanz@nsu.edu*

## Abstract:

Many sustainability issues arise with the current manufacturing processes used for semiconductor-based solar cells. Microwave (MW) heating could be adopted as sustainable since its capital costs are less and it more efficient than conventional furnace systems. In addition, microwave heating is directly produced inside the material. This study compares the extent of dopant activation and damage repair for a MW anneal and a conventional rapid thermal anneal (RTA) with identical heating profiles. Sheet resistance measurements were used to assess the extent of dopant activation and ion channeling was used to monitor the extent of damage repair. The results showed that for identical heating profiles, MW annealing resulted in better dopant activation and damage repair.

## Introduction:

When high concentrations of dopants are implanted into silicon, the surface layer becomes damaged. Large amounts of lattice damage results in increased sheet resistance. High temperature anneals are performed to repair the damage created during ion implantation and to also electrically activate the implanted dopants [1]. Rapid thermal annealing (RTA) has been used to reduce the diffusion of dopants during annealing. However, uneven heating sometime occurs due to differences in the emissivities of the various near-surface device materials. Additionally, the photons used in the RTA lamp and laser heating were not able to penetrate beyond the surface regions of the silicon [2]. However, MW of silicon allows for volumetric heating of the wafer due to the greater penetration depth of the microwave radiation [3]. In this study, we investigate the extent of dopant activation and damage repair for a MW anneal and a conventional RTA with identical heating profiles.

## Experimental Procedure:

Silicon wafers received a 180 keV arsenic ion implant with one of three different doses: 1, 2 or  $4 \times 10^{15}$  ions  $\text{cm}^{-2}$ . A single-frequency (2.45 GHz)  $2.8 \times 10^4 \text{ cm}^3$  cavity applicator microwave system with a 1300 W magnetron source was used to MW anneal the arsenic implanted silicon. A pyrometer, mounted through the cavity wall, with a spectral response of about  $3.9 \mu\text{m}$ , was used to monitor the near surface temper-

ature. The heating curves were then plotted in order to determine ramp up temperatures, times, and rates. A Heat Pulse 610 RTA was used to anneal each sample to obtain a similar heating curve as that of the corresponding microwave annealed sample. To monitor dopant activation, the sample surfaces were contacted with an in-line four-point-probe (FPP) equipped with a 100 mA Keithley 2700 digital multimeter. In order to determine the carrier concentration after microwave processing, Hall effect analysis was also performed. Rutherford backscattering spectrometry (RBS) was used to measure the extent of recrystallization of after each anneal.

## Results and Conclusions:

Figure 1 shows the close match between the heating curves for both 50 sec MW and RTA anneals of the  $2 \times 10^{15} \text{ cm}^{-2}$  sample. These results are consistent for all samples in this study. In Figure 2, sheet resistance values are shown for all three doses as a function of microwave and RTA annealing times. The MW saturation point for the dopant activation is 50 seconds. Based on this result, two set times are used for the RTA: 50s and 100s. The sheet resistances for the 50s RTA anneals are out of range (for all three doses); hence, the single hollow plotted points for the 100s RTA samples. Table 1 displays the Hall measurement results, including the carrier concentration and the sheet resistance for each MW dose.

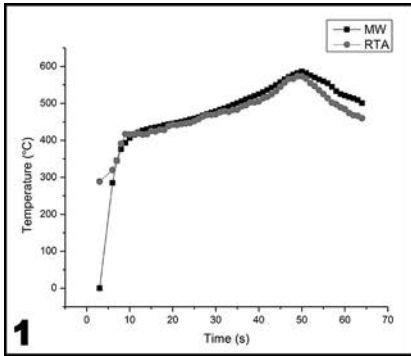


Figure 1: Illustration of the heating curve comparison between MW and RTA.

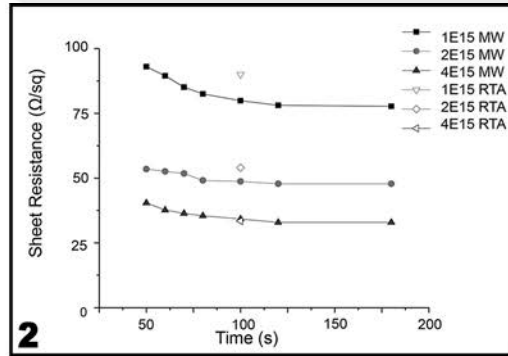


Figure 2: Comparison of the sheet resistance for MW and RTA samples.

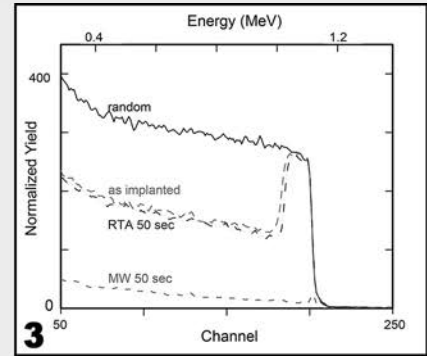


Figure 3: Represented the RBS data for four selections of samples.

Microwave annealing the samples allowed for a wider range of annealing times after the already determined saturation point. Based on the data in Table 1, it can be concluded that higher the dose and time of arsenic in the silicon, the smaller the difference in the sheet resistance between the RTA and microwave annealing. For the MW Hall measurements, the  $1 \times 10^{15}$  ions  $\text{cm}^{-2}$  100s sample has a higher carrier concentration than the  $2 \times 10^{15}$  ions  $\text{cm}^{-2}$  50s sample. For all three 50s doses for the RTA samples, the sheet resistance was observed to be inconclusive as a result of not reaching the saturation point.

Figure 3 illustrates the normalized yield and energy between a random, as implanted, RTA 50s, and MW 50s samples. These results showed that the MW anneals gave better dopant activation and damage repair for short times for identical heating profiles.

### Future Work:

Optimize and model the microwave induced dopant activation heating process, and present findings at TMS 2015 conference.

### Acknowledgments:

I sincerely thank my PI, Dr. T. L. Alford, and my mentors Ms. Zhao Zhao and Dr. A. Lanz for all of their assistance and guidance. I extend my thanks to Dr. Trevor Thornton, the National Nanotechnology Infrastructure Network Research Experience for Undergraduates Program, the National Science

Foundation, and the Center for Solid State Electronics Research at Arizona State University for providing the opportunity and funding for this research experience.

### References:

- [1] K.N. Tu, J.W. Mayer, L.C. Feldman, *Electronic Thin Film Science*, Macmillan Publishing Company, New York, NY, 1992.
- [2] J.D. Plummer, M.D. Deal, P.B. Griffin, *Silicon VLSI Technology: Fundamentals, Practice and Modeling*, Prentice Hall, Upper Saddle River, NJ, 2000.
- [3] T.L. Alford, M.J. Madre, R.N.P. Vemuri, N. David Theodore. 520 4315 (2012).

Dose ( $\text{cm}^{-2}$ )	Time (s)	Carrier Concentration ( $\#/\text{cm}^3$ )	Sheet Resistance ( $\Omega/\text{sq}$ )
1.00E+15	50	9.00E+19	92.6
1.00E+15	100	1.00E+20	80.3
2.00E+15	50	1.70E+20	53.5
2.00E+15	100	1.80E+20	48.7
4.00E+15	50	3.40E+20	40.4
4.00E+15	100	4.00E+20	34.2

Table 1: Depiction of the Hall measurements obtained from the MW samples.



# Characterizing TiN Resistivity using Plasma Enhanced Atomic Layer Deposition with TDMAT

Matthew Hartensveld

Microelectronic Engineering, Rochester Institute of Technology

NNIN REU Site: UCSB Nanofabrication Facility, University of California, Santa Barbara, CA

NNIN REU Principal Investigator: Mark Rodwell, Electrical and Computer Engineering, University of California Santa Barbara

NNIN REU Mentor: Robert Maurer, Electrical and Computer Engineering, University of California Santa Barbara

Contact: matthart610@yahoo.com, rodwell@ece.ucsb.edu, robdmaurer@gmail.com

## Abstract:

The effects of multiple deposition parameters on the plasma enhanced atomic layer deposition (PEALD) of conductive titanium nitride (TiN) films were investigated. Specifically, effects of plasma pressure and time on TiN resistivity were characterized. Optimum growth conditions for minimum film resistivity was determined to be: plasma power of 500W, precursor gas of ammonium ( $\text{NH}_3$ ), chamber pressure of 2 mTorr, and a plasma time of 30 seconds. The minimum achieved resistivity was found to be  $175 \mu\Omega\text{cm}$ .

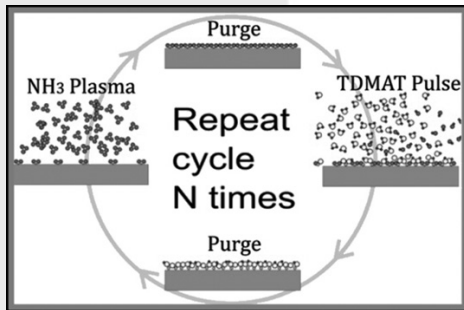


Figure 1: ALD process.

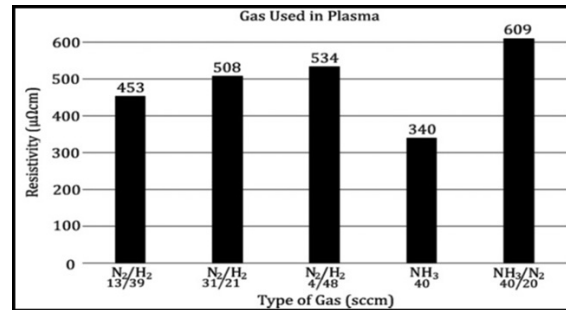


Figure 2: Plasma composition on resistivity.

## Introduction:

There is a constant need for faster devices and communications. As devices are pushed to faster speeds though, frequency becomes a limiting factor. Atomic layer deposition (ALD) conducting films are used in modern electronics due to their properties of low resistivity and ability to evenly coat high aspect ratios allowing for more advanced devices. Titanium nitride (TiN) is often chosen due to its ideal properties of low resistivity. TiN is deposited by flowing tetrakis (dimethylamido) titanium (TDMAT) into the ALD chamber followed by, an argon (Ar) purge, a  $\text{N}_2/\text{H}_2$  plasma treatment, and another Ar purge. This cycle is shown in Figure 1 and is repeated until the desired thickness is reached. This study provides an investigation of the effects of  $\text{NH}_3$  plasma pressure on film resistivity as well as a review of these other reported variables regarding TiN.

## Experimental Procedure:

The ALD system used was an Oxford FlexAL remote plasma system. Silicon  $\langle 100 \rangle$  substrates involved were coated by an

insulating layer. The plasma parameters in the ALD cycle were varied one at a time to observe their effects on resistivity. An SEM/ellipsometer and four-point probe were used to record results.

## Results and Discussion:

**Plasma Power.** The dependence of resistivity on plasma power was studied. Increased plasma power enhances film density by compacting layers [1] and more completely removing ligands contained in TDMAT. The denser film prevents oxygen diffusion into the material upon exposure to atmosphere [2, 3] preventing the formation of  $\text{TiO}_2$  and other compounds that increase the resistivity [2, 4]. Plasma power increased to the maximum allowed of 500W provided the lowest resistivity.

**Plasma Composition.** The dependence of plasma composition was studied and results are listed in Figure 2. A stoichiometric ratio of 1:3 N:H was found to be optimal. Implementing this ratio in  $\text{N}_2/\text{H}_2$  plasma yielded the lowest resistivity for any combination. Preserving this stoichiometric ratio,  $\text{NH}_3$

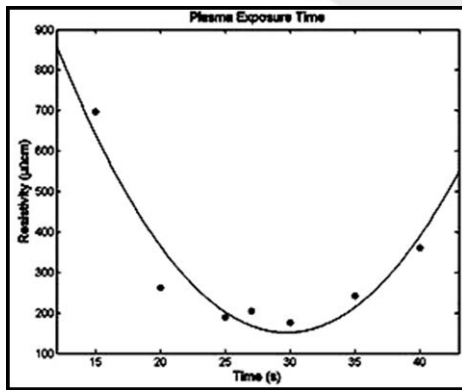


Figure 3: The effect of plasma exposure time on resistivity.

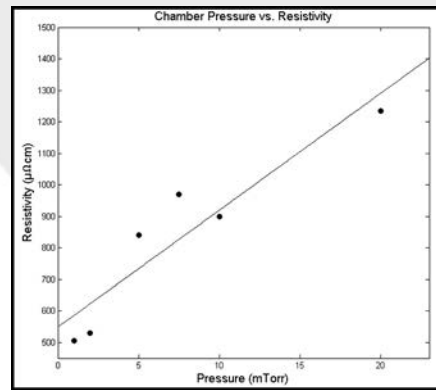


Figure 4: Chamber pressure effects on resistivity.

was also used, which yielded a lower resistivity. A possible explanation for this is that more  $\text{NH}_x$  radicals are formed [5].

**Plasma Time.** The duration of the plasma was found to have a significant impact on the resistivity. As Figure 3 shows, the effect of timing exhibits a parabolic like effect on the resistivity. Short timing can lead to greater carbon contamination while longer timing gives higher resistivity also, possibly due to plasma damage. An ideal time of 30 seconds was experimentally determined to give the lowest resistivity.

**Chamber Pressure.** For the first time, chamber pressure was varied during the plasma exposure and effect on resistivity studied. A trend was observed that has you decrease chamber pressure the resistivity is significantly lowered. This is shown in Figure 4.

Combining all optimal parameters described above, the minimum TiN film resistivity achieved was  $175 \mu\Omega\text{cm}$  for a 35 nm thick film. The optimal process determined is outlined below:

1. Dose TDMAT: 2 seconds, 200 mT, 100 sccm Ar
  2. Purge TDMAT: 5 seconds, 20 mT, 200 sccm Ar
  3. Pump TDMAT: 5 seconds
  4. Plasma Dose: 30 seconds, 2 mT, 10 sccm  $\text{NH}_3$ , 500W
  5. Purge  $\text{NH}_3$ : 5 seconds, 20 mT, 200 sccm Ar
  6. Pump  $\text{NH}_3$ : 4 seconds
- Repeat.

## Conclusions:

The effects of chamber pressure and a review of additional plasma parameters on ALD TiN film resistivity were studied. It was found that  $\text{NH}_3$  plasma as a precursor more effectively reacts with TDMAT. Increased plasma power and plasma exposure time ( $t < 30$  seconds) decrease film resistivity due to a denser film. Combining all optimized parameters, a resistivity of  $175 \mu\Omega\text{cm}$  for a 35 nm thick film was realized. Denser, less resistive, ALD TiN films have many advantages for future integration into microelectronic devices.

## Acknowledgements:

This study was funded by the National Nanotechnology Infrastructure Network Research Experience for Undergraduates (NNIN REU) Program with the support of the National Science Foundation (NSF). The author thanks Robert Maurer, Prakteek Choudhary, Mark Rodwell, Bill Mitchell, and Brian Markman for their many helpful suggestions.

## References:

- [1] S. Chang, et al., Surface and Coating Technology, 203, (2008).
- [2] H. Kim, JVSTB, 21, (2003).
- [3] G. Cho and S. W. Rhee., JVSTA, 31, (2013).
- [4] J. Musschoot, et al., Microelectronic Engineering, 86, (2009).
- [5] M. Hua, et al., Wear, 260, 11-12 (2006).

# Aluminum-Induced Crystallization of Amorphous Silicon on Patterned Substrates

Jon-L Innocent-Dolor  
Chemical Engineering, Syracuse University

**NNIN REU Site:** Penn State Nanofabrication Laboratory, The Pennsylvania State University, University Park, PA  
**NNIN REU Principal Investigator:** Dr. Joan Redwing, Materials Science Department, The Pennsylvania State University  
**NNIN REU Mentor:** Mel Hainey, Jr., Materials Science Department, The Pennsylvania State University  
**Contact:** inohill@gmail.com, jmr31@psu.edu, melhaineyjr@gmail.com

## Abstract and Introduction:

Aluminum-induced crystallization (AIC) has become an attractive method of fabricating polycrystalline silicon on insulating substrates because of its ability to produce thin films with uniform surface orientations [1], and its low process temperatures ( $< 500^{\circ}\text{C}$ ), which make the use of much cheaper substrates such as glass possible. One drawback of current methods is that they tend to produce films with high-angle grain boundaries. By using patterned substrates to align the grains in the films we hope to minimize the presence of high angle grain boundaries which tend to act as defects and can inhibit future device performance.

Previous studies on patterned quartz substrates made with fluorine-based reactive ion etching showed increased crystallization rate in the patterned regions, but the preferential orientation was lost. It was found that the patterned surfaces were significantly rougher than the unpatterned surfaces, which may have led to the loss of preferential orientation. This work examines the effect of surface roughness on crystallization rate and orientation.

Samples with higher and lower patterned region surface roughness were prepared by using contact lithography and fluorine and chlorine-based plasma etches, respectively. Aluminum and amorphous silicon (a-Si) layers 30 nm thick were deposited by electron-beam evaporation, and then AIC was performed by annealing the samples below the Al/Si eutectic temperature, at temperatures between  $400^{\circ}\text{C}$

and  $500^{\circ}\text{C}$ . *In situ* and post anneal optical microscopy were used to determine the effect of patterning and roughness on crystallization and grain size. We hypothesize that the smoother surface will be better able to preserve preferential crystal orientation while maintaining the increased crystal growth rate.

## Experimental Procedure:

**Patterning.** Fused quartz substrates were cleaned by sonication in acetone, isopropanol and de-ionized (DI) water followed by Nanostrip<sup>®</sup>. The cleaned samples were spin-coated with 3012 resist, then; contact lithography was used to produce line patterns with spacings of 100, 75, 50 and 25  $\mu\text{m}$  (Figure 1). The samples were etched to a depth of 25 nm using reactive-ion plasma etch with fluorine-based etch and chlorine-based etch in order to produce samples with higher and lower surface roughness respectively. After etching, the resist was removed using acetone, isopropanol and DI water, then atomic force microscopy (AFM) was used to characterize the surface roughness of the samples and contact profilometry was used to determine the etch depth.

**Deposition and Annealing.** Using e-beam evaporation, 30 nm of aluminum was deposited on the etched samples, then the samples were exposed to air for 30 minutes in order to form a thin oxide layer before 30 nm of amorphous silicon was deposited onto the samples. The fused quartz substrates were diced and separated by line spacing and etch type. Anneals were performed in an annealing furnace in ambient nitrogen at  $450^{\circ}\text{C}$  for four hours on samples, and then an aluminum etchant (hydrochloric, acetic and nitric acid mixture) was used to remove the aluminum layer before optical microscopy was used to view the polycrystalline silicon layer. In order to study differences in crystallization between chlorine and fluorine etched samples, *in situ* optical microscopy was performed using a heating stage with a viewing window. Samples were again annealed at  $450^{\circ}\text{C}$  in ambient nitrogen and, images were captured every 30 seconds over the annealing period.

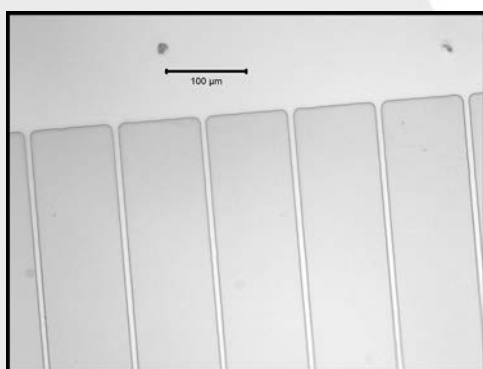


Figure 1: Optical micrograph of 100  $\mu\text{m}$  patterned region.

M  
A  
T  
S

## Results:

The chlorine-based plasma etch was found to produce a surface that was much smoother (RMS 3.02 nm) than the fluorine based etch (RMS 6.88 nm) — comparable to the roughness of an unetched substrate (2.96 nm (Figure 2)). For the chlorine etched samples, at a line spacing of 50  $\mu\text{m}$ , there seemed to be no effect of patterning on crystallization, but 25  $\mu\text{m}$  line spacing seemed to cause some grain confinement in the patterned region. Similarly, for the fluorine-based etched samples, the 25  $\mu\text{m}$ -spaced line pattern had a greater effect on crystallization than the 50  $\mu\text{m}$ -spaced line pattern. In both cases, however, the fluorine-based etch showed a much more dramatic effect of patterning on crystallization, with the 25  $\mu\text{m}$  pattern causing almost continuous growth in the direction of the line pattern (Figure 3).

*In situ* optical microscopy (Figure 4) revealed that for chlorine-etched samples, nucleation began simultaneously in and out of the patterned region, but the growth rate for crystals was faster within the patterned region. Conversely, for fluorine-etched samples, nucleation occurred mainly along the lines between etched regions where there seemed to be a faster crystallization rate than the patterned region. This caused the crystals to first grow along lines, then, spread outward into the etched region, leading to the near-continuous crystals and periodicity seen in the fluorine-etched samples.

## Conclusions and Future Work:

Smaller line spacing and fluorine etching seems to promote grain alignment with pattern. This result shows that patterned substrates could potentially be used to align grains. Orientation imaging microscopy will be used in order to determine the effect of surface roughness on the surface orientation. Further on, we hope to use these patterned substrates as templates for the growth of nanowires and other substances such as GaN [2].

## Acknowledgements:

I would like to thank my mentor Mel Hainey, Jr. for his guidance, support and help keeping me on track with my research, my Principal Investigator Dr. Joan Redwing for welcoming me into her lab, Kathleen Gehoski for coordinating my stay at PSU and the entire Nanofab staff at PSU. I would also like to thank the NNIN REU Program and the National Science Foundation for funding this research.

## References:

- [1] M. Kurosawa, N. Kawabata, T. Sadoh, and M. Miyao, 2009. Orientation-controlled Si thin films on insulating substrates by Al-induced crystallization combined with interfacial-oxide layer modulation Appl. Phys. Lett. 95, 132103.
- [2] D. Tsukada, Y. Matsumoto, et al., 2009. Fabrication of (1 1 1)-oriented Si layers on SiO<sub>2</sub> substrates by an aluminum-induced crystallization method and subsequent growth of semiconducting BaSi<sub>2</sub> layers for photovoltaic application, Journal of Crystal Growth, 311 (14): 3581-3586.

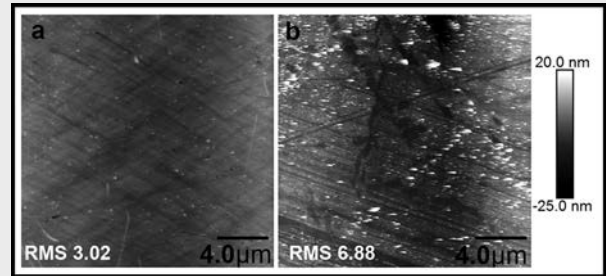


Figure 2: AFM scans; (a) chlorine-based etch, and (b) fluorine-based etch.

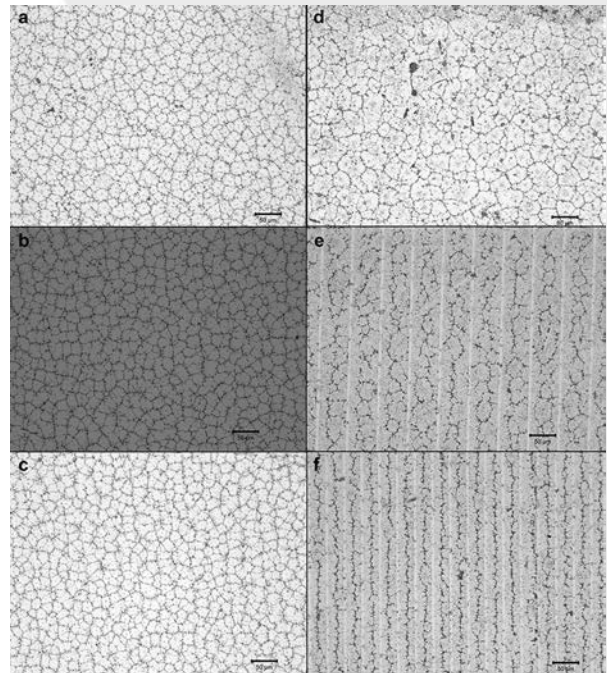


Figure 3: (a) Chlorine etch unpatterned, (b) chlorine etch 50  $\mu\text{m}$  pattern, (c) chlorine etch 25  $\mu\text{m}$ , (d) fluorine etch unpatterned, (e) fluorine etch 50  $\mu\text{m}$ , and (f) fluorine etch 25  $\mu\text{m}$ .

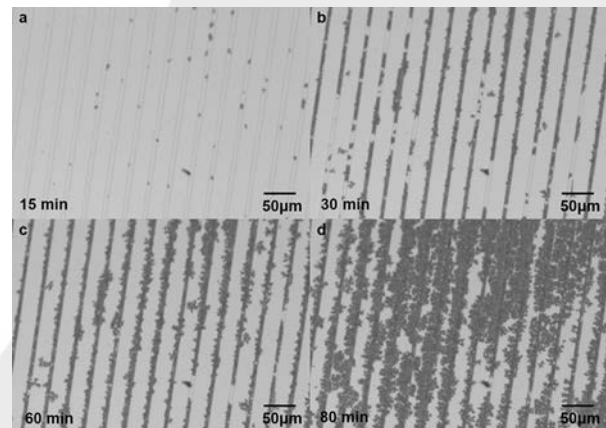


Figure 4: In situ micrographs of chlorine-etched 50  $\mu\text{m}$  line patterned samples during anneal showing difference in growth rate between patterned and unpatterned region.

# Fabrication of Low-Density Vertically Aligned CNT Forests

Yasuhiro Kimura

Mechanical Engineering, Tohoku University, Japan

NNIN iREG Site: Institute for Electronics & Nanotechnology, Georgia Institute of Technology, Atlanta, GA

NNIN iREG Principal Investigator: Prof. Baratunde A. Cola, Mechanical Engineering, Georgia Institute of Technology

NNIN iREG Mentor: Dr. Virendra Singh, Mechanical Engineering, Georgia Institute of Technology

Contact: kimura@ism.mech.tohoku.ac.jp, cola@gatech.edu, vsingh@gatech.edu

## Abstract:

Carbon nanotubes (CNT) are a tubular nano-material made of carbon atoms and utilized by some applications due to its remarkable characteristics. The effect of growth conditions on the morphology of the CNT has been investigated for the correlation of morphology and characteristics. In the present work, the effect of growth parameters—including catalyst element, plasma properties, and the thickness of catalyst layer—on the morphology of CNT was studied to fabricate low-density CNT forests. As a result, we successfully demonstrated the fabrication of low-density CNT forests by optimizing growth parameters. The low-density CNT forests were fabricated by using 5-nm-thick nickel catalyst via low pressure chemical vapor deposition (LPCVD).

## Introduction:

Carbon nanotube (CNT) is composed of one or several graphene sheets rolled into a tube and has nanoscale diameter [1]. Several noticeable characteristics of CNT, e.g. high thermal and electrical conductivity, attract increasing attention and are applied to generate the devices with outstanding performance. One of the applications of CNT is the diode array [2], which was developed by the NanoEngineered System and Transport (NEST) laboratory at the Georgia Institute of Technology. A diode array that consists of a metal-oxide-metal structure based on CNTs is capable of rectification at ultrahigh-frequencies. Conversely, this device requires low-density CNT forests for fabricating the robust device with curable resin and improving performance.

Generally, CNTs are fabricated using catalyst via chemical vapor deposition (CVD), and the morphology of CNT depends on growth conditions of CVD and surface conditions [3]. Growth conditions are plasma properties, the gases used for carbon source and facilitating CNT growth, catalyst elements, particle sizes of catalyst, structures under catalyst, etc. In this work, we focused on three parameters—catalyst element, existence of plasma, and catalyst size—for fabricating low-density CNT forests, because the listed parameters are assumed dominant to morphology of CNT and are easy to control.

The primary objective of this study was the investigation of the effect of the above parameters on the morphology of the CNT growth and fabrication of low-density CNT forests. Nickel (Ni) and iron (Fe) were used as different types of catalyst elements. LPCVD and plasma-enhanced CVD (PECVD) were used as different plasma properties. Additionally, 3, 5 and 7-nm-thick catalysts were used as different particle size of catalyst because the catalyst particle size is involved in catalyst layer thickness.

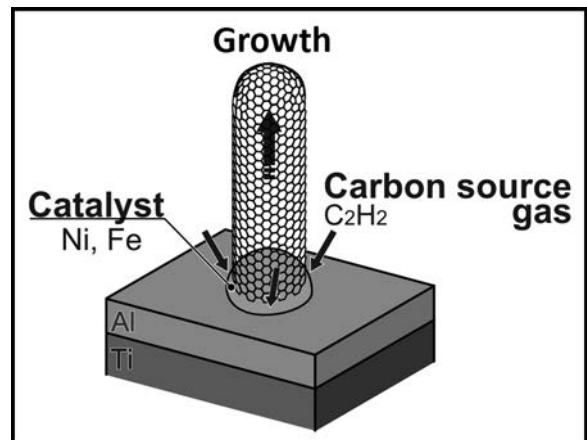


Figure 1: Schematic of CNT base-growth by CVD.

## Experimental Procedure:

The fabrication process of the sample for CNT growth is given herein. Using electron-beam evaporator, 30-nm-thick Ti, 10-nm-thick Al were serially deposited as under layers onto a Si wafer. The catalyst layer, which had corresponding thickness and was composed of Ni or Fe, was formed for shaping different sizes of the catalyst particles. The CNTs were grown by using different growth conditions through CVD techniques as base-growth model, as shown in Figure 1.

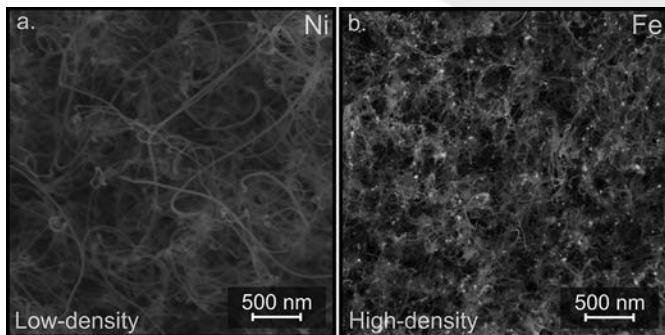


Figure 2: FE-SEM images of CNT morphology using different catalyst element; (a) Ni and (b) Fe.

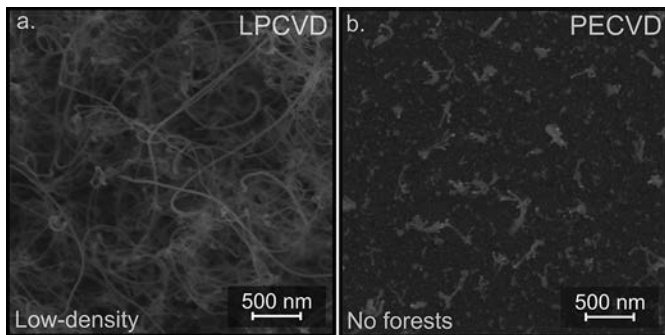


Figure 3: FE-SEM images of CNT morphology using different plasma properties; (a) LPCVD and (b) PECVD.

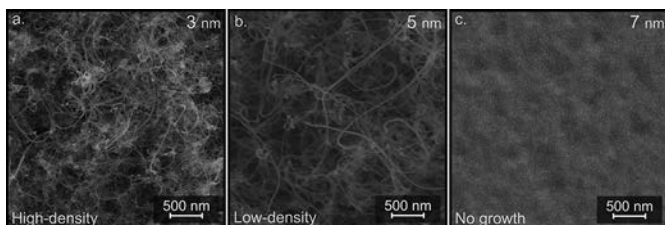


Figure 4: FE-SEM images of CNT morphology using different thickness; (a) 3 nm, (b) 5 nm and (c) 7 nm.

## Results and Conclusions:

**Effect of Catalyst Element.** Figure 2 shows field emission scanning electron microscope (FE-SEM) images of CNT forests formed by using different catalyst elements. Other parameters of CNT growth are as follows: 10 min of growth time, LPCVD as growth technique, and 5-nm-thick of catalyst. As a result, the use of Ni catalyst contributed to fabricate low-density CNT forests. On the other hand, when Fe was utilized as a catalyst, the density of CNT forests was higher than the one using Ni catalyst.

**Effect of Plasma Properties.** Figure 3 shows FE-SEM images of CNT forests fabricated by using different plasma properties. Other parameters of CNT growth are as follows:

10 min of growth time, Ni as catalyst element, and 5-nm-thick of catalyst. LPCVD is suitable for growing low-density CNT forests. No CNT forests were grown using plasma, PECVD, as shown in Figure 3 (b). Normally, the plasma facilitates the CNT growth and enables CNT growth at low temperatures, but the use of plasma did not contribute to expedited CNT growth, in the case of this study. The cause of non-formation of CNT forests by using plasma is assumed that the plasma etched the catalyst particle and deposited carbon before it became a vertically aligned CNT.

**Effect of Catalyst Layer Thickness.** Figure 4 shows FE-SEM images of CNT forests grown by using different catalyst thicknesses. Other parameters of CNT growth are as follows: 10 min of growth time, Ni as catalyst element, and LPCVD as growth technique. The thickness of catalyst involves the particle size of catalyst as described above, and the correlation between particle size and the density of CNT is expected to be inverse proportion. In fact, the dependence between thickness involved in particle size and the density of CNT is indicated as shown in Figure 4. Nevertheless, 7-nm-thick Ni is unsuitable to fabricate low-density CNT because the film was formed with increasing thickness and particle size.

The growth and morphology of CNT were varied by different growth parameters. Consequently, the formation of low-density CNT forests can be demonstrated by using 5-nm-thick Ni catalyst via LPCVD.

## Future Work:

In the future, we plan infiltrated low-density CNT forests with curable resin for the design and fabrication of CNT-based robust electronic devices.

## Acknowledgements:

This work was supported by National Nanotechnology Infrastructure Network International Research Experience for Graduates (NNIN iREG) Program and National Institute for Materials Science. Part of this work was performed at the Institute for Electronics and Nanotechnology of Georgia Institute of Technology. I appreciate the support by Prof. Baratunde A. Cola, Dr. Virendra Singh, and laboratory members of NEST.

## References:

- [1] Scarselli, M., Castrucci, P. and Crescenzi, M. De; J. Phys., Condens. Matter., 24, 313202 (2012).
- [2] Cola, B.A., Sharma, A. and Singh, V.; U.S. Patent, WO/2014/063149, 04/24/2014.
- [3] Chhowalla, M., et al.; J. Appl. Phys., 90, 5308 (2001).

# Synthesis, Device Fabrication, and Characterization of Two-Dimensional Transition Metal Dichalcogenides

Matthew Koehler  
Mechanical Engineering, The University of Saint Thomas

NNIN REU Site: Penn State Nanofabrication Laboratory, The Pennsylvania State University, University Park, PA

NNIN REU Principal Investigator: Professor Joshua Robinson, Department of Materials Science and Engineering, The Pennsylvania State University

NNIN REU Mentor: Brian Bersch, Department of Materials Science and Engineering, The Pennsylvania State University

Contact: koeh7692@stthomas.edu, jrobinson@psu.edu, bmb5382@gmail.com

## Abstract:

Semiconducting two-dimensional transition metal dichalcogenides (TMDs), in particular molybdenum disulfide ( $\text{MoS}_2$ ) and tungsten diselenide ( $\text{WSe}_2$ ), have been the focus of intense research in recent years for their potential use in next-generation, scaled down electronic and optoelectronic devices due to their unique chemical, optical, and mechanical properties. TMDs are an excellent material candidate to replace silicon in digital CMOS technology, yet there still exists a need for optimized device fabrication and a scalable growth process for controllable large area, single-crystalline films. This project focused on two main objectives:  $\text{WSe}_2$  device fabrication for Hall mobility measurements and the construction of a new metal organic chemical vapor deposition (MOCVD) system for advanced material synthesis of  $\text{MoS}_2$ . Van der Pauw structures were fabricated by photolithography, inductively coupled reactive-ion plasma etching, and metal thin film deposition by e-beam evaporation. Devices were fabricated on several  $\text{WSe}_2$  samples of varying morphology and were characterized by field emission scanning electron microscopy, profilometer, and Raman spectroscopy. A fully functional MOCVD system equipped with metal organic precursor “bubbler” chambers was designed and fabricated to be used for synthesis of  $\text{MoS}_2$ .

## Introduction:

Mono- and few-layered  $\text{WSe}_2$  devices possess properties such as transparency, high flexibility, direct or indirect bandgap, high  $I_{\text{ON}}/I_{\text{OFF}}$  ratio, near-perfect subthreshold swing, and high field effect mobility [1]. This material, if proven scalable and robust to conventional nanofabrication techniques, could yield a more efficient, low cost and high quality semiconductor material for industrial fabrication. We used standard photolithography to make three types of devices to test this.

Mono- or few-layered TMDs have been predominantly obtained by mechanical exfoliation from bulk crystals or powder precursor CVD. Mechanical exfoliation is not a high-throughput, scalable method while powder precursor CVD has issues precisely controlling layer thickness, uniformity, island growth, grain size, and unwanted deposition of metallic or metal oxide particulates. Modifying the currently used powder precursor CVD to a MOCVD system would greatly reduce these issues and also be compatible with existing silicon microelectronics manufacturing.

## Experimental Procedure:

An exposure mask for the lithography process was designed using L-Edit, a computer aided design software, and fabricated by a laser writer. The created mask contained the layout for three devices; dual gated radio frequency field effect transistors (FET), van der Pauw structures (vdP), and transmission line measurement devices (TLM). Three successive iterations

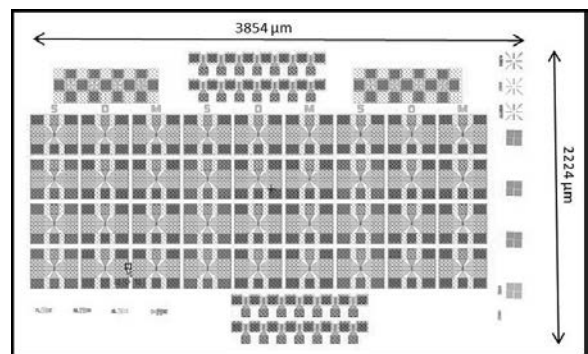


Figure 1: Exposure mask device design layout.

of photolithography were performed in order to fabricate the following layers: alignment mark layer, isolation ( $\text{WSe}_2$  etch) layer for defining the active channel regions, and ohmic (source/drain) layer to define the contacts. A bilayer resist stack was used for lift-off of both alignment mark and contact layers. Ten nanometers of titanium (Ti) and 100 nm of gold (Au) were deposited using e-beam evaporation. A single resist layer was used for the isolation layer, and an oxygen based dry etch was successfully developed.

Constructing the MOCVD system consisted of common metal assembly tasks such as tightening bolts, joining brackets and drilling screws to assemble the frame and fasten the gas panel components. The gas lines were fully purged and evacuated

before orbital welding was performed to route the gas lines to the furnace and create a higher quality smoother weld bead. The switch box was wired by both soldering and terminal block connectors.

### Results:

After each layer, devices were examined by optical microscope and field-emission scanning electron microscope (FESEM). Fortunately,  $WSe_2$  films that are bonded to the substrate by van der Waals forces remained on the substrate even with exposure to various solvents and chemicals throughout processing, which is reassuring for future device fabrication. The majority of the devices had a visible, defined channel region shown in Figure 2. However, each device had a lack of continuous coverage in the  $WSe_2$  channel region also shown in Figure 2, which obviates the need for more uniform, wafer-scale TMD growth.

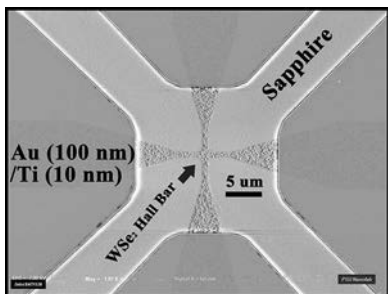


Figure 2: Finished vdP device.

A fully functional MOCVD system was designed and built, shown in Figures 3 and 4. Over 150 parts/components were ordered to create the three bubbler input system allowing multiple metal organic precursors to be used in TMD synthesis. Each bubbler has a mass flow controller and three pneumatic actuators controlled by the switchbox. Each bubbler temperature can be controlled individually by the temperature readouts on the right side of the switchbox. The user is protected by the fully ventilated sheet metal and Plexiglass® sliding door enclosure.

### Conclusions:

$WSe_2$  proved to be a robust and compatible material for scalable device nanofabrication. In addition, it was found that  $WSe_2$  is easily etched by an oxygen plasma and remains on the substrate throughout the fabrication process.

Even though the measurements were not taken from the vdP devices, the fabrication steps to

making the devices will help future  $WSe_2$  research. Scientific investigators can continue to use the exposure mask and fabrication steps knowing they can achieve functioning devices if coalesced and continuous  $WSe_2$  films are successfully grown.

The new MOCVD system will contribute to future molybdenum disulfide ( $MoS_2$ ) research for many years to come. The system will allow the operator to precisely control various parameters of material synthesis to create uniform films. Readouts will give an exact flow rate for each bubbler and precursor allowing for easier repeatability and reliability. Ultimately, the new system will aid in the synthesis of uniform, large-area  $MoS_2$ , which will not only assist in device fabrication within the group, but also shed light on  $MoS_2$  integration in manufacturing.

### Acknowledgments:

I would like to thank Prof. Joshua Robinson, and Brian Bersch, along with Dr. Sarah Eichfeld and the Robinson research group for their guidance this summer. I'd also like to thank the National Nanotechnology Infrastructure Network Research Experience for Undergraduates (NNIN REU) Program and the National Science Foundation (NSF) for making this experience possible.

### References:

- [1] Z. Weijie, et al., "Evolution of Electronic Structure in Atomically Thin Sheets of  $WSe_2$  and  $WSe_2$ "; arXiv. Org, Cornell University Library.

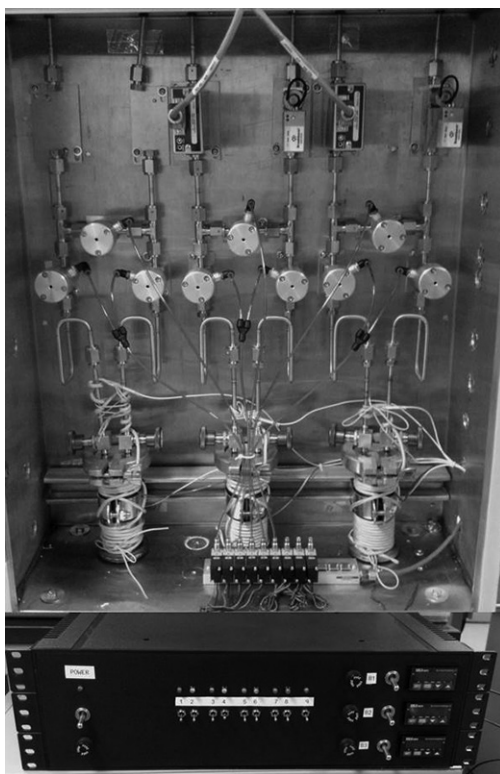


Figure 3, left: Finished MOCVD gas panel and switch box. Figure 4, right: Fully ventilated protective enclosure.

M  
A  
T  
S

# Growth of Boron Nitride for Two-Dimensional Applications

Tewa Kpulun

Physics and Math, Vassar College

*NNIN REU Site: Howard Nanoscale Science & Engineering Facility, Howard University, Washington, DC*

*NNIN REU Principal Investigator: Dr. Gary L. Harris, Nanoscale Science and Engineering, Howard University*

*NNIN REU Mentor: Dr. William Rose, Nanoscale Science and Engineering, Howard University*

*Contact: tekpulun@vassar.edu, gharris1124@gmail.com, wbullrose@gmail.com*

## Abstract:

Boron nitride (BN) is an isoelectronic compound similar to carbon that is sometimes referred to as white graphene. It has several applications due to its excellent chemical properties and thermal stability. BN has weak van der Waals forces between its layers which makes it, like graphene, an excellent self-lubricant. However for certain applications, including but not limited to space applications, it is preferable to graphene. The objective of this project was to grow BN on thin substrates using a horizontal chemical vapor deposition (HCVD) system under high temperatures and pressures. Our precursors were diborane ( $B_2H_6$ ) and ammonia ( $NH_3$ ), while our substrates were sapphire ( $\alpha-Al_2O_3$ ) and silicon carbide (SiC). After growth, these samples were characterized using Raman spectroscopy, atomic force microscope (AFM), and the scanning electron microscope (SEM).

## Introduction:

Boron nitride (BN) is a compound that is isoelectronic to carbon; instead of carbon atoms, its lattice structure contains an equal number of boron and nitrogen atoms. It can be found in three different forms: nanosheets (BNNS), nanoribbons (BNNR), and nanomeshes (BNNM). There are four different types of BN; amorphous ( $\alpha$ -BN), cubic (c-BN), wurtzite (w-BN), and hexagonal (h-BN).

This project mainly focused on h-BN, because it's the most stable form of BN. Its structure is similar to graphene, hence h-BN is sometimes referred to as white graphene. h-BN has strong covalent bonds between the boron and nitrogen atoms with weak van der Waals forces between its layers. This makes it an excellent lubricant with applications in cosmetics and bullet coating, and several space applications.

Using diborane and ammonia as our precursors, we attempted to grow BN on sapphire and silicon carbide substrates. Growing BN is a difficult process, thus several different methods were used to achieve our objectives.

## Experimental Procedures:

First, we had to cut the  $\alpha-Al_2O_3$  into smaller sizes. We used an available laser with a 1050 nm wavelength. Ideally, to cut through  $\alpha-Al_2O_3$ , a laser of wave length 1070 nm is require. We were unable to cut through the material, but the laser produced several striations on the back part of the whole sample. This sufficiently weaken the material allowing us to complete the cutting process with diamond tip scribes. The samples were then cleaned using standard RCA cleaning procedures.

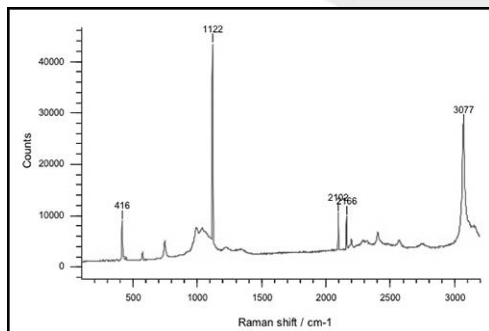


Figure 1: HCVD system. Temperatures can go as high as 1800°C and pressures as high as 400 Torr. (See full color version on page xxxvi.)

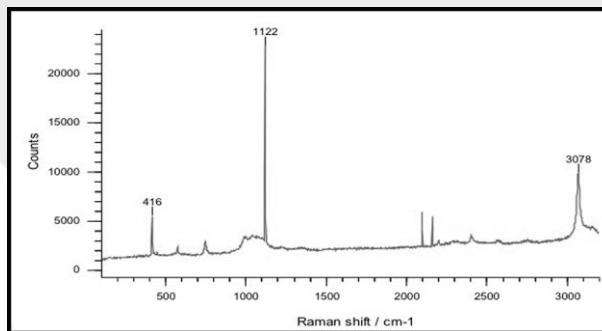
Next was the growth process where we used a horizontal chemical vapor deposition system (HCVD). The HCVD system allowed us to grow several samples on different substrates using different precursors. As you can see in Figure 1, there is a coil-like structure around the furnace that produces electromagnetic fields, which in turn creates a current that allows the device to heat up to temperatures as high as 1800°C. Pressures of about 400 Torr were also observed.

## Methods and Results:

Several attempts to grow BN were made without success. We varied many of the parameters (for instance, time, amount of each precursor, and etching time) but were unable to



Graph 1: No-growth sapphire sample.



Graph 2: Sapphire growth in 1050°C.

successfully grow graphene. We used temperatures at 1000°C and 1050°C with a growth time of 15 minutes and 30 minutes. The precursor values differed from 10 sccm to 100 sccm for diborane, and 180 sccm to 200 sccm for ammonia with 9 slm for hydrogen. After each growth period, the samples were observed using Raman spectroscopy. The expected value for BN is about 1300  $\text{cm}^{-1}$  and our results showed Raman graphs with 1122  $\text{cm}^{-1}$  peaks. With this device, it was very easy to determine if the parameters we used produced expected results. Before using the Raman spectroscopy, we scanned a normal sample and compared it to that of a sample after growth; as you can see in Graphs 1 and 2.

After several attempts and additional research, we determined that having a longer growth period and higher temperatures would probably help us achieve our goal. We also characterized our samples using SEM and AFM systems. In the SEM, we used the energy dispersive spectroscopy (EDS) to determine what was on the samples' surfaces after growth. The sapphire samples showed evidence of aluminum and oxygen and the SiC showed evidence of silicon and oxygen. An AFM was used to compare the surfaces of our samples to that of previous research.

### Conclusions and Future Steps:

After several attempts, there was no evidence of BN on any of the substrates. The Raman shift of a clean substrate was exactly the same as that of a substrate upon which growth had been attempted.

The next step towards growing BN on sapphire is to use other precursors instead of diborane, such as triethylboron.

Using this precursor would require using a metalorganic chemical vapor deposition system because triethylboron is a metalorganic substance. We could also continue to extend the growth period and increase the temperature.

### Acknowledgments:

I would like to thank Mr. Crawford Taylor, Dr. William Rose, Dr. Gary Harris, Gurpreet Kaur, Mr. James Griffin, the Howard Nanoscale Science and Engineering Facility, and the National Nanotechnology Infrastructure Network Research Experience for Undergraduates (NNIN REU) Program.

### References:

- [1] Bresnehan, S. Michael. Prospects of Direct Growth Boron Nitride Films as Substrates for Graphene Electronics. <http://arxiv.org/pdf/1310.1870.pdf>.
- [2] Cubarovs, Mihails. CVD growth of sp<sup>2</sup>-hybridized boron nitride using aluminum nitride as buffer layer. 2011. <http://iu.diva.portal.org/smash/get/diva2:467821/FULLTEXT01.pdf>.
- [3] Ismach, Ariel. Toward the Controlled Synthesis of Hexagonal Boron Nitride Films. 18 June 2012. <http://pubs.acs.org/doi/abs/10.1021/nn301940k>.
- [4] Paduano, Qing. Self-terminating growth in hexagonal boron nitride by metal organic chemical vapor deposition. 9 June 2014. <http://m.iopscience.iop.org/1882.0786/7/7/071004/article>.
- [5] Senthilingam, Meera. Boron Nitride. 17 December 2013. <http://www.rsc.org/chemistryworld/2013/12/boron-nitride-podcast>.



# Investigation of Nanodiamond Foil Product for H- Stripping to Support Spallation Neutron Source

Rachel Lim  
Materials Science, Rice University

NNIN REU Site: Howard Nanoscale Science & Engineering Facility, Howard University, Washington, DC

NNIN REU Principal Investigator: Dr. Gary Harris, Electrical Engineering, Howard University

NNIN REU Mentor: Mr. James Griffin, Electrical Engineering, Howard University

Contact: rel3@rice.edu, gharris@msrce.howard.edu, griffin@msrce.howard.edu

## Abstract:

Diamond is an ideal material as an H- stripper foil for spallation neutron source (SNS) applications due to its high thermal conductivity, low molecular weight, and strength. Polycrystalline diamond is characterized by a high degree of internal stress, which causes the foil to curl when not supported by the substrate. Hot filament chemical vapor deposition (HFCVD) was used to grow diamond on a silicon substrate. A 1.2 cm diameter window was etched in the silicon using a 1:1:3 solution of hydrofluoric, nitric, and acetic acids, so that the diamond foil would be suspended while being supported on all sides by the silicon. Wax and diamond were used as masks to protect the outer silicon from etching. Raman spectroscopy verified a high quality diamond foil. Atomic force microscopy (AFM) revealed that the foil originally against the substrate had an average roughness of 6.7 nm while the foil away from the substrate had an average roughness of 13.2 nm. Scanning electron microscopy (SEM) revealed no cracks in the suspended foil.

## Introduction:

SNS is a process that produces intense neutron beams for research. An ion source produces H<sup>-</sup> ions, hydrogen atoms with two electrons, which are injected into a linear particle accelerator. The ions pass through a foil that strips them of their electrons, yielding protons. The protons are collected in accumulator ring, then released in high energy pulses towards a liquid mercury target. Neutrons are ejected from the mercury target upon impact, which can be used for different experiments.

Currently, a carbon stripper foil is being used, but diamond would be an ideal foil. It would be able to withstand the high energy radiation because of its high thermal conductivity, low molecular weight, and strength. The foil would not have to be changed as often because diamond is more durable than just carbon.

## Experimental Procedure:

A piece of <100> silicon was seeded with a nanodiamond slurry solution for ten minutes in an ultrasonic bath, then the sample was loaded into the HFCVD reactor. The working distance between the filaments and the sample was set to 20 mm, the process pressure was set to 20 torr, and the diamond heater was set to 750°C. A flow of 80.0 sccm of H<sub>2</sub> and 1.0 sccm of CH<sub>4</sub> was introduced, and when the process pressure reached 20 torr and the diamond heater temperature reached 650°C, the filament temperature was raised to 2350°C. The nanodiamond film was left to grow for 6-8 hours.

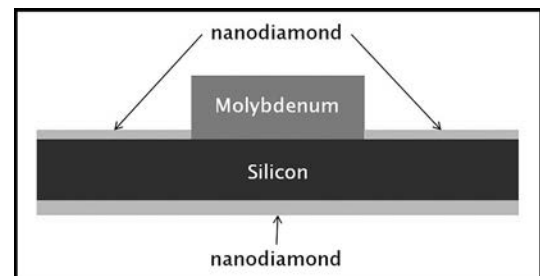


Figure 1: The circular piece of molybdenum placed in the center of the sample.

After growth of the top foil layer, the sample was flipped over, and a circular piece of molybdenum was placed in the center of the sample (see Figure 1). A diamond layer for etch masking was grown on the backside for two hours with conditions similar to the topside foil layer. The molybdenum prevented diamond from growing on part of the backside of the sample. Some of the samples were annealed at 600°C for 20 hours in a 5.0 sccm flow of N<sub>2</sub> at a process pressure of 20 torr in an attempt to reduce the internal stresses in the diamond foil.

The sample was placed in a 1:1:3 solution of 48% hydrofluoric, 70% nitric, and 100% acetic acids to etch a window in the silicon. The ratio of acids determined the etch rate. If the etch was too fast, the diamond came off in little pieces. If the etch was too slow, it did not etch all the way through the silicon. The backside layer of diamond protected the silicon outside of the circle from the etch, yielding a suspended diamond foil

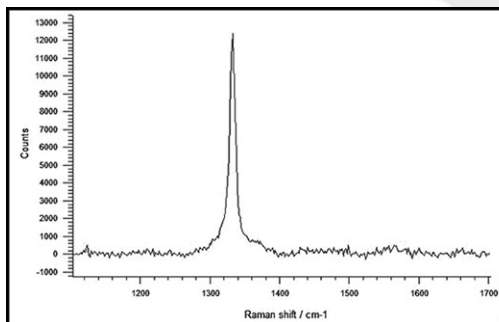


Figure 2: Raman spectroscopy verifying a high quality diamond foil with a strong diamond peak and a very weak graphite peak.

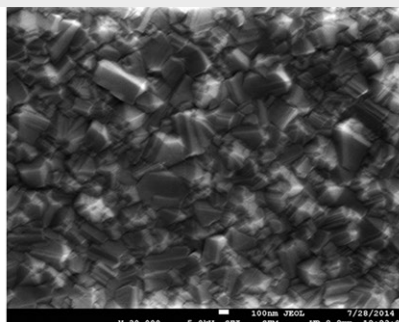


Figure 3: SEM image verifying the presence of polycrystalline diamond.

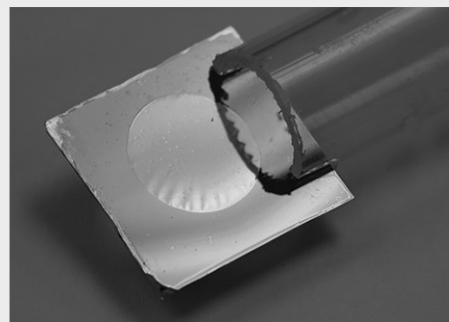


Figure 4: Optical imaging reveals no cracks in the suspended foil. (See full color version on page xxxvi.)

that was supported by the silicon. Once all of the silicon in the circle was etched away, the sample was rinsed in DI water, then allowed to air dry.

## Results and Conclusions:

A high quality diamond foil was grown on a  $\langle 100 \rangle$  piece of silicon by HFCVD. Raman spectroscopy verified a high quality diamond foil with a strong diamond peak at  $1333 \text{ cm}^{-1}$  and a very weak graphite peak as seen in Figure 2. Both SEM and AFM showed the presence of polycrystalline diamond as seen in Figure 3. A 1:1:3 acid ratio was found to be ideal because it was not too fast or too slow. Using diamond as a mask to protect the silicon during etching worked better than wax by providing better mask control and greater resistance to acid etching. AFM revealed that the foil originally against the substrate had an average roughness of 6.7 nm, while the foil away from the substrate had an average roughness of 13.2 nm.

SEM and optical imaging (see Figure 4) revealed no cracks in the suspended foil. Both 6-hour diamond film growths did not crack. The annealed sample appeared to be smoother, which means that it had less internal stress. The 8-hour unannealed diamond film growth cracked, while the 8-hour annealed film growth did not. It appears that annealing the diamond foil before etching away the silicon relieves some of the stresses in the film.

## Future Work:

Currently, the diamond foils that have been grown are under much internal stress. Initial results suggested that pre-etching annealing of the diamond is useful for relieving internal stress. Future work should concentrate on various anneal temperature and times for stress reduction. Another area of investigation should involving introducing argon to the gas species during

diamond growth. Depending on the argon concentration during growth, diamond grains can be reduced from poly to nanocrystalline. Smaller grains may also reduce the stress in the film. Lastly, foil testing by SNS should be performed to verify diamond foil performance.

## Acknowledgements:

I would like to thank the NNIN REU Program, the NSF, and the Howard Nanoscale Facility (HNF). I would also like to thank my PI, Dr. Gary Harris, and my mentor, Mr. James Griffin, for their help and guidance, and Ms. Bokani Mtengi for training me at Howard University. Lastly, I would like to thank Dr. R.D. Vispute from Blue Wave Semiconductors for his expertise on this project.

## References:

- [1] V.Kh. Liechtenstein, T.M. Ivkova, E.D. Olshanski, R. Repnow, J. Levin, R. Hellborg, P. Persson, T. Schenkel. "Advances in targetry with thin diamond-like carbon foils"; Nuclear Instruments and Methods in Physics Research A, 480 (2002) 185-190.
- [2] R.W. Shaw, D.P. Bontrager, L.L. Wilson, C.S. Feigerle, C.F. Luck, M.A. Plum. "An Electron Beam SNS Foil Test Stand"; White Paper.
- [3] T. Spickermann, M.J. Borden, R.J. Macek, R.W. Shaw, C.S. Feigerle, I. Sugai. "Comparison of carbon and corrugated diamond stripper foils under operational conditions at the Los Alamos PSR"; Nuclear Instruments and Methods in Physics Research A, 590 (2008) 25-31.
- [4] R.W. Shaw, V.A. Davis, R.N. Potter, L.L. Wilson, C.S. Feigerle, M.E. Peretich, C.J. Liaw. "Corrugated Thin Diamond Foils for SNS H-Injection Stripping"; White Paper.
- [5] R.A. Campos, V.J. Trava-Airoldi, O.R. Bagnato, J.R. Moro, E.J. Corat. "Development of nanocrystalline diamond windows for application in synchrotron beamlines"; Vacuum 89 (2013) 21-25.
- [6] RD Vispute, H.K. Ermer, P. Sinsky, A. Seiser, R.W. Shaw, G. Harris, F. Piazza. "Nanodiamond Foil Product for H- Stripping to Support Spallation Neutron Source (SNS) and Related Applications"; White Paper.



# Characterization and Modeling of Carrier Dynamics in Thin Films of Gallium Nitride

Rachel Lucas

Physics/Aerospace Engineering, Purdue University

**NNIN REU Site: UCSB Nanofabrication Facility, University of California, Santa Barbara, CA**

*NNIN REU Principal Investigator: Dr. James Speck, Materials Department, University of California, Santa Barbara*

*NNIN REU Mentor: Brian McSkimming, Materials Department, University of California, Santa Barbara  
(2007 NNIN Intern at UCSB and 2008 NNIN iREU Intern in Tsukuba, Japan)*

Contact: lucas27@purdue.edu, speck@mrl.ucsb.edu, mcskimming@gmail.com

## Introduction:

Gallium nitride (GaN) is used in violet laser diodes that are used to read Blu-ray disks, as well as in light emitting-diodes ranging in color from red to ultraviolet. GaN is also employed in various wireless infrastructure applications in the form of high-electron-mobility transistors (HEMTs). GaN can operate at higher powers and temperatures than many other semiconducting materials and this makes it an excellent material for use in cell phone base stations in order to improve the distance of signal transmittance. GaN transistors use less power to convert an equivalent amount of power with less energy loss than many other semiconducting materials and because of this it has the potential to improve energy retention.

An excellent way to quantify material quality is through mobility measurements. Electron scattering from impurities as well as dislocations decreases mobility. When growth conditions of the material are varied defects and thus mobility values change. By data fitting to specific equations a value for the defect concentration can be found. We created software to do this along with plotting of raw data and the mobilities due to six scattering mechanism [1].

## Methods:

Software was created to perform data fitting of carrier concentration and mobility data taken through variable temperature Hall measurements. Carrier concentration is the density of electrons in the material, while mobility is a measurement of how well these electrons move through the material while dealing with scattering events. These data values were fit to two equations, the charge balance and total mobility equations. These equations along with the variable definitions can be referenced in Figure 1. The charge balance equation is a balance confirming that the material is electrically neutral. The total mobility equation uses Matthiessen's rule in order to consolidate mobility equations for six scattering mechanisms into the overall total mobility. Each of the six component mobility equations is based off of an individual scattering mechanism, each one having a physical basis in the material.

The program began by accepting a data set and scanning in the raw data values. These values were then plotted. An example of this plot can be referenced in Figure 2. Carrier concentration increased with temperature, while mobility increased to a peak and then decreased. Mobility took this shape because as the temperature decreased from

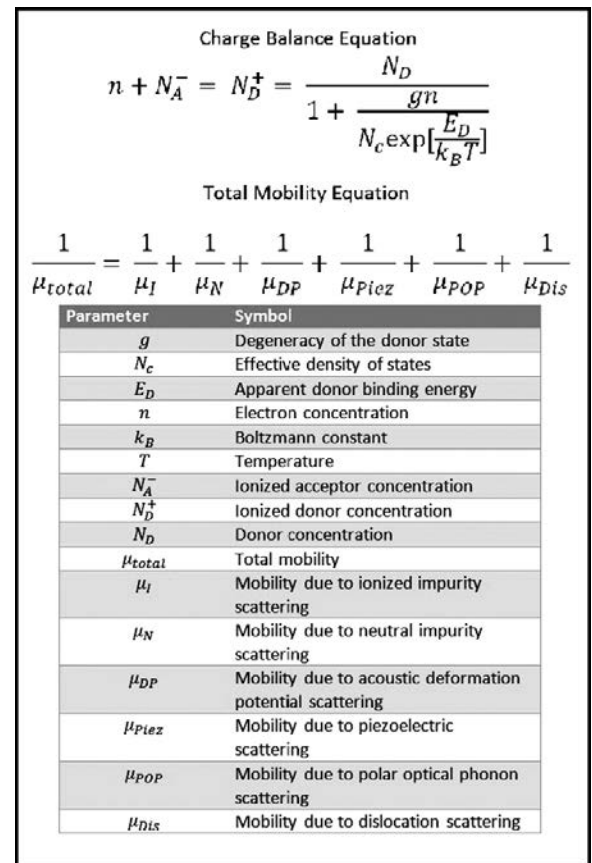


Figure 1: Charge balance and total mobility equations along with variable definitions [1].

M  
A  
T  
S

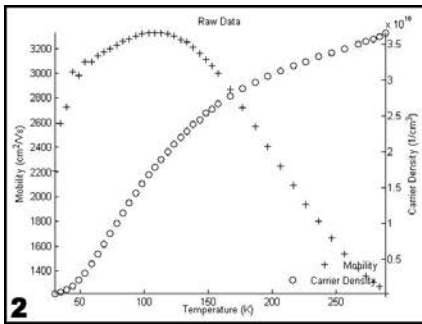


Figure 2: Raw data plot of carrier concentration and mobility data with varying temperature.

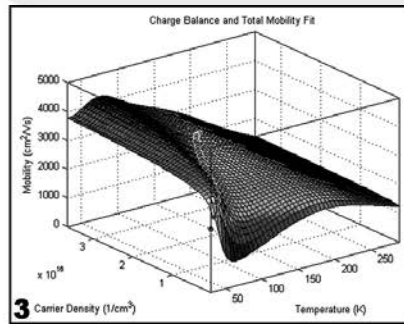


Figure 3: Fit of raw data to charge balance and total mobility equations as a surface. (See full color version on page xxxvi.)

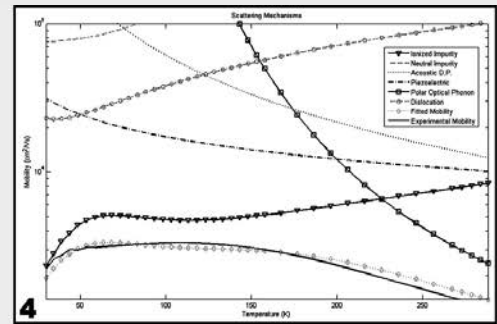


Figure 4: Mobilities due to each scattering mechanism along with total fitted and experimental mobility.

room temperature, phonons, vibrations in the lattice structure of GaN, began to lose energy and eventually freeze out. This decreased the scattering effect of polar optical phonon scattering, thus increasing the mobility. As the temperature continued to decrease, the mobility came to a peak and the effect of charge carriers themselves lost energy, and freezing out began to take over.

After the raw data values were scanned in and plotted they were fit to the charge balance and total mobility equations as a surface, which can be referenced in Figure 3. This allowed for the determination of four unknown parameter values: the acceptor concentration,  $N_A$ , which is the density of atoms in the sample that accept carriers, the donor concentration,  $N_D$ , which is the density of atoms in the material that donate carriers, the apparent donor binding energy,  $E_D$ , which is the energy required for an atom to donate a carrier, and the occupancy of traps along a dislocation,  $f$ , which is a value from 0 to 1 denoting how many traps along dislocations are occupied by a carrier. These four values can then be used in the six mobility equations for each of the scattering mechanisms as well as the total mobility equation in order to create a plot. This plot can be viewed in Figure 4.

In this plot, dominant scattering mechanisms for specific samples can be seen. Because scattering caused carriers to move more slowly, the scattering mechanism that caused the lowest mobility was the predominant scattering mechanism. In this particular sample, ionized impurity scattering was most influential up until approximately 225 K, while polar optical phonon scattering was dominant above this value.

## Results and Conclusions:

Determining values for  $N_A$ ,  $N_D$ ,  $E_D$ , and  $f$ , along with measured mobility values, allowed for a comparison between GaN samples grown with varied conditions.  $N_A$  corresponded to

approximate defect density and defect density had a direct effect on mobility and thus sample quality. As defect density increased scattering increased, therefore decreasing mobility. Materials allowing higher mobility allowed carriers to move more easily through them and thus were a better quality material.

## Future Work:

In the future, we are hoping to test the effect of different power levels of the plasma source on  $N_A$ . We are expecting to see an increase in  $N_A$  with an increase in power level as increasing the power level supplies the sample with more energy in order to create more ionized atoms and thus acceptors. We also want to test different flow rates of the plasma source and expect to see a similar correlation between it and  $N_A$ .

## Acknowledgements:

Thanks to Brian McSkimming and Dr. James Speck as well as to his research group. Thank you to the National Nanotechnology Infrastructure Network Research Experience for Undergraduates Program and the NSF for funding, and thanks to the UCSB Nanofabrication Facility. Thank you also to UCSB's multiple site coordinators.

## References:

- [1] Kyle, Erin C.H., Stephen W. Kaun, Peter G. Burke, Feng Wu, Yuh-Renn Wu, and James S. Speck. "High-electron-mobility GaN Grown on Free-standing GaN Templates by Ammonia-based Molecular Beam Epitaxy." *Journal of Applied Physics* 115.193702 (2014).



# Decreasing Contact Resistance to n-InGaAs with ALD TiN

Brian Markman

Materials Science and Engineering, The Pennsylvania State University

NNIN REU Site: UCSB Nanofabrication Facility, University of California, Santa Barbara, CA

NNIN REU Principal Investigator: Dr. Mark Rodwell, Electrical and Computer Engineering, University of California, Santa Barbara

NNIN REU Mentor: Prateek Choudhary, University of California, Santa Barbara

Contact: brian.markman8@gmail.com, mjwrodwell@gmail.com, prateek.pc@gmail.com

## Abstract:

The effects of multiple deposition parameters on the plasma enhanced atomic layer deposition (PEALD) of conductive titanium nitride (TiN) films were investigated. Specifically, effects of chamber pressure and plasma exposure time on TiN resistivity were characterized. Optimum growth conditions for minimum film resistivity was determined to be: substrate temperature of 300°C, plasma power of 500W, precursor gas of ammonia (NH<sub>3</sub>), chamber pressure of 2 mTorr, and a plasma time of 30 seconds. The minimum achieved resistivity was found to be 176 μΩ\*cm.

Precursor Gases	Flow Rate (sccm)	ICP Power (W)	Resistivity (μΩ*cm)
N <sub>2</sub> /H <sub>2</sub>	13/39	400	814
N <sub>2</sub> /H <sub>2</sub>	13/39	500	453
NH <sub>3</sub>	40	400	595
NH <sub>3</sub>	40	500	432

Table I: Resistivity relationship to plasma power for two different plasma compositions.

Precursor Gases	Flow Rates (sccm)	Resistivity (μΩ*cm)
N <sub>2</sub> /H <sub>2</sub>	13/39	453
N <sub>2</sub> /H <sub>2</sub>	31/21	508
N <sub>2</sub> /H <sub>2</sub>	4/48	534
NH <sub>3</sub>	40	340
NH <sub>3</sub> /N <sub>2</sub>	40/20	609

Table II: Resistivity relation to plasma composition for combinations of N<sub>2</sub>, H<sub>2</sub>, and NH<sub>3</sub>.

## Introduction:

Dimensional scaling of heterojunction bipolar transistors (HBT) must be supplemented by reductions in contact resistance at the emitter and base contacts, in order to improve device performance. Specifically, the emitter contact is particularly difficult to fabricate due to the extremely high aspect ratio and high current densities required. Due to these requirements, titanium nitride is of interest because of its low resistivity and high melting temperature [1, 2]. Many deposition techniques of TiN have been explored; atomic layer deposition (ALD) is of particular interest because of its conformal coating of high aspect ratio structures and low resistivity [1, 3].

Though multiple precursors are commonly used in ALD TiN deposition, tetrakis-dimethylamido titanium (TDMAT) is attractive due to its ability to deposit at temperatures below 400°C without generating chemically aggressive, non-volatile products [1, 4, 5]. Additionally, plasma assisted processes are common due to their ability to increase deposition rate and reduce resistivity [1]. This study presents a novel investigation of chamber pressure on TiN film resistivity for low contact resistance applications as well as a review of plasma power, plasma composition, plasma exposure time, and the introduction of a hold step.

## Experimental Procedure:

The ALD system used in all tests was an Oxford FlexAL remote plasma system. Substrates were prepared from doped silicon <100> wafers that were coated with an insulating layer. All samples were solvent cleaned and dehydrated before being loaded into the ALD. Sigma Aldrich 99.999% TDMAT was used. An inductively coupled plasma (ICP) system was used and operated at 500W and 13.56 MHz, unless otherwise mentioned. Substrate temperature was kept at 300°C and the TDMAT bubbler was kept at 60°C.

During tests, plasma parameters including plasma power, plasma composition, chamber pressure, and plasma exposure time were varied. Sheet resistance was then measured using a four-point probe. Film thicknesses were determined using SEM and ellipsometry.

## Results and Conclusions:

To achieve the lowest TiN resistivity, the effects of plasma power, plasma composition, chamber pressure, plasma exposure time, and hold step duration were investigated.

**Plasma Power.** As demonstrated in Table I, as plasma power is increased, the resistivity decreases independent of the precursor oxidant.

M  
A  
T  
S

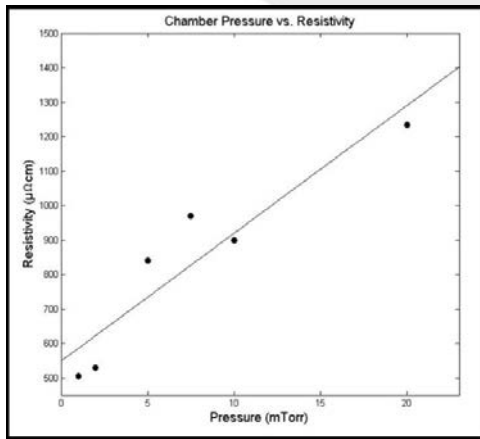


Figure 1: Resistivity as a function of chamber pressure for substrate temperature 300°C, plasma power 500W, and plasma exposure time 25 s.

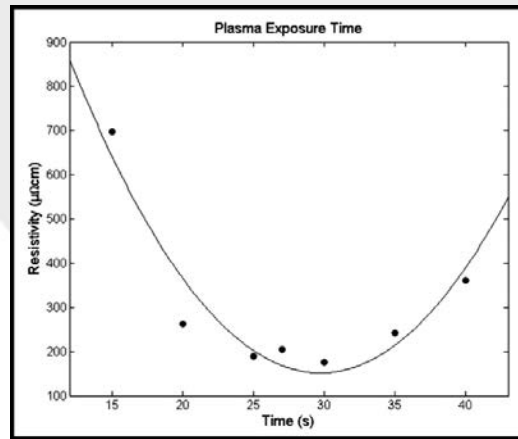


Figure 2: Resistivity as a function of plasma exposure time for substrate temperature 300°C, plasma power 500W, and chamber pressure 2 mTorr.

**Plasma Composition.** Both nitrogen rich and hydrogen rich plasma compositions were tested and the results are outlined in Table II. It was found that a stoichiometric ratio of N:H 1:3 is optimal for both  $\text{NH}_3$  and  $\text{N}_2/\text{H}_2$  precursors where  $\text{NH}_3$  is the most favorable. This is likely due to the formation of more  $\text{NH}_x$  radicals in a  $\text{NH}_3$  plasma than in an  $\text{N}_2/\text{H}_2$  plasma [1, 3].

**Chamber Pressure.** As illustrated in Figure 1, as chamber pressure decreases, resistivity decreases. This is likely because of reduced plasma damage over time.

**Plasma Time.** Increasing plasma time for  $t < 30$  seconds decreases the resistivity; however, when  $t > 30$  seconds, resistivity increases quickly. Figure 2 demonstrates this relationship and suggests that for  $t < 30$  seconds, the plasma is mostly reacting away the organic ligands contained within TDMAT. Likely after 30 seconds most of the ligands have been removed and subsequent plasma action results in plasma damage rather than defect removal.

**Dose and Hold.** The effect of introducing a hold step during the TDMAT dose was investigated. TDMAT was held in the chamber, allowing conformal coating of high aspect ratio structures. Further decomposition of the TDMAT also provided lower resistivity. A five second hold time was found to allow for the lowest resistivity, while an increased time realized no further improvements.

By increasing plasma power, using  $\text{NH}_3$  as an oxidant, decreasing chamber pressure, and increasing plasma time ( $t = 30$  seconds), it is possible to significantly reduce TiN film

resistivity and thus create less resistive metal contacts in many devices thus enabling next generation HBTs without having to alter the base contact as well.

#### Future Work:

Experimentally determined TiN has recently been incorporated into 64 nm HBTs, which are currently being processed. Transmission line models (TLM) will be fabricated to quantitatively determine the contact resistance associated with the newly developed TiN recipe. The effects of plasma power on contact resistance will be examined.

#### Acknowledgements:

I would like to thank Prateek, Rob, Chen-Ying, all other members of the Rodwell group, and all of the cleanroom staff for their help and support throughout the summer. Additional thanks to the NNIN REU Program, NSF, and DARPA for making this project possible.

#### References:

- [1] E. Gerritsen, et al., SSE, 49, (2005).
- [2] J. K. Huang, et al., Thin Solid Films, 519, (2011).
- [3] Y. Y. Chen, et al., Microelectronic Engineering, 112, (2013).
- [4] P. Caubet, et al., ECS, 155, (2008).
- [5] Atomic Layer Deposition, NNIN, UCSB.

# Using Fluid Dynamics Modeling to Guide the Fabrication of Patterned Shearing Blades for the Solution Deposition of Single-Crystalline Organic Semiconductor Thin Films

Geoffrey C. Martin-Noble  
Chemistry and Computer Science, Haverford College

**NNIN REU Site:** *Stanford Nanofabrication Facility, Stanford University, Stanford, CA*

*NNIN REU Principal Investigator: Professor Zhenan Bao, Chemical Engineering, Stanford University*

*NNIN REU Mentor: Leo Shaw, Chemical Engineering, Stanford University*

*Contact: gmngeoffrey@gmail.com, zbao@stanford.edu, leoshaw@stanford.edu*

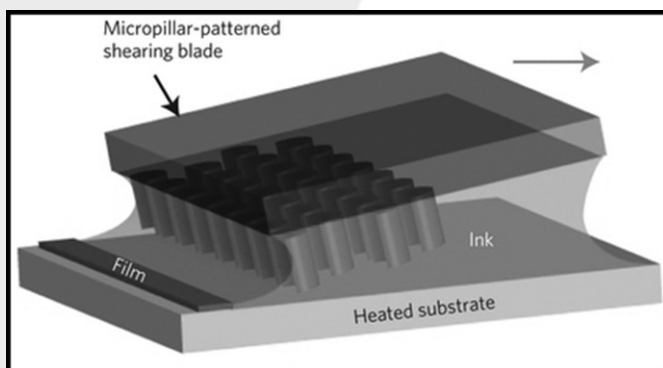


Figure 1: The solution shearing technique using a blade with micropillars (not to scale).

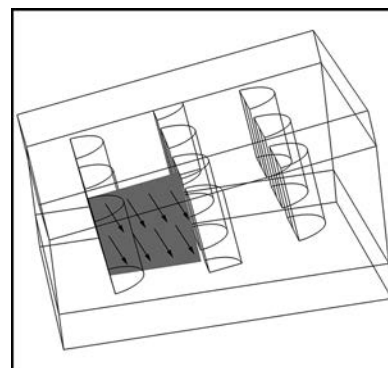


Figure 2: COMSOL model geometry. The trapezoid surface was used to measure mass flux and was not part of the model geometry.

## Abstract and Introduction:

Organic semiconductors (OSCs) are promising materials for applications requiring flexible and transparent electronics and have the potential to be produced using low-cost solution processing methods [1, 2]. However, typical solution-based techniques create polycrystalline OSC thin films unable to reach the performance of single crystals grown by vapor-based deposition methods [3].

Previously, the Bao group has developed a method called solution shearing for the deposition of high quality OSC thin films for use in field effect transistors [3]. In solution shearing, the OSC is dissolved in a solvent, and the solution is spread across a heated silicon substrate by a blade moving at a constant velocity, as shown in Figure 1. The solvent evaporates as it is sheared, depositing the OSC solute as a thin film.

Using this technique to shear a solution of 6,13-bis(triisopropylsilyl)ethynyl pentacene (TIPS-pentacene) in toluene resulted in thin films with field effect mobilities—the primary measure of semiconductor effectiveness—more than double the highest previously reported for TIPS-pentacene [4]. However, the films had large void spaces between crystalline ribbons. We suspected that these voids formed because as crystals grow on either side of a region, they pull solute from it, creating a zone with depleted OSC.

To eliminate these voids, micropillars were introduced to the blades [1] (see Figure 1) to induce recirculation in the solution during shearing. This modification virtually eliminated voids and resulted in mobilities double again those achieved without micropillars. Further improvement could likely be achieved by optimization of the micropillar pattern.

In order to better understand the shearing process, we used COMSOL Multiphysics to model the effects of different micropillar shapes and spacings on the solution flow during shearing. We fabricated these blades using photolithography with the aim of correlating simulated fluid flow with experimental blade performance, and thus enabling the use of modeling for future blade development.

## Procedure:

**Model Parameters.** Figure 2 shows the model geometry used in COMSOL. Only the solvent was modeled, as the concentration of OSC is low enough to not affect viscosity. Periodic boundary conditions were used on the sidewalls to model an infinite array of pillars. The mass flux flowing through the system was set to the experimentally determined solvent evaporation rate. To simplify the calculation, the

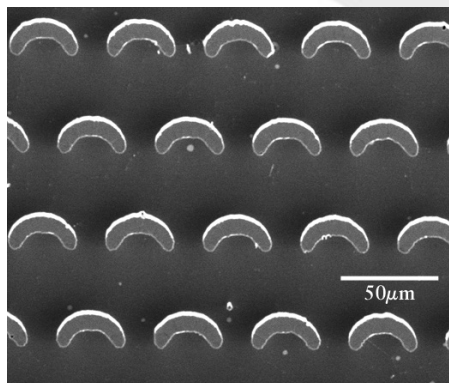


Figure 3: A scanning electron micrograph of part of a completed blade.

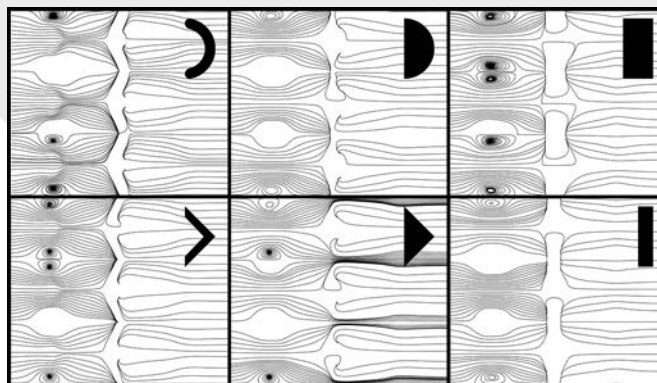


Figure 4: Velocity streamlines of simulated fluid flow. Line spacing indicates speed.

simulation was performed in the frame of reference with the blade stationary and the substrate moving to the left, but all data was adjusted back to the laboratory frame for analysis.

**Fabrication of Blades.** The blades were created using a standard photolithography procedure and deep reactive ion etching with sulfur hexafluoride ( $\text{SF}_6$ ) on a silicon substrate.

## Results and Discussion:

Figure 4 shows two-dimensional velocity streamlines of the simulated fluid flow for different pillar shapes. We also examined different pillar spacings (not shown). The flow is shown  $3 \mu\text{m}$  above the substrate. To try to quantitatively evaluate the different pillar shapes, we measured the simulated lateral mass flux between two rows of pillars through the surface shown in Figure 2. We hypothesized that an increased lateral flux would be an indication of improved recirculation and therefore improved crystals. Flux measurements were  $109 \text{ ng/s}$  for the model with crescent pillars,  $115 \text{ ng/s}$  for the chevron,  $115 \text{ ng/s}$  for the thick bar,  $119 \text{ ng/s}$  for the thin bar,  $123 \text{ ng/s}$  for the semicircle, and  $125 \text{ ng/s}$  for the triangle.

Previous experimental results indicate that the chevron and crescent pillars create noticeable improvements in the TIPS-pentacene thin film, while the semicircle and bar pillars do not. However, the crescent and chevron models actually have the lowest lateral mass flux, so measuring flux across the surfaces we used does not appear to be an effective metric for evaluating the simulations. Neither can we conclude the reverse trend—lower lateral flux improves film quality—because a lateral flux of zero would result from the removal of the micropillars, which were already shown to create a significant improvement.

## Summary and Future Work:

Solution shearing has already been demonstrated as an effective method for the creation of high-quality single-crystalline OSC

thin films and the addition of micropillars further improves the technique. However, we cannot use lateral flux as we have measured it in order to effectively evaluate simulation results, so we must identify another figure of merit.

To investigate this project further, we must evaluate the quality of TIPS-pentacene thin films sheared with different blades. We can examine the films optically, employ grazing incidence x-ray diffraction to calculate crystal coherence length, and measure the field-effect mobilities of the films. By correlating experimental and simulation results, we aim to find an effective metric for evaluating simulation results. With appropriate evaluation, the simulations can be used to determine optimal pillar patternings for a range of different systems.

## Acknowledgements:

I would like to acknowledge the National Nanotechnology Infrastructure Network Research Experience for Undergraduates Program, the National Science Foundation, and Stanford's Center for Integrated Systems for funding. I would also like to thank the Bao Group, the Stanford Nanofabrication Facility staff, the Stanford research computing staff, Mike Deal, Maureen Baran, and my other Stanford REU interns for their support.

## References:

- [1] Gao, P., et al. *Adv. Mater.* 21, 213-216 (2009).
- [2] Rogers, J. A., et al. *Proc. Natl. Acad. Sci. USA* 98, 4835-4840 (2001).
- [3] Diao, Y., et al. *Nat. Mater.* 12, 665-671 (2013).
- [4] Giri, G., et al. *Nature* 480, 504-508 (2011).

# Characterization of InAs/AlSb/GaSb Heterostructures When Exposed to *in situ* Plasma Cleans in an ALD Process

Marlee Motes

Chemical Engineering, University of Arkansas

NNIN REU Site: UCSB Nanofabrication Facility, University of California, Santa Barbara, CA

NNIN REU Principal Investigator: Dr. Christopher Palmström, Electrical and Computer Engineering,  
and Materials, University of California, Santa Barbara

NNIN REU Mentor: Borzoyeh Shojaei, Materials Science and Engineering, University of California, Santa Barbara

Contact: [mjmotes@email.uark.edu](mailto:mjmotes@email.uark.edu), [cpalmstrom@ece.ucsb.edu](mailto:cpalmstrom@ece.ucsb.edu), [borzoyeh@umail.ucsb.edu](mailto:borzoyeh@umail.ucsb.edu)

## Abstract:

The ability to control the carrier density in a semiconductor using a voltage applied to a metal gate electrode on top of a dielectric insulating layer is critical to many device applications. Gallium antimonide/indium arsenide/aluminum antimonide/gallium antimonide (GaSb/InAs/AlSb/GaSb) heterostructures have electronic properties that make them useful for electronic and optoelectronic application [1]. However, the gating efficiency has generally been low with hysteretic behavior. Surface contamination and surface oxides on the heterostructures are believed to be the cause of hysteric gate operation. The main goal of the project is to improve gate control of group III-V antimonide based semiconductor heterostructures. An *in situ* plasma clean using both hydrogen and nitrogen was used prior to depositing of a AlN dielectric film by atomic layer deposition (ALD). Images were taken using atomic force microscopy (AFM) before and after deposition to determine if degradation of the surface occurred, and if so, the rate of degradation; also to view the atomic layers that had been deposited. Optical and atomic force microscopy images were taken between fabrication steps, as well as after fabrication was completed. The electrical properties were also measured (mobility, resistivity, carrier density via four-point probe techniques and the Hall Effect) of the full heterostructures and lone insulating buffers before and after exposure to fabrication steps. These measurements help understand the effects of surface roughness, surface contamination, and processing induced defects on gate operation of the heterostructures.

## Introduction:

Compound semiconductors have applications in electronics and optoelectronics such as transistors, infrared detectors and infrared emitters. InAs is a compound semiconductor and GaSb/InAs/AlSb/GaSb heterostructures have electronic properties that make them useful for high speed, low power electronics and infra-red optoelectronic application [1]. However, their implementation in electronic devices has been limited because of difficulties in fabricating devices. Using InAs and AlSb layers, the InAs creates a channel where electrons become confined; this is called a quantum well. When processing the material to make these applications often a metal gate electrode must be fabricated onto the material that allows control of the electron density in the InAs channel by applying a voltage to the gate.

Contamination of the GaSb surface occurs very readily. It can begin to oxidize as soon as the surface is exposed to air after the growth process of the material is over [2]. It can also become contaminated when performing fabrication processes on the material. Therefore, a way to clean and protect the surface

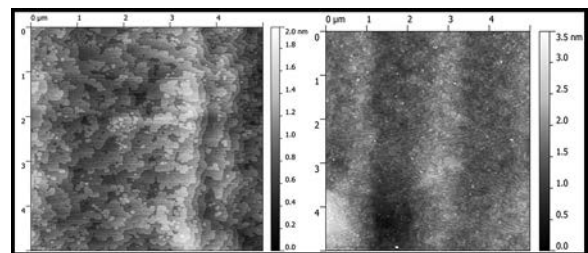


Figure 1: AFM images of the GaSb surface before and after basic photolithography process and compatible chemical clean.

without changing the material's performance is needed. The following atomic force microscopy images depict a surface immediately after growth on the right and on the left is the same sample after going through a standard photolithography process and solvent clean (see Figure 1).

## Experimental Procedures:

In this experiment, two samples were tested. The first being an InAs layer 5 nm from the surface and the second being an InAs layer 55 nm from the surface. The samples were first measured for Hall mobility, sheet resistivity, and sheet carrier density by Hall measurements using four-point contacts at the corners of the samples. The samples then underwent an ALD process where in a chamber the GaSb/InAs/AlSb/GaSb heterostructure was heated to 300°C and then cleaned with hydrogen plasma and then with nitrogen plasma for a combined 10 seconds under 50W of power. Then AlN was layered in a self-limiting manor. The exposure to the nitrogen and hydrogen plasmas were repeated 1, 10, and 100 times for different ALD runs, and electronic properties were determined by Hall measurements after the combined plasma cleans and ALD process.

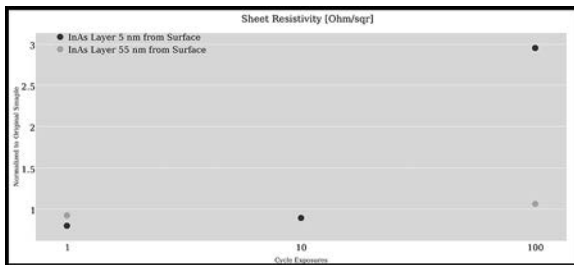


Figure 2: Plot of number of ALD cycles versus resistivity normalized to the original sample.

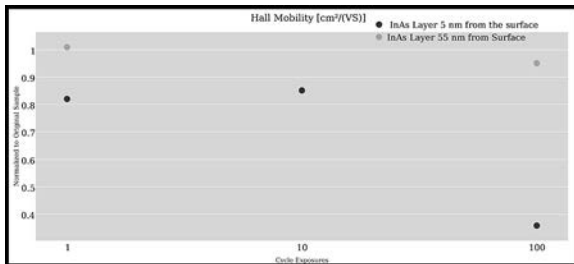


Figure 3: Plot of number of ALD cycles versus mobility normalized to the original sample.

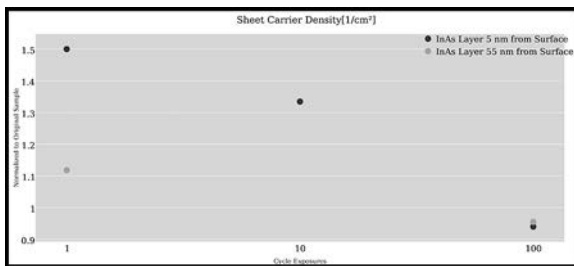


Figure 4: Plot of number of ALD cycles versus carrier density normalized to the original sample.

## Results and Conclusions:

It was desired that resistivity and mobility measurements (see Figure 2 and 3) stay as close as possible to the original sample to maintain the functionality of the material. Carrier density was expected to change due to removal of surface contamination changing the surface carrier density and bulk properties changing after many cycle exposures (see Figure 4).

AlN deposition including a hydrogen and nitrogen *in situ* plasma clean was thought to be a useful agent in the passivation of GaSb/InAs/AlSb/GaSb heterostructure.

This study has shown that the electrical properties of quantum wells set back at greater distances from the structure's surface are less affected by the cleaning process while the electronic properties of quantum wells close to the structures surface were sensitive to the cleaning process.

## Future Work:

This ALD process of AlN could be a possible precursor of other treatments of the GaSb surface to prevent impurities from forming on the surface during processing as well as preventing oxidation; it is desired to use the optimal amount of cycle exposures of AlN and then also test deposition of a dielectric on top of the AlN layers to possibly improve the gating process when testing the material.

## Acknowledgements:

I would like to thank Borzoyeh Shojaei, Dr. Chris Palmstrøm, and Wendy Isben for all of their help while at UCSB. I would also like to thank the NNIN staff, as well as the funding sources for this project: NNIN REU Program, NSF, and University of California at Santa Barbara.

## References:

- [1] Kroemer, Herbert. "The 6.1 A family (InAs, GaSb, AlSb) and its heterostructures: a selective review." Science Direct Physica 20 (2004): 196-203. Print.
- [2] Ruppalt, Laura B., Erin R. Cleveland, James G. Champlain, Sharka M. Prokes, J. Brad Boos, Doewon Park, and Brian R. Bennett. "Atomic layer deposition of Al<sub>2</sub>O<sub>3</sub> on GaSb using *in situ* hydrogen plasma exposure." Applied Physics Letters 101.23 (2012): 231601. Print.



# Cohesion and Adhesion in Thin-Film Organic Nanostructured Materials for Photovoltaic Applications

G. Emily Nitzberg

Mechanical Engineering and Computer Science, University of Portland

NNIN REU Site: Stanford Nanofabrication Facility, Stanford University, Stanford, CA

NNIN REU Principal Investigator: Reinhold Dauskardt, Materials Science and Engineering, Stanford University

NNIN REU Mentor: Christopher Bruner, Chemistry, Stanford University

Contact: nitzberg16@up.edu, rhd@stanford.edu, cbruner9@stanford.edu

## Abstract:

The main focus of this project was to study the nano-mechanical properties, cohesion, and reliability of advanced thin-film architectures used in polymer organic photovoltaics. Photovoltaics are devices that convert incident light into usable energy. The cohesion of the photoactive layer, which consists of the semiconducting polymer poly(3-hexylthiophene-2, 5diyl) (P3HT) and small molecule Phenyl-C60-butyric acid methyl ester, or PC<sub>60</sub>BM, are characterized using micromechanical analysis. The goal of the work was to develop an understanding of how the films adhesive/cohesive and thermo-mechanical properties are related to their nanostructure and processing conditions. In addition, we used a cross-linking agent (BABP) to minimize molecular diffusion, improving thermal stability. In particular, we were interested in how the films were affected under operating conditions; including exposure to air, solar UV irradiation, and temperature. By correlating the results to the efficiencies for our organic photovoltaics and analyzing the trends, we intend to design processing methods that will improve the mechanical reliability of these devices while maximizing thermal stability.

## Introduction:

Having a finite amount of fossil fuels is one of the main reasons the development of alternative sources of energy is necessary. Additionally, the burning of said fossil fuels in such large quantities causes severe environmental alterations such as global warming. The project at hand aimed to offer a reliable alternative for fossil fuels with the use of photovoltaics.

Organic cells can be printed into very thin sheets making them weigh significantly less than inorganic based solar cells and allow for flexibility. However, organics tend to be more sensitive to air and moisture, meaning that environmental effects can severely degrade their performance. Our research also indicates that the polymers with small molecules used are relatively fragile from a mechanical perspective. This is important to note since barrier delamination of the solar cell may lead to catastrophic failure within the device. Our main concern for this project was the need for the cells to operate under severe environmental conditions.

The operational principle of an organic cell begins when light is incident upon the device, which is then followed by the absorption of the photon. This process then results in electrons

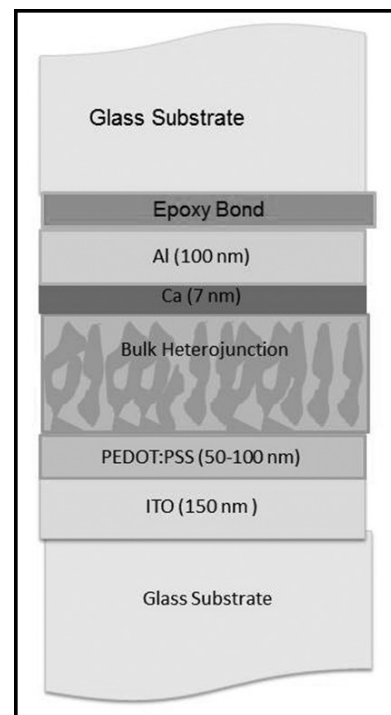


Figure 1: Organic solar cell thin film layer profile.

being excited from the highest occupied molecular orbital to the lowest unoccupied molecular orbital. Charge splitting then occurs allowing for the collection of electrons and holes.

## Experimental Procedure and Results:

The organic solar cells at hand consisted of eight layers as shown in Figure 1. The core of the cell was the bulk heterojunction (BHJ) layer, which consisted of a 1:1 weight ratio of P3HT and PC<sub>60</sub>BM and a particular amount of BABP ranging from 0%-10%.

First, a thin layer of BHJ solution was spin-coated onto a glass substrate and observed under a microscope after various thermal annealing times. As shown in Figure 2, BABP prevented the crystallization of PC<sub>60</sub>BM with annealing time. This is important to note since it is consistent with past

literature and supports the argument that BABP allows for thermal stability of the BHJ layer via preventing the diffusion of PC<sub>60</sub>BM molecules.

Next, one of the most important techniques used to test the mechanical properties of the solar cell devices was the four-point bend test (4PB). The 4PB test applies an equivalent amount of force on four parallel directions on the device, two forces acting on top of the device and two on the bottom of the device, in order to propagate a crack within the cell. This technique provided a method for analyzing the cohesion values of the devices. These values are significant because if the cohesion is low failure is more likely to occur. As shown in Figure 3, the cohesion values of the devices decreased significantly when BABP was included in the BHJ layer. These results helped us understand that although BABP increased the thermal stability of the cell, it decreased the mechanical reliability by about 50%. Though the cohesion values decreased significantly, they still remained around 5 J/m<sup>2</sup>, which is the optimal value desired for the devices.

Finally, after analyzing the cohesive strength of the device, it was important to investigate where exactly the failure occurred. In order to do so, an x-ray photoelectron spectrometer (XPS) was used.

XPS emits an x-ray beam onto the surface of the device and utilizes the photoelectron effect to eject core shell electrons from the elements on the surface. The XPS then records peaks at specific binding energies that correspond to each element on the periodic table.

In this case, the two peaks that occurred around 200 eV corresponded to sulfur and the large peak around 300eV corresponded to carbon. XPS analysis showed that failure occurred in the (organic) BHJ layer. This was due to the prominent peaks for sulfur and carbon within the analyzed spectra (see Figure 4).

The presence of sulfur and carbon indicated failure at the BHJ since those were the two common elements of P3HT and PC<sub>60</sub>BM. Also, the failure occurring at the BHJ did not change with BABP concentration and/or anneal time, which reinforced the conclusions made.

### Conclusions:

Although organic solar cell devices have many improvements to be made, this project was able to yield a few key conclusions. First, BABP increases the thermal stability yet decreases the cohesion values of the solar cells. Next, failure occurs at the BHJ layer no matter the concentration of BABP in the device, or the anneal time it undergoes. This allows for further analysis to be done on the BHJ in order to maximize its mechanical strength. Finally, devices are able to withstand 5-11.9 J/m<sup>2</sup>, which are optimal values for these kinds of organic devices.

### Acknowledgements:

Thank you to Professor Dauskardt, Christopher Bruner, and the 2014 Stanford NNIN REU group and staff. Also to the NNIN REU Program and National Science Foundation (NSF) for funding.

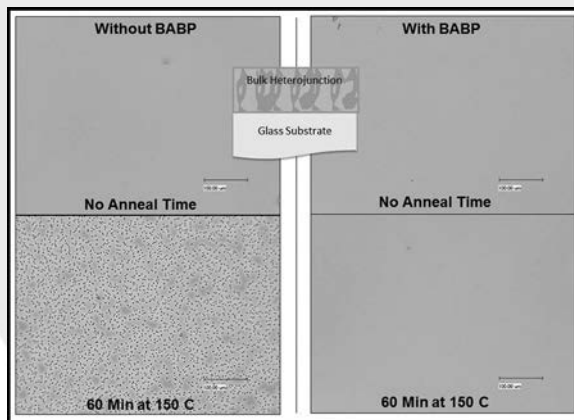


Figure 2: Microscopic images of BHJ layer on glass.

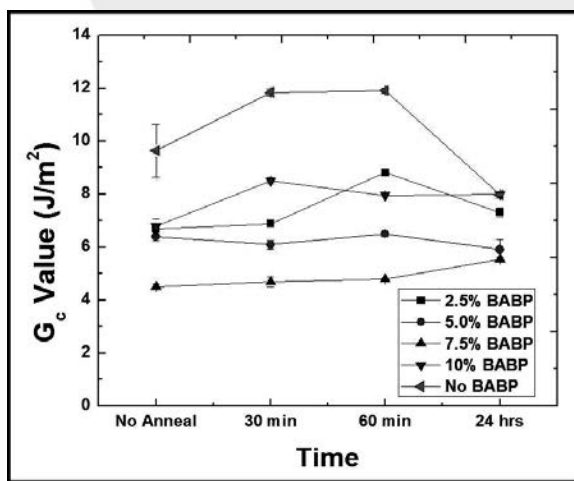


Figure 3: Cohesion values for devices with various BABP concentrations.

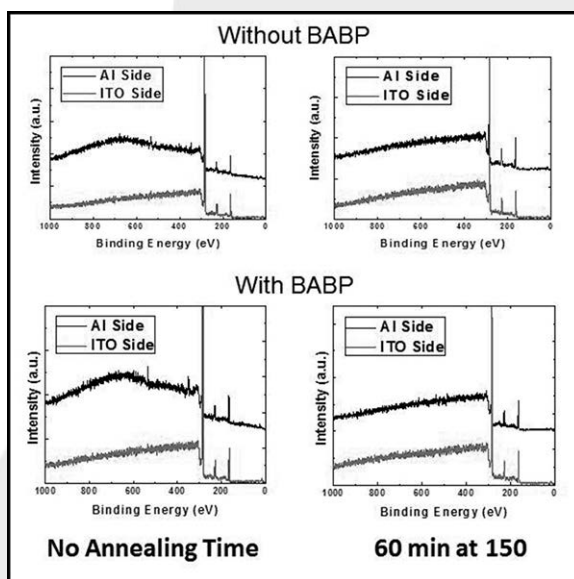


Figure 4: XPS results showed peaks at the sulfur and carbon binding energies.

M  
A  
T  
S

# Patterning Silicon Nanowire Arrays using EBL

Matthew Salmon

Chemical Engineering, North Carolina State University

NNIN REU Site: Institute for Electronics & Nanotechnology, Georgia Institute of Technology, Atlanta, GA

NNIN REU Principal Investigator: Prof. Michael Filler, Chemical and Biomolecular Engineering, Georgia Institute of Technology

NNIN REU Mentor: Ho Yee Hui, Chemical and Biomolecular Engineering, Georgia Institute of Technology

Contact: mcsalmon@ncsu.edu, michael.filler@chbe.gatech.edu, hhui3@gatech.edu

## Abstract:

Silicon nanowires have applications as advanced solar energy collectors, lithium ion anodes, catalysts and biological and chemical sensors. Silicon nanowires have demonstrated superior light absorbance in photovoltaic cells. The peak wavelength of light absorbed is tunable, depending on length, doping, spacing and diameter. Length and doping control in silicon nanowires are fairly well understood. The focus of this project was to develop a method for finely controlling diameter and spacing of silicon nanowires in an array and to transfer technology from ultra-high vacuum (UHV) to more scalable systems. Electron-beam lithography (EBL) was chosen because it can pattern samples with the nanometer resolution required. Using poly (methyl methacrylate) (PMMA) as the electron-beam resist, and electron-beam evaporation to deposit gold, an array of gold catalyst nanodots was developed on the silicon substrate surface. Then silicon nanowires were grown from each gold catalyst dot through vapor-liquid-solid deposition — in which silane decomposes on the catalyst surface, creating a liquid gold silicon eutectic, and a silicon crystal grows epitaxially on the bottom of the eutectic droplet. The goal was to create arrays of nanowires with diameters as small as 20 nm.

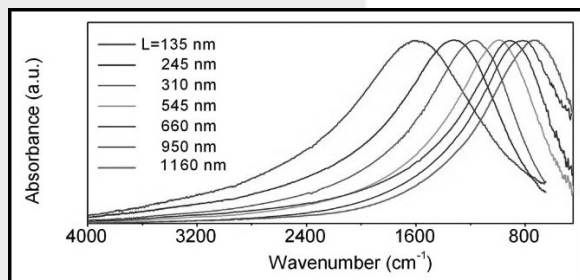


Figure 1: Surface plasmon resonance frequency varies with nanowire dimensions and spacing. (See full color version on page xxxvi.)

## Introduction:

Semiconductor nanowires, also called nanopillars, are of increasing interest in scientific research. Their synthesis methods and chemical, mechanical, electronic and photonic properties have been studied. They may have use as solar cell enhancers [1]. Our research team designed silicon (Si) nanowire synthesis methods with the electronic properties in mind. Surface plasmon resonance frequency varies with nanowire dimensions and spacing (Figure 1) [2], so dimension and spacing control is critical to nanowire function.

## Experimental Procedure:

A set of samples were made by cutting approximately 1 cm<sup>2</sup> from <111> Si wafers, which are necessary — as opposed to <100> Si — to produce vertical nanowires by the vapor liquid solid growth method [3]. The cut samples were then immersed in 10% hydrofluoric acid (49% HF diluted 1:4 in distilled water) for three minutes to remove silicon oxide (SiO<sub>2</sub>), rinsed in distilled water and dried with nitrogen. They were immediately placed in an electron-beam evaporator, pumped down to 8 × 10<sup>-7</sup> Torr and coated with 3.0 nm of gold (Au). Au-coated samples may have been stored, in clamshell sample holders in a cool dark space in the cleanroom, for as long as a week.

To grow nanowires, the reactor chamber was first vented. The reactor employed was a “CVD FirstNano Graphene Furnace” with quartz chamber, graphite susceptor, RF heating up to 2200°C, turbo pump for base pressure of 6.0 × 10<sup>-7</sup> Torr, and fed by argon, hydrogen (H), silane and methane gas lines. An Au-coated sample was immersed in 10% HF for 15s to remove any SiO<sub>2</sub> that may have formed on unprotected surfaces, rinsed in distilled water and dried with nitrogen.

Immediately, the sample was placed onto the reactor susceptor and the reactor was pumped down to a base pressure below 10<sup>-5</sup> Torr. The pressure was set to 7.0 Torr with only H flowing

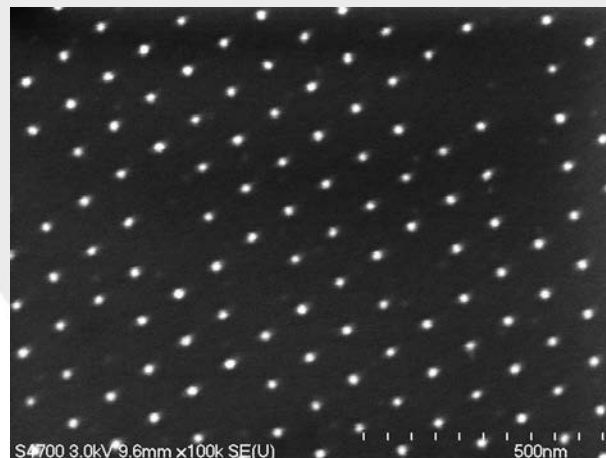
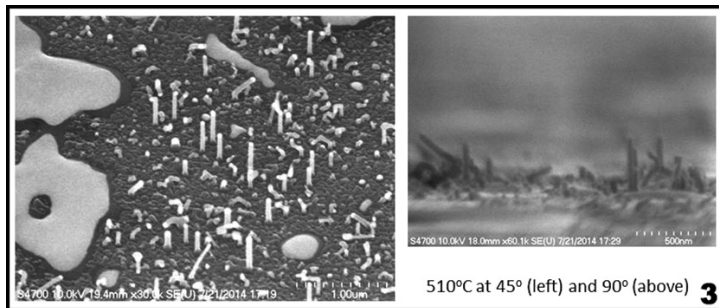
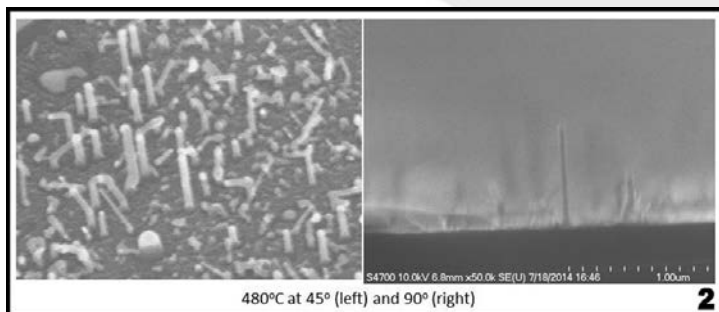


Figure 4: EBL patterning.

Figures 2, above, and 3, below: An inverse relationship was found between temperature and both nanowire kinking fraction and diameter and spacing.

at 500 standard cubic centimeters per minute (sccm). The temperature was then ramped up to 400°C over five minutes and finally, to the temperature setpoint over three minutes. After the temperature setpoint was reached, silane was flowed at 25 sccm for ten minutes and the H flow was reduced to 475 sccm to maintain a constant total flow rate. This was regarded as 350 mTorr of silane pressure for comparison to experimental results from other systems. The system was then vented and the sample removed.

The sample was then fractured for imaging by pressing with a scribe at the edge. The larger fragment of the two was placed on the 45° sample mount and the smaller fragment was placed on the 90° mount so that the fractured edge could be viewed by scanning electron microscopy (SEM).

### Results, Conclusions, and Future Work:

At the tested silane pressure, an inverse relationship was found between temperature and both nanowire kinking fraction and diameter and spacing (Figures 2 and 3). There was a direct relationship between temperature and wire size uniformity at this silane pressure. Variability in the reactor controls made it difficult to draw strong correlations between temperature and nanowire morphology. More data needs to be collected, after the reactor is fixed, at higher temperatures and different silane pressures to thoroughly understand how process conditions affect nanowire morphology. Once growth conditions are optimized, EBL patterning methods can be applied to achieve

an ordered array, or more complex pattern, of nanowires by seeding the gold, or other metal, catalyst exactly where it should go (Figure 4).

### Acknowledgements:

I would like to recognize my principal investigator Prof. Michael Filler and my mentor Ho Yee Hui. Dmitriy Boyuk and especially Saujan Sivaram, PhD, of the Filler group, were also a great help to me understanding our area of research and how to conduct it. Devin Brown was essential for the EBL part of the project and he did a really fantastic job patiently training Ho Yee and me on this complex tool. A number of the Georgia Tech IEN laboratory staff went the extra mile for me and were most helpful: Dean Sutter, Gary Spinner, John Pham, Thomas Averette, Scott Fowler, Claude Roney, Todd Walters, Eric Woods and Charlie Turgeon. Finally, I would thank the National Nanotechnology Infrastructure Network Research Experience for Undergraduates (NNIN REU) Program and National Science Foundation (NSF) for funding this work.

### References:

- [1] Peng K, et al.; Small, 1, No. 11, 1062-1067 (2005).
- [2] Chou L-W, Shin N, Sivaram S, Filler M; Journal of the American Chemical Society, 134, 16155-16158 (2012).
- [3] Picraux S T, Dayeh S A, Manandahar P, Perea D E, and Choi S G; JOM, vol. 62, No. 4, 35-43 (2010).



# Mechanical Properties of Hierarchical Nanoporous Metal

Aki Sato

Applied Optics, Chitose Institute of Science and Technology, Japan

NNIN iREG Site: Institute for Electronics & Nanotechnology, Georgia Institute of Technology, Atlanta, GA

NNIN iREG Principal Investigator and Mentor: Antonia Antoniou, Manufacturing Engineering, Georgia Institute of Technology

Contact: m2140050@photon.chitose.ac.jp, antonia.antoniou@me.gatech.edu

## Abstract:

There is a lot of research focused on the fabrication of hierarchical nanoporous structures applicable to new devices. Also, polymer has attracted attention in the application of materials. Previous reports in the literature describe the synthesis protocols of nanoporous gold (NPG) obtained by dealloying Au/Ag foil with  $\text{HNO}_3$ , and nanoporous copper fabricated by Cu/Si foam dealloying using HF [1]. Furthermore, it is well known that self-organized wrinkle structures are deformable anisotropic microstructures. Those wrinkle structures can be obtained by taking advantage of the difference in Young's modulus between soft and hard materials [2]. In this report, we show the preparation and measurement surface properties of a heterostructures obtained by combining metal foam and polymer. The basic surface properties of the samples will be discussed.

## Introduction:

The properties of metals and polymers are quite distinct. In this project, we focused on creating heterostructures by combining polymer and metal foam structures so as to establish a new system with applications as a sensor or actuator. Metal foams can span several length scales. In this system, the porosity is in the nanometer range that offers high surface to volume ratio and allows synthesis of porous metals with unique physical properties. This structure can be obtained via a two-step process involving synthesis of a metal alloy and its controlled corrosion (dealloying) in a solution. During dealloying one element of the alloy dissolves and the remnants self-assemble into a three dimensional sponge. The elastomer used in this project is polydimethylsiloxane (PDMS). This polymer is a soft material and any curling is easy to control via Young's modulus.

One inspiration for the project involves biomimetics that is observing and replicating functional biological surfaces and replicating their functional surfaces so as to obtain superior functional materials. For example, one of the most famous biological functions is the Lotus effect. Lotus leaf surfaces have hierarchical structures ranging from nanometer to micrometer. In previous research, we fabricated a structure that mimicked shark skin by using self-organization with a sample surface made of polymer. But shark skin surface is known to have a functional drag reduction because of its riblet structure. Our intention is to fabricate the same surface with a more durable material like metal.

Periodic buckling structures, similar to the shark skin riblet, are formed by self-organization. This "wrinkle" structure formation depends on the difference in any two material's Young's modulus. Also, the period of wrinkles depends on the hard material's height —  $\Lambda \propto 2\pi h(Ef/3Es)^{1/3}$  — where  $\Lambda$  is the period of wrinkle,  $h$  is the thickness of hard layer,  $Ef$  equals

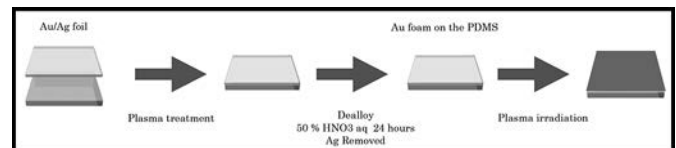


Figure 1: Gold foam on polymer process.

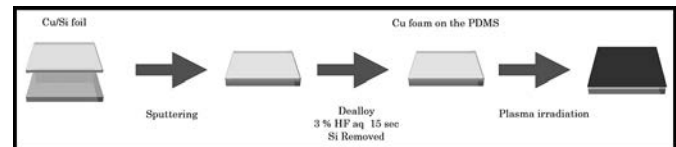


Figure 2: Copper foam on polymer process.

the hard layer's Young's modulus, and  $E_s$  is the hard layer's Young's modulus.

## Experimental Procedure:

We fabricated two types of metal samples.

**Gold Foam on Polymer (see Figure 1).** First, we cured PDMS at  $70^\circ\text{C}$  for five hours. This PDMS has a Young's modulus of 1.3 MPa. We treated the PDMS surface with a plasma irradiation for 10 min, and then fixed gold (Au) and silver (Ag) complex foil (gold leaf) on top of the PDMS. NP Au foil was formed by dealloying a Au/Ag foil by using a 50% nitric acid water solution for 4, 12, and 24 hours. As a result, we obtained nanoporous gold (NPG) and polymer heterostructures. Finally, we tried using plasma irradiation to change the surface chemistry.

**Copper Foam on the Polymer (see Figure 2).** In the meantime, we fabricated the same structure using a different

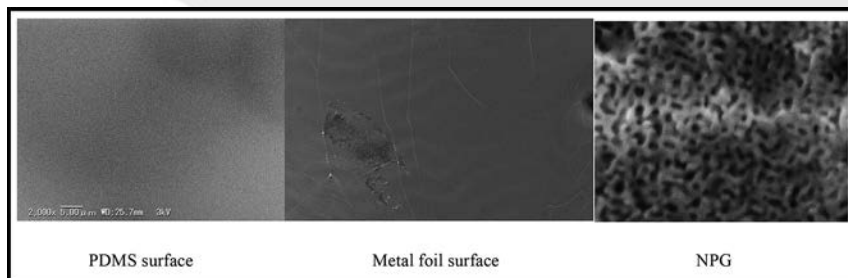


Figure 3: SEM images of surface observations.

Water contact angle	PDMS	Self standing Foil	NPG	
			48 Hours	4 Hours
No plasma 	 103.4	$\theta < 40^\circ$	 98	 92.4
Metal : Hydrophobic Polymer : Hydrophilic	Plasma 10 min 	N/A	Gradually Changed	
N = 3 Average	Plasma 30 min 	N/A	 113	 98.6

Table 1: NPG contact angles.

metal. We again cured the PDMS using the same curing condition of 2-1. After that, the PDMS surface was treated by plasma irradiation for 10 min. We then obtained copper (Cu) and silicon (Si) complex layers by sputtering, and dealloyed a Cu/Si foil using 3% HF water solution for 15 sec. After that, we obtained a nanoporous Cu and polymer heterostructure. Finally, we tried using plasma irradiation for 30 min to change the surface chemistry.

## Results and Discussion:

**Dealloying.** Dealloying NPG for 24 hours resulted in a nanoporous structure with a pore diameter around 20 nm. According to the results of a XPS survey, NPG dealloyed by  $\text{NH}_3\text{OH}$  for 24 hours had a surface that was less than 1% Ag. However after dealloying for only four hours, the sample had 6% Ag. We concluded that this porous diameter and the Au/Ag ratio depends on dealloying time. (See Figure 3.)

**Wettability.** A lot of biomimetic research focuses on surface wettability. In this report we show NPG contact angle measurement data in Table 1. In general, the polymer surface showed a hydrophilic surface and the metal showed a hydrophobic surface. With no plasma treatment, the polymer surface had hydrophobicity. In contrast, after plasma irradiation, the polymer surface was hydrophilic. On the other hand, our metal form results were the reverse. Also, 24 hours of dealloying the metal foam surface showed that the contact angle was more increased than a four-hour dealloying. Surface wettability depends on surface pore diameter and chemical

metamorphic. We concluded that we could successfully make a hydrophilic metal porous surface.

## Conclusions and Future Plans:

We obtained gold foam on PDMS, and we could see the difference in contact angles with this heterostructured surface. Also, we successfully obtained a nanoporous metal structure important for biomimetics. For future work, this structure has to make a clear buckling structure proven using the buckling equation, so we will need to change the thickness of the metal foam in order to obtain the periodic wrinkle structure. We can then consider sliding angle and reduction measurements. Such measurements can establish the combined properties of a complex heterostructure.

## Acknowledgements:

Many thanks to Prof. Antonia Antoniou, the National Nanotechnology Infrastructure Network International Research Experience for Undergraduates (NNIN iREU) Program, and the National Institute for Materials Science (NIMS).

## References:

- [1] Applied Physics Letters, 103, 241907 (2013).
- [2] T. Ohzono and M. Shimomura, Phys. Rev. B, 2004, 69(13), 132202-132206.

# Nanoparticle Photoresists: Synthesis and Characterization of Next-Generation Patterning Materials

Pavel Shapturenka

Chemical Engineering, City College of New York (CUNY)

**NNIN REU Site:** Cornell NanoScale Science & Technology Facility, Cornell University, Ithaca, NY

**NNIN REU Principal Investigator:** Christopher K. Ober, Materials Science and Engineering Department, Cornell University

**NNIN REU Mentor:** Jing Jiang, Materials Science and Engineering Department, Cornell University

**Contact:** pshaptu00@citymail.cuny.edu, cko3@cornell.edu, jj453@cornell.edu

## Abstract:

Hybrid metal oxide nanoparticle photoresists are prominent candidates for next-generation photolithography due to their exceptional sensitivity to extreme ultraviolet (EUV) radiation. To improve the resist's resolution, roughness, and sensitivity (RLS) performance, we explored new compositions for this nanoparticle system. In this study, a series of new nanoparticle resist compositions were synthesized and characterized by solubility and radiation dose tests, as well as deep ultraviolet (DUV) and electron-beam patterning.

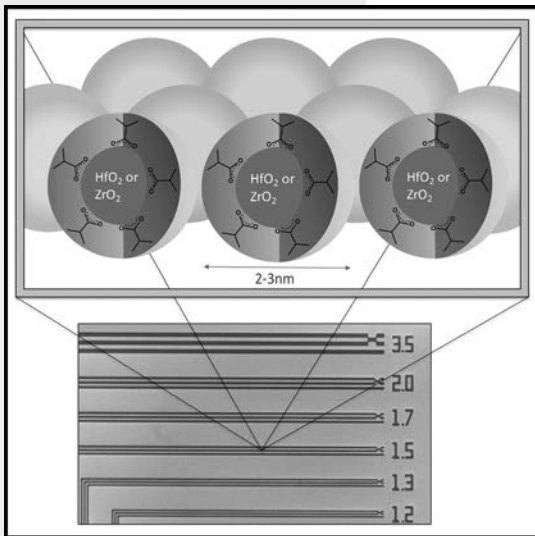


Figure 1: A schematic of the Ober group nanoparticle photoresist.

## Introduction:

If the current microelectronics industry is to continue the trend set by Moore's Law, immediate solutions are required for successful next-generation patterning processes. The processes currently in development use EUV radiation at a 13.5-nanometer wavelength. However, the source for this radiation is currently too weak for industrial production throughput. The nanoparticle photoresist developed by Ober and Giannelis, et al. (Figure 1) is one prominent candidate for next-generation photolithography, helping to mitigate the light source issues with its high EUV sensitivity [1]. The inorganic metal oxide core also provides thermal stability and a higher

refractive index, increasing the depth of field, while the organic ligand shell defines the nanoparticle's solubility properties. It is believed that the resists' EUV sensitivity relates to the relative binding affinities of the ligand shells; however, this requires further investigation. These properties provide a unique foundation for a patterning material that can be further explored for optimal performance.

## Experimental Procedure:

The nanoparticle resist was synthesized by a zirconia precursor and a carboxylic acid. The reaction workup through precipitation, resuspension, and drying yielded a nanoparticle powder. The particles were run through thermogravimetric analysis (TA Instruments) and dynamic light scattering (Zetasizer) to measure organic content and the particle size distribution.

For patterning characterization, a 10 wt% solution of particles with respect to PGMEA, with an 3 wt% addition of photoacid generator (N-hydroxy-5-norbornene-2,3-dicarboximide perfluoro-1-butanesulfonate), was prepared and spun onto a silicon wafer at 2000 RPM for 60 seconds. After a 60-second post-apply bake at 110°C, the resist was exposed with 248 or 254 nm UV light on the ASML 300C or ABM contact aligner, respectively. The JEOL 9500 e-beam lithography system was used for higher-resolution exposures.

Developing conditions were found by submerging resist samples in various developing solvents at measured durations. Solvents most commonly tried were o-xylene and 4-methyl-2-pentanol. Several developer mixtures were also attempted to more finely control developer kinetics. The ABM contact aligner was used to flood-expose adjacent regions of the wafer to test a series of doses and overall resist sensitivity. A Tencor P10 profilometer was used for film thickness measurements.

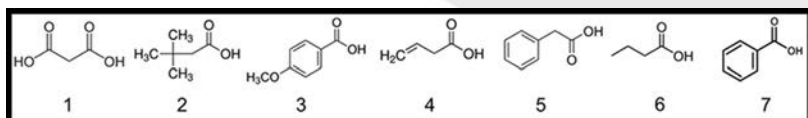


Figure 2: The attempted functional ligands for new compositions, corresponding to the numbering in Figure 3.

	Ligand	pKa	NP size (nm)	Organic content	Patterns?	Developing solvent	Optimal developing time
1	Malonic acid	2.82 5.7	--	--	No	--	--
2	3,3-Dimethylbutyric acid	4.79	4.5	47%	Yes	4-methyl-2-pentanol	30-50 s
3	4-Methoxybenzoic acid	4.47	4.0	60-65%	Yes	5:2 <i>o</i> -xylene:butyl acetate	45 s
4	3-Butenoic acid	4.34	--	--	No	--	--
5	Phenylacetic acid	4.31	6.7	59%	Yes	5:1 <i>o</i> -xylene:heptane	3-5 s
6	Butyric acid	4.82	--	55%	No	--	--
7	Benzoic acid	4.2	--	~60%	Yes	<i>o</i> -xylene	3-5 s

Figure 3: Results of new composition synthesis and developing conditions for each.

## Results and Conclusions:

Out of the six studied compositions (compounds 1-6 in Figure 2), two synthesis products agglomerated, and one yielded insoluble particles. The three remaining syntheses were successful; two of which yielded large enough quantities to be studied in greater detail. The two successful ligands were 4-methoxybenzoic acid and phenylacetic acid.

By TGA analysis, it was found that both nanoparticle powders were 60% organic by content, and were approximately 4 to 7 nanometers in diameter. The photoresists patterned effectively under deep ultraviolet light, nearly reaching the 150-nm resolution. Electron beam exposures of 4-methoxybenzoic acid resist showed clear 100-nm features and under-developed features at 50 nm. Phenylacetic acid exposures showed clearly defined features at 80 nm, with visible 35-nm features. In order to maximize resist performance, the developing conditions need to be optimized further.

## Future Work:

Having established two new patternable compositions and tailored the processing of each, further characterization is necessary for a better assessment of resist performance and optimization. Since our primary goal is to develop resists for

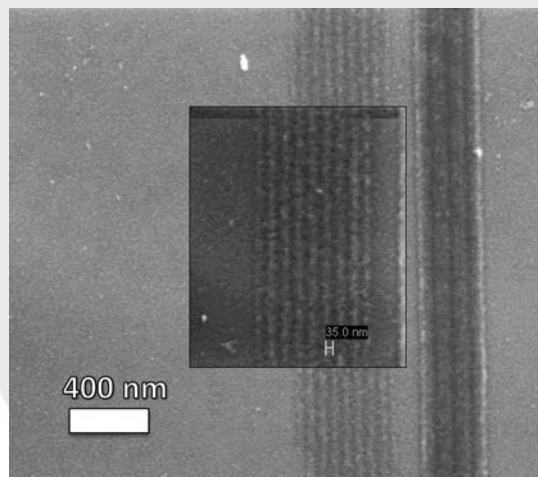


Figure 4: Electron-beam lithography result for the ZrO<sub>2</sub>-phenylacetic acid resist.

EUV patterning, we will study EUV exposures and compare the sensitivity with previous formulations.

We will also characterize the critical dimensions of the patterns, namely the line edge roughness and line width roughness (LER/LWR) through SuMMIT, and performing etch resistance tests for applications involving advanced process integration.

## Acknowledgements:

I would like to acknowledge the National Science Foundation, the National Nanotechnology Infrastructure Network Research Experience for Undergraduates (NNIN REU) Program, and the Cornell NanoScale Science and Technology Facility for their support. A special thanks to the Ober group, my mentor Jing Jiang, Ben Zhang, Melanie-Claire Mallison, and the rest of the CNF staff for their guidance.

## References:

- [1] Chakrabarty, S., Sarma, C., Li, L., Giannelis, E. P., and Ober, C. K. (2014). Increasing sensitivity of oxide nanoparticle photoresists (Vol. 9048, p. 90481C-90481C-5). doi:10.1117/12.2046555.

# The Optimization of High Growth Rate GaN Thin Film Mobility

Bethany Smith

Materials Science and Engineering, Arizona State University

**NNIN REU Site:** UCSB Nanofabrication Facility, University of California, Santa Barbara, CA

NNIN REU Principal Investigator: Professor James Speck, Materials Department, University of California, Santa Barbara

NNIN REU Mentor: Brian McSkimming, Materials Department, University of California, Santa Barbara  
(2007 NNIN Intern at UCSB and 2008 NNIN iREU Intern in Tsukuba, Japan)

Contact: bbsmith5asu.edu, speck@mrl.ucsb.edu, mcskimming@gmail.com

## Abstract:

We explored how n-type gallium nitride (GaN) electron mobility is affected by plasma assisted molecular beam epitaxy (PAMBE) growth conditions. The primary goal was to determine the conditions that produce the highest mobility. First, we performed a doping study to determine which carrier concentration produced the highest mobility. We then optimized mobility by varying plasma power and flow rate. All carrier concentrations and mobilities were determined using the Hall Effect. The doping study demonstrated that the optimal carrier concentration was  $\sim 1.5 \times 10^{15} \text{ cm}^{-3}$ . The highest mobility at this optimal carrier concentration was  $\sim 550 \text{ cm}^2/\text{V}\cdot\text{s}$ , thus achieving our primary goal.

## Introduction:

GaN is a semiconductor of interest because of its current use in light emitting diodes (LEDs) and because of its potential future applications in high power and high frequency devices. However, there are still issues with GaN that need to be explored in order to make these exciting future applications more feasible for large scale implementation. We need to determine how to grow the best quality GaN possible. PAMBE is one prominent GaN growing method used primarily in research settings that gives the user precise control over the samples produced, though it is generally slower than other methods. However, the plasma source used in this study produced growth rates higher than any PAMBE system recorded to date [1]. We hoped to grow the highest mobility GaN possible using this new plasma source by optimizing PAMBE growth conditions. Though many different growth parameters could be varied, the two parameters focused on here were plasma power and nitrogen flow rate into the power source.

## Experimental Procedure:

To optimize the PAMBE growth conditions, the experiment was broken into two parts: an optimizing carrier concentration study and an optimizing mobility study. The first part determined the optimal carrier concentration.

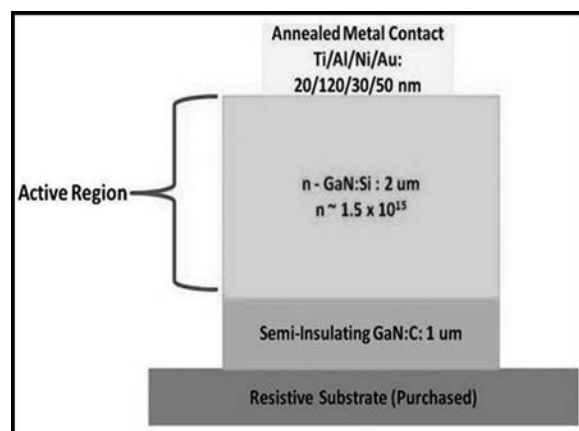


Figure 1: Cross section of a completed sample (schematic).

Various doping concentrations were tested by changing the temperature of the growth chamber. After PAMBE growth with the Nitride Gen III system onsite, each sample was characterized with atomic force microscopy (AFM) to ensure proper morphology. After checking the structure, we added many metal contacts on each sample for testing by a simple two mask contact photolithography process. The metal contacts were arranged in a Greek cross formation, and from each cross, a single Hall Effect measurement could be taken. The Hall Effect measurements determined the carrier concentrations and mobilities. Figure 1 shows a schematic of the cross-section of a completely processed sample. The measured carrier concentration that produced the highest mobility could then be matched with its corresponding doping so that way the mobility could be further optimized in part two.

After the optimal carrier concentration was determined, various plasma powers and nitrogen flow rates were tested to find the combination that produced the highest overall mobility. The samples in this series all had the carrier concentration determined in the first study. The same procedure of sample preparation and testing was used for this series as well.

M  
A  
T  
S

## Results and Conclusions:

Figure 2 is an AFM image showing typical morphology of the samples tested in both series. The step-like features present are indicative of proper PAMBE growth. This step was done as a quality check so that poor films were not processed. Figure 3 shows the results of the carrier concentration study. The two data sets presented were taken at the two plasma conditions shown. Both data sets indicate that the carrier concentration producing the greatest mobility is about  $1.5 \times 10^{15} \text{ cm}^{-3}$ .

Figure 4 shows the results of the optimization study. All samples presented in Figure 4 have the same carrier concentration of about  $1.5 \times 10^{15} \text{ cm}^{-3}$  so that they can be fairly compared. The highest mobility recorded in this series was  $\sim 550 \text{ cm}^2/\text{V}\cdot\text{s}$ . The plasma power and nitrogen flow rate that produced this highest mobility were 200 W and 10 standard cubic centimeters per minute (sccm).

The results of both studies make sense. In the doping study, lower carrier concentration corresponds to lower doping. Lower doping means fewer possible scattering sites for the charge carriers in the film. Less scattering events corresponds to higher mobility, which is supported by the results of that series. The results of the optimization series also make sense because higher powers and flow rates may have the potential of damaging the film which would lower the mobility.

## Future Work:

We hope to continue the optimization study for it to include other plasma powers and nitrogen flow rates so that it is more complete. Once the optimization study is fully complete, other parameters could be tested to further optimize mobility. Also, temperature dependent Hall Effect measurements should be taken so that defect concentrations can be determined. These results could be correlated to the mobilities measured for a more complete understanding of the material.

## Acknowledgements:

I would like to thank Professor Speck, my mentor Brian McSkimming, the rest of the Speck group, the UCSB cleanroom staff, and my fellow intern Rachel Lucas for their support and guidance with this project. (My mentor especially deserves credit for his outstanding guidance throughout this REU experience.) Finally, I would like to thank NSF and the NNIN REU Program for their resources and for giving me this wonderful learning opportunity.

## References:

- [1] B.M. McSkimming, F. Wu, T. Huault, C. Chaix, J.S. Speck. Plasma assisted molecular beam epitaxy of GaN with growth rates  $> 2.6 \mu\text{m}/\text{h}$ , *J. of Crystal Growth*, Volume 386, 15 January 2014, Pages 168-174 (2013).

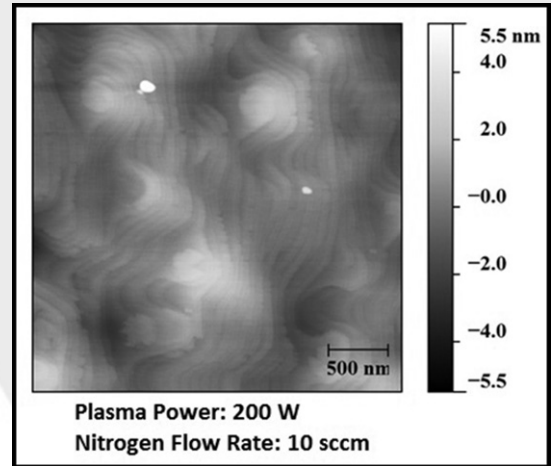


Figure 2: Typical morphology of a GaN film used in this study. All samples tested had similar morphologies.

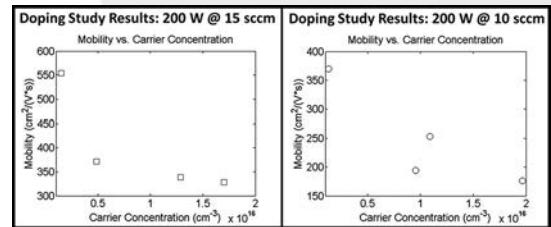


Figure 3: Mobility vs. carrier concentration for the listed growth conditions.

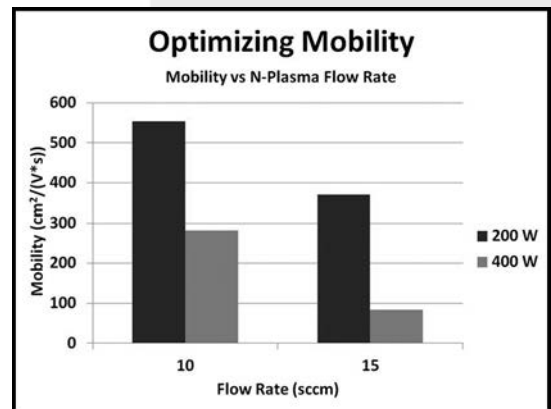


Figure 4: Mobility vs. nitrogen flow rate for plasma powers of 200 W and 400 W.

M  
A  
T  
S

# Doping in Spray-Deposited Fe<sub>2</sub>O<sub>3</sub> for Next-Generation Photovoltaics

Wesley Tatum

Physics and Physical Chemistry, Whitworth University

*NNIN REU Site: ASU NanoFab, Arizona State University, Tempe, AZ*

*NNIN REU Principal Investigator: Dr. Meng Tao, Electrical Engineering, Arizona State University*

*NNIN REU Mentor: Woo Jung Shin, Materials Science, Arizona State University*

*Contact: wtatum15@my.whitworth.edu, meng.tao@asu.edu, wshin4@asu.edu*

## Abstract:

The purpose of this experiment was to find optimal and simple parameters for fabrication of highly efficient solar cells with earth rich materials, which are capable of large scale deployment. Spray pyrolysis is a simple method for the creation of thin film solar cells. In this process, a solution is “atomized” into small droplets. A heated substrate evaporates the solvent, leaving behind a precipitated thin film. This technique was used to deposit a film of doped iron oxide (Fe<sub>2</sub>O<sub>3</sub>) onto a heated glass substrate, with a 100% ethanol solvent. The Fe<sub>2</sub>O<sub>3</sub> was doped with zinc from zinc chloride (ZnCl<sub>2</sub>). The samples were then analyzed for optimal morphology/film quality, resistivity, and transmittance using 4-point probe, SEM, and spectrophotometer. There was found to be no correlation between morphology patterns of doped and un-doped samples with the same deposition parameters. The optimal doped film structure was found to be amorphous. Optimal doping was at 9%, with a resistivity of 250 Ω-cm.

## Introduction:

Current solar technologies are not sustainable at the terawatt scale of energy harvesting and storage. This is because they rely on either silicon (Si) or rare earth metals. Si requires massive amounts of energy for isolation, as well as notoriously harsh chemicals in the manipulation of the Si wafers, such as hydrofluoric acid or “piranha.” Rare earth metals are just that: rare. Should solar energy seek to be a main energy source for society, the materials need to be in abundance and easy to isolate and manipulate. The optimal cell would also be easily translatable to large scale production.

## Experimental Procedure:

A solution was prepared with a molarity varying from 0.1-1.0 M ferric chloride (FeCl<sub>3</sub>) in a solution of water, ethanol, or a 50/50 mixture of the two. The solution was then mixed with ZnCl<sub>2</sub> to be 4-20% by mass. The solution was sucked into a titanium bodied Fuso Seiki STA-5N atomizing mister (Figures 1 and 2). The solution was sprayed onto a heated substrate (glass slides). On the glass slides, a small shard of Si wafer was pinned down to cover a section of the thickest part of the film (Figure 3), so that its thickness could be measured via profilometry. As the solvent evaporated, a thin film was deposited onto the substrate [1]. Following an experimentally derived “recipe,” approximately 1 μm of film was deposited, with varying temperatures, but leaving the liquid consumption rate (LCR) and the nozzle-substrate-distance constant. This combination was used because these three variables all affect the rate at which the solvent is evaporated [1]. The sample was then allowed to cool to a temperature below 150°C before it was removed from the hotplate.

## Results and Conclusions:

When the molarity of the FeCl<sub>3</sub> was varied, a correlation between that and film quality was found; the lower the molarity, the better the film quality [1] and the longer the deposition time was required to be. Film quality was judged by the crystallinity. In balancing these factors, 0.11 M FeCl<sub>3</sub> was found to be optimal [2, 3]. Solvent was varied from pure water to pure ethanol. The latter of these extremes yielded both highest film quality and shortest deposition time — 8:00 for 900 nm. Amorphous films (Figure 4) proved to have drastically lower resistivity than crystallized films, by at least two orders of magnitude.

After initial testing, continuous deposition produced lower resistivity than a pulsed deposition (rounds of :20 deposition and 1:00 re-heat period). The optimal resistivity was calculated to be 250 Ω-cm. This was found at 9% doping, which conflicts with literature values [2, 3]. This may be because we used an air carrier gas, rather than pure oxygen, and could also be due to a difference in spray techniques. This result is within three orders of magnitude of the goal 1-5 Ω-cm, which is encouraging, and this resistivity indicates that the material, still in its rudimentary stages, has the potential to be a sustainable and easily produced replacement for Si-based technologies.

## Future Work:

Thermal annealing needs to be explored to see if resistivity can be lowered through that route. Sulfurization of the samples also needs to occur to tune the band gap of the film, as well as to lower the resistivity of the film. The p-type doped half of the solar cell also needs to be designed and produced.

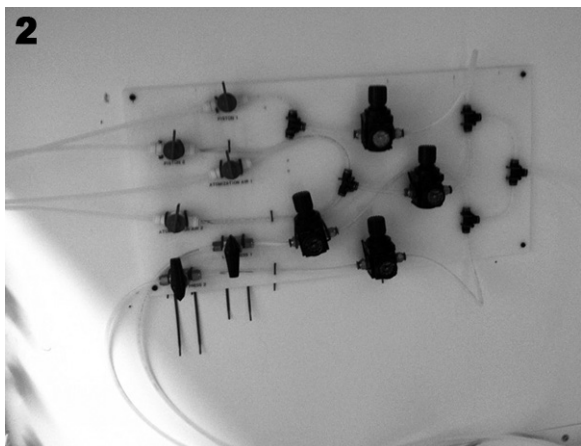
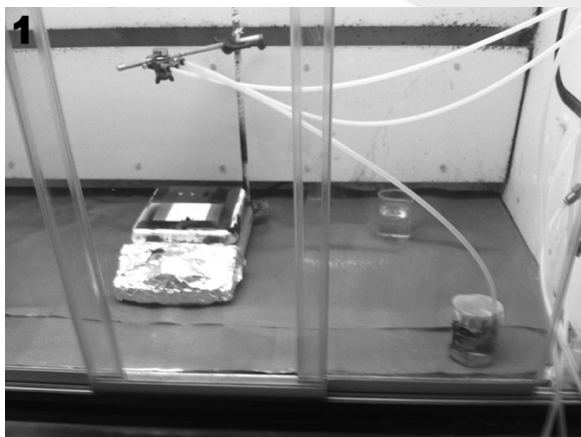


Figure 1, top left: Solution is sucked into the atomizer main body, where it is then sprayed as a mist towards the heated glass substrate.

Figure 2, bottom left: A system of valves and tubing directs pressure to the atomizer piston (controlling liquid flow), the main body (adding pressure to the solution), and to a carrier gas source (air).

Figure 3, right: Sample 7/23-2. Has lowest resistivity. Clearly visible is the section covered by the shard of silicon.

### Acknowledgements:

I would like to thank my PI, Dr. Meng Tao, and my mentor, Woo Jung Shin, for all of their help, support and guidance. I would also like to thank the Center for Solid State Electronics Research. Finally, a thanks to the National Science Foundation and all of those who helped to make the NNIN REU Program possible.

### References:

- [1] Hamedani, H.A. Investigation of Deposition Parameters in Ultrasonic Spray Pyrolysis for Fabrication of Solid Oxide Fuel Cell Cathode. Ph.D. Thesis, Georgia Institute of Technology, December 2008.
- [2] Ingler, W.; Baltrus, J.P.; Kahn, S.U.M. Photoresponse of p-Type Zinc-Doped Iron(III) Oxide Thin Films. J. Am. Chem. Soc. 2004, 126, 33.
- [3] Kumari, S.; Tripathi, C.; Singh, A.P.; Chauhan, D.; Shrivastav, R.; Dass, S.; Satsangi, V.R. Characterization of Zn-Doped hematite thin films for photoelectrochemical splitting of water. Cur. Sci. 2006, 91, 8.

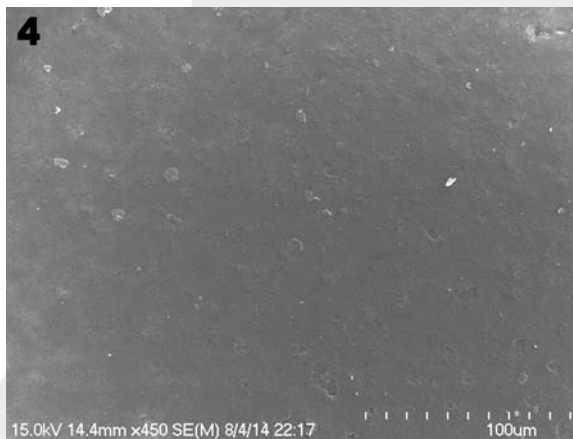


Figure 4: Sample 7/23-2. Amorphous film allows for even distribution of the dopant. Ethanol allows for fewer surface defects (e.g., pores, cracks, etc.).

# Investigation of Straight-Edge Graphene Grown via Segregation on Ni(110) using Scanning Tunneling Microscopy

Jill Wenderott

Physics, University of Kansas, Materials Science and Engineering, University of Michigan

**NNIN iREU Site: National Institute for Materials Science (NIMS), Tsukuba, Ibaraki, Japan**

*NNIN iREU Principal Investigator: Dr. Daisuke Fujita, National Institute for Materials Science, Tsukuba, Ibaraki, Japan*

*NNIN iREU Mentor: Dr. Keisuke Sagisaka, National Institute for Materials Science, Tsukuba, Ibaraki, Japan*

*Contact: jwenderott@gmail.com, fujita.daisuke@nims.go.jp, sagisaka.keisuke@nims.go.jp*

## Abstract and Introduction:

Controlling the size and shape of graphene grown on metal surfaces is key to utilizing graphene in future applications. Despite having three-fold symmetry, graphene was found to grow in rectangular shapes and with straight edges on the Ni(110) surface. The focus of this project was to clarify the growth mechanism of graphene on the Ni(110) surface by observing the edges of graphene with atomic resolution. Two samples were investigated in this project: pristine Ni(110) and carbon-doped Ni(110). It is known from prior work that nickel contains a small amount of impurity sulfur that will segregate and reconstruct on the surface in a  $c(2 \times 2)$  pattern upon annealing. This  $c(2 \times 2)$  pattern is hypothesized to be responsible for the rectangular shape of graphene by acting as a template for graphene growth.

Graphene was grown via surface segregation by heating and then cooling the carbon-doped nickel sample. The subsequently segregated graphene was characterized with various surface characterization techniques, including scanning tunneling microscopy (STM). It was found at the atomistic level that the leading edge of graphene grows in stair-stepping fashion and the reconstructed  $c(2 \times 2)$  sulfur on the surface of Ni(110) experiences stress during the growth of graphene, as indicated by circuitry patterns seen with STM. The density of the sulfur stress patterns changes with the size and density of graphene flakes, further confirming a direct relationship between the sulfur stress patterns and the growth of graphene.

## Methods:

Carbon was doped into a nickel sample at 800°C and in high vacuum for three weeks. The sample was placed in an ultra-high vacuum chamber and heated to 1000°C for one minute and cooled to prompt segregation of graphene. The cooling rate during segregation was manipulated to determine which yielded graphene with the best crystallinity. Upon segregating graphene, the sample was moved into the ultra-high vacuum STM chamber and measured at liquid nitrogen temperature (78K). These STM measurements provided an atomistic survey of the sample.

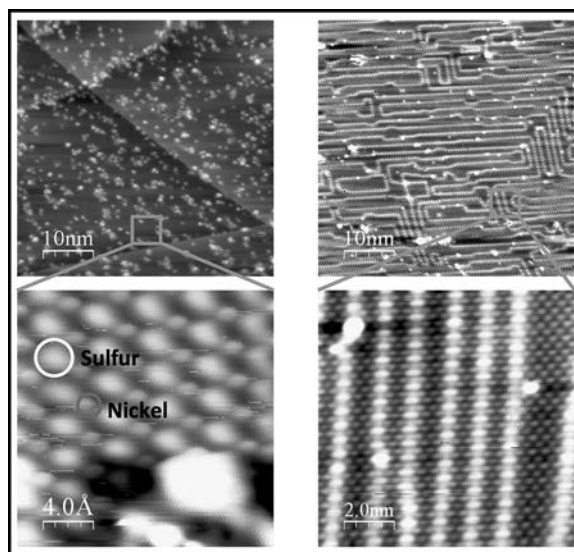


Figure 1: Sulfur on Ni(110) pristine (leftmost images), on C-doped Ni(110) (rightmost images).

The sample was also measured with low-energy electron diffraction (LEED), which showed the average crystal structure of the surface in reciprocal space, and Auger electron spectroscopy (AES), which revealed the chemical composition of the surface. Furthermore, helium ion microscopy, atomic force microscopy (AFM) and scanning electron microscopy (SEM) were used to look at the distribution and average size and shape of graphene flakes. All of these techniques allowed for a macroscopic view of the sample that, once paired with STM images, painted a more complete picture of the graphene growth mechanism on Ni(110).

## Results and Conclusions:

The  $c(2 \times 2)$  sulfur patterns on the pristine Ni(110) and the carbon-doped Ni(110) were first inspected to elucidate any differences. It was noted that STM images of the pristine Ni(110) surface confirmed the existence of sulfur arranged in

$c(2\times 2)$  pattern. The carbon-doped Ni(110) STM images also showed surface sulfur, but it was observed that sulfur was stressed in such a way that it produced intricate circuitry patterns (see Figure 1). As graphene was later found on the same sample, it was inferred that the growth of graphene was straining the  $c(2\times 2)$  sulfur either by competing with sulfur for placement on the Ni(110) surface or effectively “pushing” sulfur out of the way during its growth.

Next, graphene and the borders between graphene and sulfur on the carbon-doped Ni(110) were investigated. Fast-Fourier transforms of STM images of graphene showed certain areas of graphene to be highly-ordered, though in several cases highly-ordered graphene bordered semi-ordered graphene (see Figure 2). It was found that decreasing the cooling rate during segregation from  $10^\circ\text{C}/\text{sec}$  to  $3^\circ\text{C}/\text{sec}$  increased the ratio of well-ordered graphene to semi-ordered graphene, but decreasing the cooling rate to  $0.6^\circ\text{C}/\text{sec}$  resulted in multi-layer graphene. Thus, a balance was struck between cooling slow enough to produce well-ordered graphene and not cooling so slowly that multi-layer graphene was formed.

Regarding the borders between  $c(2\times 2)$  sulfur and graphene, it was found that graphene grew in a stair-stepping fashion down to the atomistic scale with STM (see Figure 3). This lent support to the hypothesis that graphene is using sulfur as a template for growth. It was also confirmed that graphene segregated was composed entirely of carbon and the surface surrounding it was covered in sulfur via AES.

Finally, it was observed that as the area of graphene on the nickel surface increased, the stress patterns of the  $c(2\times 2)$  sulfur experienced greater compaction (see Figure 4). When multi-layer graphene was grown, the stress patterns appeared the most compacted, implying that sulfur’s presence on the surface of nickel was potentially directing the growth of graphene. It was postulated that monolayer graphene segregated laterally across the surface of nickel compacting sulfur. When sulfur could not be pushed closer together, the graphene began to grow vertically away from the surface. The use of an element such as sulfur to direct and/or quench the growth of graphene would be a breakthrough in graphene research, but more studies are needed to confirm these preliminary findings.

### Future Work:

Theoretical modeling, such as density functional theory, is necessary to support experimental data collected thus far. The relative surface energies of sulfur and carbon on nickel should be considered to help clarify the mechanism of graphene growth. More experimental studies, such as segregation of graphene on nickel after sputtering sulfur from the surface, should also be conducted.

### Acknowledgments:

This project would not have been possible without many parties’ support. Many thanks are owed – the National Nanotechnology Infrastructure Network International Research Experience for Undergraduates (NNIN iREU) Program and National Science Foundation, for funding; H. Guo, for helium ion microscope measurements; K. Matsushita, for atomic force microscope measurements; and T. Kusawake, for tungsten tip preparation instruction.

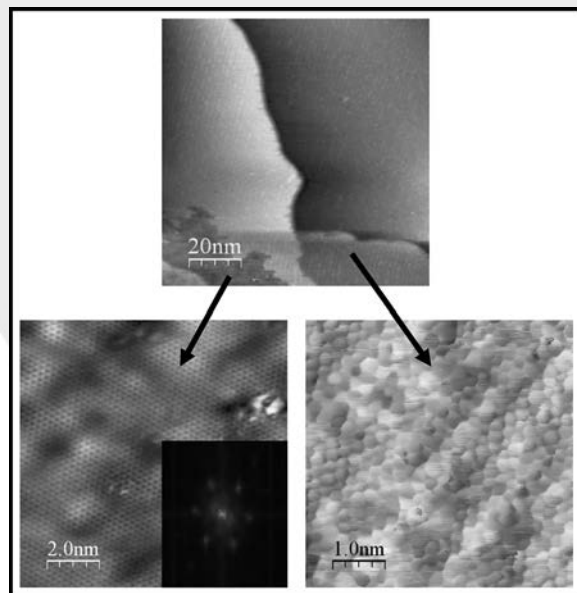


Figure 2: Well-ordered graphene (left) bordering semi-ordered graphene (right).

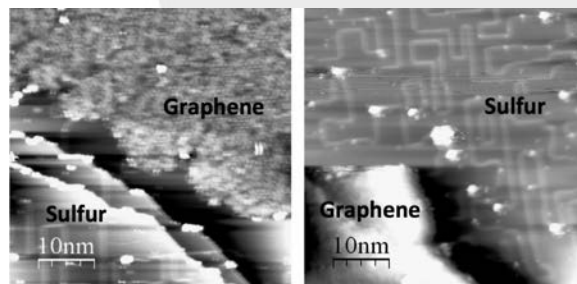


Figure 3: Borders between graphene and  $c(2\times 2)$  sulfur on Ni(110).

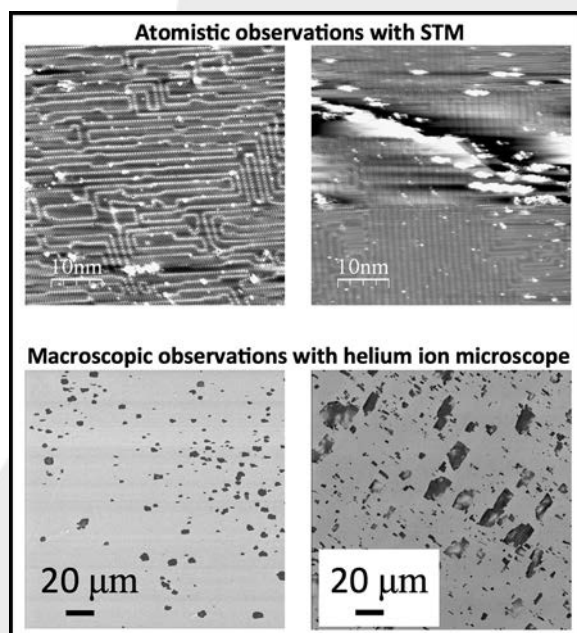


Figure 4: Comparison of sulfur stress patterns (top) to area of graphene growth (bottom), with the leftmost images corresponding to one sample and the rightmost images corresponding to another sample.

# BiO(ClBr)<sub>(1-x)/2</sub>I<sub>x</sub> Solid Solutions with Controllable Band Gap Engineering as Efficient Visible-Light Photocatalysts for Wastewater Treatment

Connie Wu

Electrical Engineering and Economics, University of Pennsylvania

**NNIN iREU Site: National Institute for Materials Science (NIMS), Tsukuba, Ibaraki, Japan**

NNIN iREU Principal Investigator: Prof. Jinhua Ye, International Center for Materials Nanoarchitectonics (WPI-MANA), National Institute of Materials Science (NIMS), Tsukuba, Ibaraki, Japan

NNIN iREU Mentor: Guigao Liu, International Center for Materials Nanoarchitectonics (WPI-MANA), National Institute of Materials Science (NIMS), Tsukuba, Ibaraki, Japan

Contact: wuconnie@seas.upenn.edu, liu.guigao@nims.go.jp, jinhua.ye@nims.go.jp

## Abstract:

The objective of this research was to find an efficient photocatalytic material for wastewater treatment. The motivation was the high cost of water treatment by oil refineries, industrial plants, and domestic waste. According to the American Society of Civil Engineers, wastewater infrastructure alone will cost around \$285 billion to build over the next 20 years [1]. As a result, BiO(ClBr)<sub>(1-x)/2</sub>I<sub>x</sub> solid solutions were investigated, because they are promising photocatalysts due to their efficient degradation capability, controllable band gap engineering, and visible light activity. The BiO(ClBr)<sub>(1-x)/2</sub>I<sub>x</sub> solid solutions were tested on water pollution proxies in the form of three dyes: methylene blue (MB), rhodamine B (RhB), and Orange II.

## Introduction:

In choosing the particular material to be used, the most important requirement was that the material be visible-light reactive. The current industry standard is titanium dioxide (TiO<sub>2</sub>). However, TiO<sub>2</sub> is only UV-light active, which is not ideal in terms of cost-efficiency. Similarly bismuth oxychloride (BiOCl) and bismuth oxybromide (BiOBr) are other bismuth oxyhalides that are only active under UV-light stimulation. Bismuth oxyiodine (BiOI) is visible-light active, however it has a low redox capability, which is detrimental to the degradation process in which the ability to separate electrons and holes is crucial [2]. Finally, the BiO(ClBr)<sub>(1-x)/2</sub>I<sub>x</sub> solid solution is both visible-light active and has a relatively high redox capability, and as such it provided a good basis to start our investigation into its ability to degrade wastewater liquid pollutants. Furthermore from previous research, it was also found that the photocatalyst's band gaps could be altered based on the ratio of halide composition [3]. Consequently, this allows for a method of band gap engineering that can allow for precise control of its visible-light activity.

## Experimental Procedure:

The BiO(ClBr)<sub>(1-x)/2</sub>I<sub>x</sub> solutions were prepared using a solvothermal method. First, ethylene glycol was mixed with Bi(NO<sub>3</sub>)<sub>3</sub>•5H<sub>2</sub>O to form a clear solution. Then the appropriate amounts of KCl, KBr, and KI salts were added with molar ratios (1-x)/2:(1-x)/2:x, where x is the percentage of KI. Next the mixture was transferred to a Teflon<sup>®</sup>-lined autoclave, which was then placed into a 160°C oven for 12 hours.

After the solution was removed from the oven, the resultant mixture was washed with water and air-dried at 70°C.

The photocatalyst was tested against the three pollutant proxies. First 100 ml of dye with a concentration of 8 mg/100 ml was mixed with 20 mg of photocatalyst. This was then placed into a liquid chamber cell and sonicated for 30 seconds before being placed under a 300W Xe arc lamp. Below was a L42 glass filter used to exclusively allow visible light and a water filter to disperse heat. Finally, 3 ml samples of the dye mixed with photocatalyst, taken in either 5-minute or 20-minute intervals depending on the characteristic degradation rate, were filtered through a syringe-driven filter unit. The samples' absorption spectra were obtained with a UV-vis spectrophotometer.

## Results:

Displayed in Figure 1 are the SEM images of the solid solutions. They formed uniform crystal spheres with larger clusters as the molar ratio of iodine increased. In the UV-vis absorption spectra (Figure 2), there was a continued blue-shift of the absorption edge as x increased. The reason was that the valence band minimum (VBM) had an upward shift as x increased from the increase in orbital potential energy with the substitution of Cl 3p and Br 4p orbitals by I 5p orbitals, creating a higher VBM [4]. This narrowed the band gap. Generally, a wider visible-light absorption would be beneficial to achieving a higher photocatalytic activity.

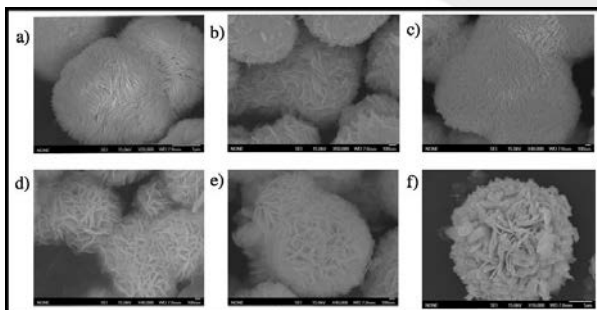


Figure 1: SEM images of the  $\text{BiO}(\text{ClBr})_{(1-x)/2}\text{I}_x$  crystals. (a)  $\text{BiO}(\text{ClBr})_{0.5}\text{I}_{0.5}$  (b)  $\text{BiO}(\text{ClBr})_{0.33}\text{I}_{0.33}$  (c)  $\text{BiO}(\text{ClBr})_{0.25}\text{I}_{0.5}$  (d)  $\text{BiO}(\text{ClBr})_{0.13}\text{I}_{0.67}$  (e)  $\text{BiO}(\text{ClBr})_{0.08}\text{I}_{0.83}$  (f)  $\text{BiOI}$ .

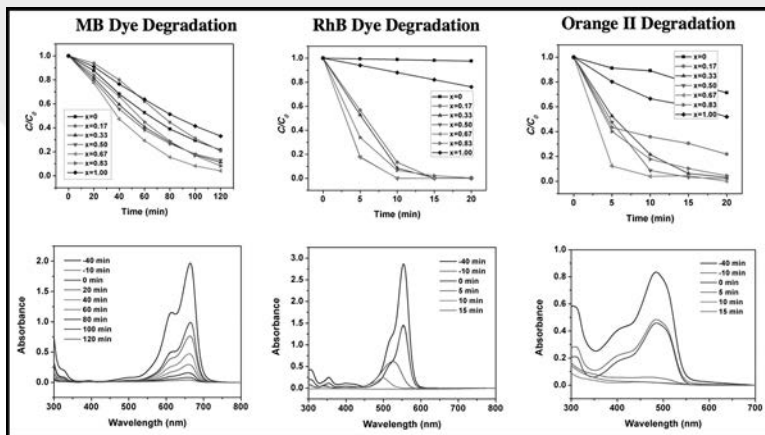


Figure 3: Degradation results.

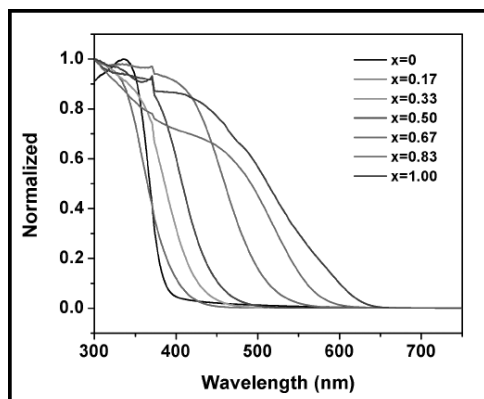


Figure 2: UV-vis absorption spectra of  $\text{BiO}(\text{ClBr})_{(1-x)/2}\text{I}_x$ . (See full color version on page xxxvi.)

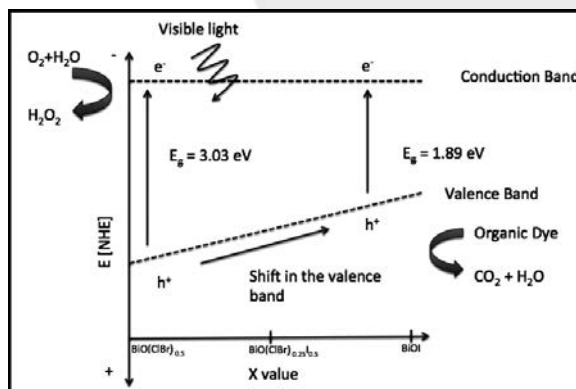


Figure 4: Band gap narrowing from shift in valence band.

Summarized in Figure 3 are the sample degradation results of the three dyes. It was found that an  $x$  value of 0.67 had the fastest degradation across all dyes. MB achieved the quickest degradation rate at 120 min, RhB at 5 min, and Orange II at 20 min.

The degradation is achieved through two differing mechanisms. When the photocatalyst was exposed to visible light, there was an excitation of electrons from the valence band to the conduction band, causing a separation of electrons and holes. Some holes reacted with water to form  $\bullet\text{OH}$ . The dye then reacted with either holes or  $\bullet\text{OH}$  to form water and carbon dioxide, completing the degradation process.

RhB, however, degraded faster than the other two dyes due to an additional mechanism. Typically for RhB degradation there is an added mechanism in which the RhB molecules form 2-3 unstable states, which will emit an electron to form  $\text{RhB}^+$ . This ion will then interact with holes or  $\bullet\text{OH}$  to simultaneously degrade the RhB dye.

## Conclusions:

$\text{BiO}(\text{ClBr})_{0.17}\text{I}_{0.67}$  exhibited the best photocatalytic properties across the dye pollutants. This is due to the tradeoff between

the increased absorption spectra inherent in the materials and the decrease in the redox capability as shown in the band gap diagram.

## Future Work:

In the future, we would like to quantify hole and  $\bullet\text{OH}$  generation in the photocatalytic process to confirm and characterize the reactions taking place.

## Acknowledgments:

I would like to thank my principal investigator, Jinhua Ye, and my mentor, Guigao Liu, for providing the inspiration for this project. I am also thankful to the NNIN iREU Program and NSF for providing the support and funding for this research.

## References:

- [1] "2013 Report Card for America's Infrastructure." American Society of Civil Engineers, n.d. Web. 30 July 2014.
- [2] Zhang, W.; Ind. Eng. Chem. Res. 2013, 52, 6740.
- [3] Zhang H. Phys. Chem. Chem. Phys. 2012, 14, 1286.
- [4] Shannon, R. Acta. Cryst. A 1976, 32, 751.

# Effects of Doping on Boride Thermoelectrics

Allison Wustrow

Chemistry, University of California Berkeley

**NNIN iREU Site: National Institute for Materials Science (NIMS), Tsukuba, Ibaraki, Japan**

*NNIN iREU Principal Investigator: Prof. Takao Mori, MANA, National Institute for Materials Science, Tsukuba, Ibaraki, Japan*

*NNIN iREU Mentor: Dr. Satofumi Maruyama, MANA, National Institute for Materials Science, Tsukuba, Ibaraki, Japan*

*Contact: wustrow@berkeley.edu, maruyama.satofumi@nims.go.jp, mori.takao@nims.go.jp*

## Introduction:

Approximately two thirds of the primary energy consumed by mankind is lost, with much of the loss being in the form of waste heat. Thermoelectrics can be used to recover some of that energy by converting a temperature gradient into an electrical current [1]. An ideal thermoelectric has a high Seebeck coefficient, which means it can produce many volts of potential per temperature change across the material, a low electrical resistivity, allowing for easy electronic transport across the material, and a low thermal conductivity, allowing for a temperature gradient to more easily be created across the material. The product of the Seebeck coefficient squared and electrical resistivity are referred to as a material's power factor, which is a measure of how much electrical power the thermoelectric can produce.

Thermoelectrics can be either p-type or n-type depending on whether the material's charge carriers are holes or electrons. Having matching p- and n-type thermoelectrics increases device efficiency. Borides, an attractive candidate for high temperature thermoelectrics, are mostly p-type due to a two electron deficiency in the boron icosahedra in their crystal structure [2]. However, by adding metals such as aluminum to yttrium boride ( $YB_{25}$ ), one can add electrons to the valence band of the boride, transitioning the thermoelectric into n-type [3]. Doping with vanadium has been shown to improve the thermoelectric properties of another n-type boride,  $YB_{22}C_2N$  [4]. In this report, vanadium (V) and manganese (Mn) were doped into yttrium aluminum boride ( $YAIB_{14}$ ) in an attempt to add electrons to the boride valence band, improving the thermoelectric properties of the material.

## Methods:

Yttrium oxide and boron powder were mixed together in a 3:8 weight ratio and heated under vacuum at 1600°C for eight hours to make  $YB_{25}$ . Samples were ground and washed in 33% nitric acid to remove impurity phases. The powder was rinsed in water, ethanol and acetone and dried. Al powder was added to the powder in a 2:1  $YB_{25}$  to Al weight ratio. The mixture was held at 1300°C for four hours to form  $Y_{0.6}Al_{0.6}B_{14}$ . The pellet was ground and washed in a sodium hydroxide solution overnight to dissolve any remaining aluminum. The powder was rinsed in water ethanol and acetone.

For the V-doped sample,  $Y_{0.6}Al_{0.6}B_{14}$  (0.762g) and vanadium diboride (0.042g) were heated to 1500°C for five minutes at 100 MPa using a spark plasma sintering system. The Mn-doped sample was made by adding  $Y_{0.6}Al_{0.6}B_{14}$  (0.770) and manganese powder (0.036g) and heating in the same manner. Undoped  $Y_{0.6}Al_{0.6}B_{14}$  pellet was made by heating the powder (0.84g) under the same conditions in the spark plasma sintering system. Seebeck coefficient and resistivity measurements were made using ZEM-2. Annealed samples were made by annealing at 1000°C for eight hours under vacuum and four hours under argon, respectively.

## Results:

Doping YAIB with V and Mn improved the thermoelectric properties. Resistivity for both samples was much lower than for the undoped sample as shown in Figure 1. Both V and Mn are capable of donating some electrons to the boride electrical network. The addition of carriers to the conductive network increases the conductivity of the material. Unfortunately it also lowers the Seebeck coefficient as seen in Figure 2, as the voltage produced by a temperature difference is lower upon the addition of more carriers. However, by combining the two factors, one can see that the power factor for doping with both elements is larger than that of the undoped sample.

To further improve the power factor, the V-doped sample was annealed both under vacuum and argon. When annealed under vacuum, the Seebeck coefficient improved, suggesting removal of dopants from the material. The resistivity did not change with annealing, suggesting the removal of impurities from the material and the resulting decrease in resistivity balanced out the increase in resistivity caused by the removal of dopants. When the sample was annealed under argon, the Seebeck coefficient and resistivity both decreased, which is consistent with an increase in doping, as the extended heating assumedly allowed the vanadium to intercalate into the structure. The power factor for both annealing processes was higher than for the un-annealed sample. The sample annealed under vacuum had the highest power factor.

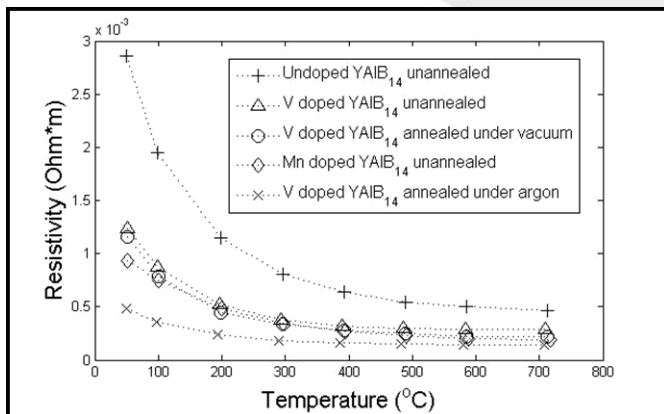


Figure 1: Resistivity of vanadium and manganese doped samples. Most samples had similar resistivities. Undoped  $YAIB_{14}$  had high resistivity, and vanadium doped  $YAIB_{14}$  annealed under argon had low resistivity.

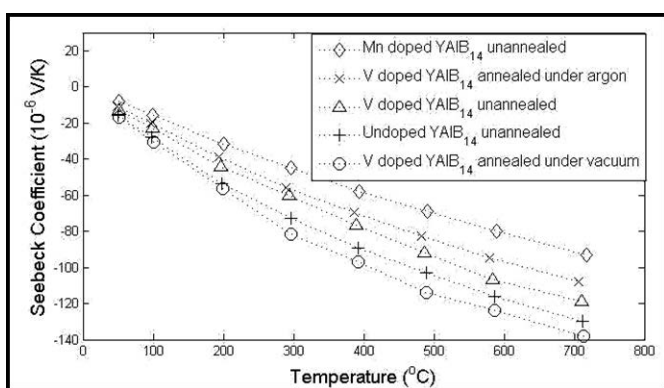


Figure 2: The Seebeck coefficient of vanadium and manganese doped samples. The lowest Seebeck coefficient belongs to manganese doped  $YAIB_{14}$ , and the highest is vanadium doped  $YAIB_{14}$  annealed under vacuum.

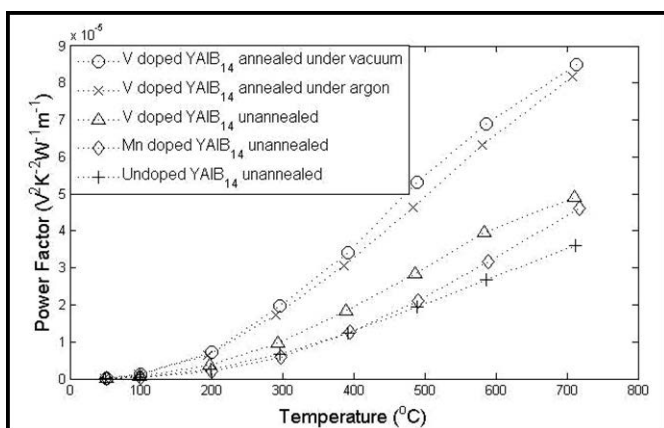


Figure 3: Power factor of vanadium and manganese doped samples. Annealed vanadium doped samples had the highest power factor.

## Conclusions:

Yttrium aluminum bromide's thermoelectric properties can be enhanced by additional doping with vanadium and manganese as well as annealing the sample after doping. However the thermoelectric properties are still much poorer than the p-type boron carbide. Further research is needed to determine which dopants increase thermoelectric properties, and to discover the mechanism by which annealing changes the Seebeck coefficient. This will lead to a better understanding of how to create more efficient n-type boride thermoelectrics.

## Acknowledgements:

I would like to thank Prof. Takao Mori, Dr. Satofumi Maruyama, and the entire Mori group for their guidance. I would also like to thank the NNIN iREU Program and NSF for funding this research, and the National Institute of Materials Science for hosting me.

## References:

- [1] "Thermoelectric Nanomaterials", ed. K. Koumoto and T. Mori, Springer Series in Materials Science (Springer, Heidelberg, 2013) pp. 1-375.
- [2] Mori, T. "Higher Borides", in: Handbook on the Physics and Chemistry of Rare-earths, Vol. 38, ed. K. A. Gschneidner Jr., J. -C. Bunzli, and V. Pecharsky (North-Holland, Amsterdam), pp. 105-173 (2008).
- [3] Maruyama, S., Miyazaki, T., Hayashi, K., Kajitani, T., Mori, T. Applied Physics Letter, 101 (2012) 152101.
- [4] Prytuliak, A., Maruyama, S., Mori, T. Materials Research Bulletin, 48, (2013), 1972.